



Justus-Liebig-University Giessen  
Institute of Physical Chemistry

*Ceria - zirconia thin films*

---

*Influence of nanostructure and moisture on charge transport properties*

Dissertation

by

Matthias Kleine-Boymann

Master of Science

April 2021

1st reviewer : Prof. Dr. Jürgen Janek

2nd reviewer : Prof. Dr. Bernd Smarsly



# Erklärung

Ich erkläre:

Ich habe die vorgelegte Dissertation selbständig und ohne unerlaubte fremde Hilfe und nur mit den Hilfen angefertigt, die ich in der Dissertation angegeben habe.

Alle Textstellen, die wörtlich oder sinngemäß aus veröffentlichten Schriften entnommen sind, und alle Angaben, die auf mündlichen Auskünften beruhen, sind als solche kenntlich gemacht.

Bei den von mir durchgeführten und in der Dissertation erwähnten Untersuchungen habe ich die Grundsätze guter wissenschaftlicher Praxis, wie sie in der „Satzung der Justus-Liebig-Universität Gießen zur Sicherung guter wissenschaftlicher Praxis“ niedergelegt sind, eingehalten.

Münster, den

Matthias Kleine-Boymann, MSc.



- Meiner Familie -



# Danksagung

Zur Entstehung der vorliegenden Dissertation haben viele Menschen einen wichtigen Beitrag geleistet. Allen Beteiligten möchte ich an dieser Stelle meinen Dank aussprechen, auch wenn ich sie hier nicht explizit erwähne.

Im Besonderen danke ich Prof. Dr. Jürgen Janek für die hervorragende Betreuung und die interessante Themenstellung, sowie das Schaffen der hervorragenden Rahmenbedingungen innerhalb der Arbeitsgruppe.

Dr. Matthias Elm danke ich für die vielen unentbehrlichen wissenschaftlichen Diskussionen, die ständige Ansprechbarkeit, sowie das Korrekturlesen dieses Manuskripts.

Ich danke Raika Oppermann und Julian Zahnow, die ihre Abschlussarbeiten zum Teil unter meiner Betreuung durchgeführt haben und damit einen wichtigen Beitrag zu der vorliegenden Dissertation geleistet haben.

Dem gesamten Delfin-Team danke ich für die wöchentlichen Diskussionsrunden aus denen ich immer wertvolle Anregungen und Erkenntnisse mitgenommen habe.

Meinen Bürokolleginnen und -kollegen Dr. Birte Jache, Katrin Michel, Jonas Neumeier und Dr. Jonas Hofmann danke ich für das Ertragen meiner „Stimmungsschwankungen“ und die unzähligen konstruktiven Diskussionen und kollegialen Hilfestellungen im Laboralltag.

Allen anderen Mitgliedern in der AG Janek danke ich für die Hilfsbereitschaft und Kollegialität, die ich während meiner Zeit in der Arbeitsgruppe und auch nach meinem Weggang erfahren habe.

Insbesondere bin ich aber meiner Partnerin Laura und meiner Familie zutiefst dankbar. Ohne ihren uneingeschränkten Rückhalt und die bedingungslose Unterstützung über all die Jahre wäre dieses Manuskript nie zustande gekommen. Gerade in Zeiten des Haderns waren sie der Grund nicht aufzugeben und zu beenden was ich begonnen habe. Danke!



## Abstract

In the last decade a huge expansion of nanomaterial applications being introduced into all kinds of markets is observed leading to a growing tendency to tailor the fabrication of materials with nanodimensions in order to tune their properties, optimizing them for a certain process. The same holds true for ceria based solid solutions.

CeO<sub>2</sub> - ZrO<sub>2</sub> solid solutions are well established for the use as part of three-way catalytic converters in the exhaust gas cleaning system of combustion engines. Apart from that ceria is studied for the use in a wide range of applications, like solid oxide fuel cells, polymer exchange membrane fuel cells, both being almost fully developed to be introduced for a wide market. Next to others, currently emerging applications are the use of ceria as a catalyst for reforming processes, water-gas shift reaction or thermochemical water splitting.<sup>1</sup>

Due to the complexity of CeO<sub>2</sub> - ZrO<sub>2</sub>- based materials the preparation of model systems has proven to be a highly versatile approach in order to gain a deeper understanding of specific phenomena. The same approach was used in the work presented here, following several preliminary studies on single crystalline material on the oxygen transport properties of ceria- zirconia solid solutions by means of surface analytical techniques and electrochemical impedance spectroscopy in the work group of Prof. Jürgen Janek.<sup>2-5</sup> Thin films offer a more straightforward application of surface analysis techniques, as well as the possibility to tune the structural and electronic properties of the material under investigation.

In this work CeO<sub>2</sub> - ZrO<sub>2</sub> thin films were deposited by means of pulsed laser deposition. The resulting Ce<sub>1-x</sub>Zr<sub>x</sub>O<sub>2</sub> thin films of different morphology and composition (ranging from  $x = 0 - 0.4$ ) were characterized by surface analytical techniques as well as electrochemical impedance spectroscopy (EIS). EIS allows to precisely control the atmospheric conditions such as gas type and mixture or temperature and humidity using a respective experimental setup described in the methods section of this manuscript.

The presented work focusses on the influence of grain boundaries and the surface, as they play an important role for thin film transport processes. Electrochemical impedance spectroscopy allows to deduce transport properties of the thin films under investigation and compare those to respective models. At moderate and very low temperatures down to room temperature water influences the conductivities determined during the experiments. In the respective literature which is going to be reviewed in the theoretical section of this work an ongoing discussion on the influence of water vapor in the surrounding atmosphere (humidity) during impedance measurements is revealed. The experimental results in this work are described in good agreement by a model combining thermodynamic adsorption models with the theory of percolating networks. These results reveal valuable information to the ongoing discussions in literature.



## Zusammenfassung

In den letzten Jahrzehnten haben sich Nanomaterialien zunehmend für technische Anwendungen etabliert und wurden in die verschiedensten Märkte eingeführt. Dies bedingt eine zunehmenden Notwendigkeit, die Herstellung von Materialien mit Nanodimensionen weiterzuentwickeln, um ihre Eigenschaften gezielt zu beeinflussen und sie für einen bestimmten Prozess gezielt zu optimieren.

Gleiches gilt für feste Lösungen auf Ceroxidbasis. So sind  $\text{CeO}_2$  -  $\text{ZrO}_2$ - Materialien für den Einsatz in Dreiwegekatalysatoren für die Abgasreinigungsanlage von Verbrennungsmotoren etabliert. Abgesehen davon werden Ceroxidmaterialien für den Einsatz in einer ganzen Reihe von Anwendungen, wie zum Beispiel Festoxidbrennstoffzellen und Polymeraustauschmembranbrennstoffzellen weiter entwickelt. Beide Brennstoffzellensysteme stehen kurz davor in den breiten Markt eingeführt zu werden. Anwendungen, die hingegen noch nicht marktreif, aber dennoch vielversprechend sind, sind unter anderem die Verwendung von Ceroxid als Katalysator für Reformierungsprozesse, Wasser-Gas-Shift-Reaktionen oder die thermochemische Wasserspaltung.<sup>1</sup>

Aufgrund der Komplexität von  $\text{CeO}_2$  -  $\text{ZrO}_2$ - basierten Materialien hat sich die Herstellung von Modellsystemen als ein sehr vielseitiger Ansatz etabliert, um ein tieferes Verständnis über bestimmte Phänomene zu erlangen. In der hier vorgestellten Arbeit wurde der gleiche Ansatz verfolgt, nachdem in der Arbeitsgruppe von Prof. Jürgen Janek mehrere Arbeiten zu einkristallinem Material über die Sauerstofftransporteigenschaften von festen  $\text{CeO}_2$  -  $\text{ZrO}_2$ - Lösungen mit Oberflächenanalytik und elektrochemischer Impedanzspektroskopie durchgeführt wurden.<sup>2-5</sup> Dünnschichten erlauben eine einfachere Anwendung von Oberflächenanalysetechniken sowie die Möglichkeit, die strukturellen und elektronischen Eigenschaften des zu untersuchenden Materials einzustellen. Mittels gepulster Laserabscheidung wurden in dieser Arbeit  $\text{CeO}_2$  -  $\text{ZrO}_2$ - Dünnschichten abgeschieden. Die resultierenden  $\text{Ce}_{1-x}\text{Zr}_x\text{O}_2$ - Dünnschichten unterschiedlicher Morphologie und Zusammensetzung ( $x = 0 - 0.4$ ) wurden sowohl durch oberflächenanalytische Techniken als auch mittels elektrochemischer Impedanzspektroskopie (EIS) charakterisiert. EIS erlaubt es die atmosphärischen Bedingungen wie Gasart, -gemisch und Temperatur, als auch die Luftfeuchtigkeit, mithilfe eines entsprechenden Versuchsaufbaus zu kontrollieren. In dieser Arbeit liegt hierbei der Fokus auf dem Einfluss von Korngrenzen und der Oberfläche, da diese für Dünnschichttransportprozesse eine wichtige Rolle spielen. Die elektrochemische Impedanzspektroskopie ermöglicht es, die Transporteigenschaften der untersuchten dünnen Filme abzuleiten und diese mit den jeweiligen Modellen zu vergleichen. Bei mäßigen und sehr niedrigen Temperaturen beeinflusst Feuchtigkeit die während der Experimente ermittelten Leitfähigkeiten. In der Literatur, die im theoretischen

Teil dieser Arbeit vorgestellt wird, wird der Einfluss von Wasserdampf in der Atmosphäre bei Impedanzmessungen mittels verschiedenster Ansätze diskutiert. Die experimentellen Ergebnisse dieser Arbeit werden mit einem Modell beschrieben, das ein thermodynamisches Adsorptionsmodell mit der Perkolationstheorie kombiniert. Die daraus abgeleiteten Erkenntnisse tragen einen wertvollen Beitrag zu der aktuellen Diskussion bei.

# Contents

<b>1</b>	<b>Introduction and motivation</b>	<b>1</b>
1.1	Aspects of influences on the conductivity of ceria based thin films . . . . .	4
<b>2</b>	<b>Theory and state of research</b>	<b>9</b>
2.1	Defect chemistry of $\text{CeO}_2$ and $\text{Ce}_{1-x}\text{Zr}_x\text{O}_2$ . . . . .	9
2.1.1	Pure Ceria . . . . .	10
2.1.2	The solid solution $\text{Ce}_{1-x}\text{Zr}_x\text{O}_2$ and its defect chemistry . . . . .	12
2.2	Defect chemistry in the vicinity of interfaces . . . . .	16
2.3	Influence of water at interfaces . . . . .	20
2.3.1	Physisorption and chemisorption . . . . .	21
2.3.2	Literature on the influence of humidity on the conductivity of ceria based materials . . . . .	26
2.4	Percolation theory . . . . .	41
<b>3</b>	<b>Methods</b>	<b>45</b>
3.1	Sample preparation . . . . .	45
3.1.1	Target preparation . . . . .	45
3.1.2	Thin film pulsed laser deposition (PLD) . . . . .	46
3.2	Crystallographic and morphologic characterization . . . . .	47
3.2.1	X-ray diffraction (XRD) . . . . .	47
3.2.2	Morphological and chemical characterization . . . . .	48
3.3	Electrochemical characterization . . . . .	49
3.3.1	Photolithography . . . . .	49
3.3.2	Electrochemical impedance spectroscopy under controlled atmosphere . . . . .	51
<b>4</b>	<b>Results and discussion</b>	<b>57</b>
4.1	Morphology and chemical composition of the PLD targets . . . . .	57
4.2	Morphological and chemical characterization of the thin films . . . . .	61
4.3	Electrochemical impedance spectroscopy results . . . . .	72
4.3.1	Measurements under dry atmosphere . . . . .	72

4.3.2	Measurements under humid atmosphere at elevated temperatures ( $200^{\circ}\text{C} > T > 550^{\circ}\text{C}$ ) . . . . .	89
4.3.3	Measurements under humid atmosphere at low temperatures ( $30^{\circ}\text{C} > T > 200^{\circ}\text{C}$ ) . . . . .	97
<b>5</b>	<b>Conclusion and outlook</b>	<b>115</b>
<b>6</b>	<b>Supplement</b>	<b>119</b>
	<b>Bibliography</b>	<b>121</b>

## Nomenclature

$\Delta H_{AF}$  Enthalpy of Anti- Frenkel pair generation

$\Delta H_{Red}$  Enthalpy of  $Ce^{4+}$  reduction

$\Delta S_{AF}$  Entropy of Anti-Frenkel pair generation

$\Delta S_m$  Entropy of migration

$\Delta S_{Red}$  Entropy of reduction

$\gamma$  Grain boundary energy

$Ce'_{Ce}$  Small polarons

$O''_i$  Oxygen interstitials

$O^x_O$  Oxide ions on oxide sites

$R_A$  Roughness, arithmetic mean

rh% Relative humidity in %

$V^{\bullet\bullet}_O$  Oxygen vacancies

$\Phi$  Space-charge potential

$\Theta$  Surface coverage

$E_A$  Activation energy

$M$  Grain boundary mobility

$p_{H_2O}$  Water partial pressure

$p_{O_2}$  Oxygen partial pressure

$P$  Probability

$p$  Partial pressure

$p_{sat}$  Saturation partial pressure

10CZO  $CeO_2$

5CZO  $Ce_{0.5}Zr_{0.5}O_{2-\delta}$

6CZO  $Ce_{0.6}Zr_{0.4}O_{2-\delta}$

8CZO	$\text{Ce}_{0.8}\text{Zr}_{0.2}\text{O}_{2-\delta}$
CPE	Constant phase element (symbol Q)
CZO	Ceria zirconia oxide
EIS	Electrochemical impedance spectroscopy
emf	Electromotive force
FWHM	Full width at half maximum
G	Crystallite size
GDC	Gadolinium doped ceria
GI-XRD	Grazing incidence x-ray diffraction
HMDS	Hexamethyldisilazane
ICSD	Inorganic Crystal Structure Database
MIEC	Mixed ionic electronic conductor
PLD	Pulsed laser deposition
Q	See CPE
R	Ohmic resistance
RH	Relative humidity
SCL	Space charge layer
SDC	Samaria doped ceria
SEM	Scanning electron microscopy
SOFC	Solid oxide fuel cell
SPM	Scanning probe microscopy
TGA	Thermogravimetry analysis
tr-KPFM	Time-resolved Kelvin probe force microscopy
TWC	Three-way catalyst
XRD	X-ray diffraction
YSZ	Yttrium stabilized zirconia

# 1 Introduction and motivation

Most technical applications of ceria based materials are related to the redox chemistry of Ce(+III) and Ce(+IV), the affinity to oxygen and sulfur, and the electronic structure. Important areas of application are metallurgy, glasses, ceramics and catalysis. For most glasses cerium oxide is the most efficient polishing agent which consumes a significant portion of the cerium annually produced. Furthermore huge amounts of cerium based catalyst materials are used for the conversion of crude oil into lower weight fractions by fluid catalytic cracking. Aside from these, the major technological relevant application of cerium oxide based materials is the pollutant removal from vehicle exhaust emissions. Here ceria-zirconia based solid solutions act as a converter by storing oxygen from the exhaust gas stream when the air-fuel ratio becomes lean. Under conditions where sufficient oxygen is not available from the exhaust gas mixture the stored oxygen is released, promoting the oxidation of highly climate-wrecking gases to less climate active ones. For three-way catalyst (TWC) systems  $\text{CeO}_2 - \text{ZrO}_2$  solid solutions are probably the most investigated systems from a structural point of view.<sup>6</sup> Nevertheless, especially the recent scandals of car manufacturers manipulating their motor control software in order to cope with the stricter (and more representative for daily car use) exhaust gas regulations showed in a dramatic way that further improvement in the understanding of the fundamental processes is needed, assuring further improvements in this globally relevant matter.

An application that gained a lot of research interest in the last decades are solid oxide fuel cells, which are a very attractive class of electrochemical cell. They are compatible with several fuels without suffering from CO poisoning. Ceria based materials are used as electrolytes, as barrier layers, and as catalysts on both electrodes of the cell.<sup>1</sup>

In fuel cells chemically stored energy from the applied fuel is directly converted into usable electrical energy by an electrochemical reaction. Fuel cells are thus capable of overcoming typical limitations of combustion efficiency, the most prominent of which is the Carnot cycle. Different kinds of fuel cell techniques are available today. Proton exchange membrane fuel cells (PEMFC), alkaline fuel cells (AFC) and phosphoric acid fuel cells (PAFC) are typically operated at moderate temperatures between 50 – 250 °C, whilst molten carbonate fuel cells (MCFC) and solid oxide fuel cells (SOFC) operate at significantly higher temperatures of

650 – 1000 °C.<sup>7</sup> PEMFCs are based on proton conducting membranes, they require hydrogen fueling. They have been in the research focus during the last century, as potentially important part of a possible future hydrogen economy. Being compatible to run with the existing hydrocarbon fuel infrastructure, this flexibility in usable fuels is a huge advantage of SOFCs over PEMFCs. SOFCs can oxidize almost any fuel, may it be hydrocarbons, carbon or hydrogen, as the electrolyte transports oxygen ions. This allows the combustion of hydrocarbons with significant efficiency gains and thus also reduced CO<sub>2</sub> emissions.

So far the high operating temperatures resulting in higher system costs and faster loss of performance as well as slow start up and shut-down procedures limited the application range to stationary units. Lowering the operation temperature of an SOFC significantly below 600 °C would not only allow to apply a wider material choice for interconnects and sealings of the system, but also primary performance degradation mechanisms caused by sintering. In addition less insulation against heat loss would be necessary. For even lower temperatures below 350 °C the material costs for such a system would not only decrease further. Fast start-up and shut-down cycles would be feasible, being critical parameters for portable power and transportation usage.<sup>8</sup> In order to reach this goal, thin film approaches are very promising to reduce the area-specific resistance in order to achieve a certain targeted power density with a given open-circuit potential.

For all applications in which the electrochemical properties of ceria are relevant it is the ionic conductivity that allows the use of ceria zirconia based materials in the respective application. This is the reason why the transport properties of ceria based materials and thus its defect chemistry was intensely studied over the last decades, starting with works on bulk and single crystalline samples, continued with research on nanostructured ceria materials.<sup>8–29</sup> With this the investigation of a lower temperature range down to room temperature became more relevant for bulk samples. For thin films, with morphological features in the sub-micrometer range quite some literature is available too.<sup>30–42</sup> Some of the works on ceria-zirconia thin films will be presented in the literature chapter of this manuscript. Surface electrochemistry is however a complex process, controlled by the interplay of charge generation as well as field-controlled and diffusion-controlled transport. The presence of water within or on ceria ceramics is in most cases, inevitable during the operation of electrochemical devices.<sup>43</sup> In many of the available literature reports this key aspect is neglected when studying the transport processes in ceria based thin films. These are typically studied by impedance or DC conductivity measurements using highly sensitive equipment. It is very well possible that either a water layer on the surface or in the pores of the material forms or that it is even incorporated into the bulk or the grain boundaries, influencing the conductivity measured being a potential pathway for charge carriers. It is known that the surfaces and grain boundaries of

---

ceria are enriched in oxygen vacancies, which might be active sites for the incorporation of water into the material, changing its defect chemistry, and thus the results of the electrical conductivity measurements. With the application of ceria- zirconia materials on a nanometer level, surfaces and grain boundary influences will significantly increase, and with that the role of water adsorbing on these interfaces.

It is the purpose of the work presented here to study these aspects of nanocrystalline ceria-zirconia thin films. Therefore, thin films with well defined morphology were prepared. Their morphology is determined and correlated with their defect chemistry by analyzing their impedance response under defined oxygen and water activities in the atmosphere around the sample. Central questions that shall be addressed are: How is water interacting with solid surfaces, influencing the properties? How does water interact with ceria thin film surfaces at the solid gas interface. This is not only of great importance, for technical applications of MIEC's, where water could also be present. Zhang et al. for example have shown that ceria {100} terminated nano- cubes enable low-temperature oxygen storage capacities already at temperatures as low as 150 °C showing their great potential as low temperature material for typical ceria applications.<sup>44</sup> It is obvious that in such systems it is inevitable to understand how water is interacting with the surface of the material and influencing its properties in order to optimize the technical process in which the material is applied. On the other hand there are a lot of reports in literature, dealing with fundamental questions of charge transport in ceria based thin films. Here it is of significant importance to know if water could interfere with the experiments conducted, if not carefully excluded.

## 1.1 Aspects of influences on the conductivity of ceria based thin films

As mentioned in the introduction above there is an immanent motivation to investigate the influence of water on classical solid state electrochemistry experiments with a given thin film model system. There is an ongoing debate in literature about the effect of water in the gas atmosphere on the conductivity of ceria based bulk and thin film samples. This discussion will be summarized in paragraph 2.3. The processes of water influencing the electrochemical properties

is assumed to depend on the morphology and composition of the sample, the temperature regime under investigation, as well as the water partial pressure ( $p_{\text{H}_2\text{O}}$ ) at a given temperature. These considerations in combination with literature studies lead to different research questions that are introduced in the following paragraphs.

Before studying CZO thin films in such a complex environment, as it is the purpose of this study, it is necessary to go one step back and start the experiments with a reduced set of parameters. Thus, including humidity into the experiments one has to understand the transport properties of the thin films without the presence of water. During preliminary work it turned out that even small amounts of water in the gas atmosphere around the thin films can have significant influence on the measured thin film conductivity. Thus, it will be necessary to discuss the influence of grain sizes and grain boundary density on the ceria thin film with and without zirconium doping under dry conditions as well. The respective literature is going to be discussed in section 2.2 and 2.3.

Going through the literature the reader will soon recognize that reports on the influence of humidity on ceria based thin films are rare, whereas literature on bulk samples, mostly pressed pellets of micro- or nanocrystalline powders prepared by classical solid state routes or wet chemical solution precipitation methods, is quite frequent. Thus, one general question that will be discussed on the basis of the experimental results in this work is whether there is a difference in the response of a polycrystalline bulk sample of similar mean crystallite size. In literature, which will in detail be discussed in section 2.3, there are reports by various groups on an enhanced conductivity in an intermediate temperature regime between 200 – 400 °C. Different models are proposed to explain the origin of the conductivity enhancement. One model is the concept of grain boundaries as a pathway for protons leading to an enhanced conductivity in materials with a high grain boundary density, especially nanocrystalline dense pellets.<sup>45</sup> Another model argues that capillary condensation effects are responsible for the enhanced conductivity between 200 – 400 °C. The open porosity in nanocrystalline pellets

exhibits a high surface area substrate having radii in the nanometer regime, leading to high capillary forces, so that water condenses in the pores.<sup>46</sup>

Thus, an important question that arises from this discussion is whether nanometer sized pores or grain boundaries are the pathways for protons leading to an enhanced conductivity in the temperature regime between 200 – 550 °C. In order to answer this question measurements on polycrystalline thin film samples with different crystallite sizes are going to be conducted for a wide water partial pressure regime. The water partial pressure regime used for most studies in literature only cover a narrow partial pressure regime addressing similar research questions.<sup>38,47–50</sup> For a detailed literature overview on this aspect the reader is referred to chapter 2.3.1. Polycrystalline pressed powder samples or pellets discussed in literature are never fully dense, they always show residual pore volume, either on purpose or due to experimental limitations in the sintering process.<sup>46,49,51–58</sup> This adds additional complexity to the systems under investigation in literature. Therefore, polycrystalline thin films are the ideal model system to answer the aforementioned question in more detail.

In order to achieve a holistic picture on the interaction of ceria based thin films with humidified atmosphere a large temperature range was investigated. Thus, not only effects in the temperature regime between 200 and 550 °C were observed. Lowering the temperature below 150 °C we find similar effects to those already reported in literature for pressed pellets of CZO materials mostly.<sup>37,42,46,53,57,59,60</sup> The origin of the reported conductivity enhancement observed in those works remains unclear. Therefore, it is the aim of this work to add a systematical study to the existing literature, using thin film samples based on  $\text{Ce}_{1-x}\text{Zr}_x\text{O}_2$  with defined morphology. It is reasonable to assume that the proton conductivity at low temperatures does not occur in the solid phase, but within a chemisorbed or physisorbed water layer. This is going to be addressed by the project presented in this thesis as well.

In this context it will be important to address the question whether protons propagate through the grain boundaries of the columnar CZO thin films, or whether adsorption of water on the surface leads to an enhancement in conductivity by forming a water layer in which the mobility of protons is enhanced. In order to answer this question, a systematical variation of the atmosphere humidity applied over a wide range of water partial pressure is necessary. The resulting data for the conductance as a function of water partial pressure then needs to be described by a suitable model. Such a model could be found by applying adsorption isotherms.<sup>38</sup>

Deduced from the aforementioned research questions on the influence of humidity on the conductivity of ceria based thin films in the two different temperature regimes, another topic shall also be addressed in this work. It is crucial to understand whether the water

adsorption is affected by the composition and/or morphology of the CZO thin films within the different temperature regimes. Answering this question, the possibility to tune the surface roughness and the composition of the  $\text{Ce}_{1-x}\text{Zr}_x\text{O}_2$  thin films is essential. Modifying the surface properties may reveal new information on the nature of the process leading to the conductivity enhancement in the different temperature regimes. It is possible that the surface energy is changed by surface roughness or composition, leading to a different energy landscape for physisorption or chemisorption processes.

From the research questions introduced a work plan is derived, that is going to be described briefly in the following paragraphs, in order to give the interested reader an impression about the time and effort that is necessary to conduct a similar research project.

First of all, sintered pellets of the desired compositions had to be prepared and characterized in order to use them as pulsed laser deposition (PLD) targets for the thin film preparation. For the target preparation classical solid state synthesis routes are used. Starting materials are mixed and ball milled, pressed into a pellet and sintered. Once pure and well characterized samples exist, thin films are prepared by pulsed laser deposition. The variation of ablating parameters during the PLD process is a tool for varying the thin film morphology in a controlled manner.

Targets and samples need to be analyzed according to their chemical and crystallographic properties. For both, the thin films and the targets, an analysis by scanning electron microscopy (SEM), x-ray diffraction (XRD), grazing incidence x-ray diffraction (GI-XRD) and scanning probe microscopy (SPM) should give sufficient information on the crystallography and morphology, the film thickness as well as its surface roughness. In addition to this standard procedure some additional methods can be applied in order to ensure a precise knowledge of the chemical composition of the thin films. Here energy-dispersive X-ray spectroscopy (EDS), Raman spectroscopy and X-ray photoelectron spectroscopy (XPS) are powerful techniques. Raman spectroscopy can give information on the crystal structure of the targets and whether the sintering process was successful for the targets. A drawback of EDS and Raman is the fact that the sampling depth is approximately one order of magnitude higher than the thin film thicknesses prepared for this work. Thus one has to be careful concerning the interpretation of the data recorded on thin films with these methods.

The thin films need to be analyzed by SEM, XRD, GI-XRD and AFM before and after the EIS measurements in order to check, whether the thin film morphology changes under the treatment during the EIS measurements. Any morphology changes should be suppressed by suitable pre-treatment of the thin film samples, as a change in morphology or crystallinity could distort the interpretation of the EIS data.

It is one major goal of this work to determine the electrical properties of CZO thin films as a function of the temperature as well as water and oxygen activity. For this purpose a setup needed to be designed, that is capable of keeping the temperature constant between 30 °C – 550 °C and deliver a controllable gas atmosphere regarding oxygen ( $pO_2$ ) and water partial pressure. Within this setup the thin films need to be electrically contacted. As an electrical contact a platinum interdigital microelectrode is chosen in this work. The sample resistance of the CZO thin films is given by the specific conductivity  $\sigma$  [S/cm] and the sample geometry using this type of electrode, as it will be described in chapter 3.3.2. Such a classical electrode with realizable electrode distances  $d$  of approximately 0.5 mm – 10 mm and 10 mm electrode length  $l$  would result in a cell constant larger than  $5000 \text{ cm}^{-1}$ , assuming a thin film thickness  $t$  of 100 nm. Assuming that impedances in an appropriate setup could be measured up to  $10^{10} \Omega$ , this would correspond to conductivities of about  $10^{-7} \text{ S/cm} - 10^{-8} \text{ S/cm}$ . These values are about two orders of magnitudes higher compared to conductivities given for CZO thin films in literature.<sup>21,54,61</sup> This difference can be overcome by the use of interdigital microelectrodes. The interdigital electrode has the advantage of a geometric cell constant  $Z = d/(lh)$  ranging from approximately  $10 - 100 \text{ cm}^{-1}$ , which is one to two orders of magnitude lower than a platinum electrode prepared by using a classical mask or metal paste, so that  $10^{-9} \text{ S/cm} - 10^{-10} \text{ S/cm}$  are detectable. For these electrodes it is important that the electrode distance is larger than the film thickness ( $h < d$ ), as simulated by Hertz et al.<sup>62</sup> The interdigital microelectrode was prepared on top of the thin films by photolithographic methods. As the resists and recipes in photolithography are typically standardized for silicon as a substrate, a parameter set for the photolithographic process on CZO thin films needs to be established by a try and error approach based on the former work by Pascal Hartmann.<sup>4</sup>

When adequate preparation parameters for the photolithographic procedure are found, electrochemical impedance spectroscopy measurements can be carried out on the samples. As these measurements will take several hours per temperature step, an automatic measurement routine needs to be programmed with the impedance bridge software in combination with a *LabView* routine. For controlling and monitoring the gas atmosphere a gas tight tube furnace is used to perform the measurements in. For a precise measurement of the electrical properties of the sample under test, consisting of the thin film with its interdigital platinum electrodes and the electrical wiring, one has to contact and shield the samples in a way that interference from external fields is suppressed as far as possible.

In order to address the research questions, several measurement series were performed under variation of the oxygen and water partial pressures in a temperature range between 30 °C – 550 °C on  $\text{CeO}_2$  (10CZO),  $\text{Ce}_{0.8}\text{Zr}_{0.2}\text{O}_2$  (8CZO) and  $\text{Ce}_{0.6}\text{Zr}_{0.4}\text{O}_2$  (6CZO) thin

films. The data collected is afterwards going to be interpreted regarding the different research questions and if necessary correlated to the information given by the morphological and structural analysis before and after the impedance measurements. In order to be able to understand the data and its correlation with the sample properties, the defect chemistry of ceria based ceramics needs to be considered. This is going to be introduced briefly in chapter 2. Here general aspects of the defect chemistry of bulk ceria are introduced in section 2.1. Based on this the defect chemistry in the vicinity of interfaces and surfaces is introduced in section 2.2. Finally, the influence of water on the properties of these interfaces will be discussed on the basis of various works published in the last decades in section 2.3.

## 2 Theory and state of research

Cerium(IV) oxide, also known as ceria, ceric oxide, cerium oxide or cerium dioxide is a pale white-yellow powder. Cerium is one of the first four elements in the group of the 15 lanthanide elements. These first four elements are referred to as the ceric or light rare-earths. The remaining lanthanides are called the yttric or heavy rare-earths.<sup>63</sup> Rare-earth minerals occur in igneous, sedimentary and metamorphic rocks. Commercially relevant cerium ores are Bastnasite, Loparite, and Monazite.<sup>64</sup> With about 0.0046 wt % of the Earth's crust, cerium is the most abundant element of the heavy rare-earths.<sup>1</sup> It is characterized by having two stable valence states with the oxidation number +IV and +III. This property is used in the production and purification processes of cerium from the ores. Cerium(IV) oxide is an intermediate product of this purification processes.

For many technical applications of ceria-zirconia based materials mentioned in the introduction, as well as in the respective research, the influence of water or protons has mostly been ignored in the past. During the last decade finally some activities in this regard were started. In the last years, proton conductivity and the influence of water on ceria and zirconia based solid mixed ionic electronic conductors (MIEC) had been addressed in research. In section 2.3 the ongoing discussion on the effect of humidity in the gas atmosphere on the conductivity processes is presented. Here one has to distinguish between two temperature regimes, as the possible mechanisms influencing the sample are different. Prior to the discussion on the influence of humidity, the defect chemistry of ceria and zirconia doped ceria is briefly introduced in section 2.1. With this in mind, the importance of interfaces in systems with small crystallite sizes is discussed in section 2.2.

### 2.1 Defect chemistry of $\text{CeO}_2$ and $\text{Ce}_{1-x}\text{Zr}_x\text{O}_2$

Before the influence of protons and/or water will be discussed, the defect chemistry of  $\text{CeO}_2$  and  $\text{Ce}_{1-x}\text{Zr}_x\text{O}_2$  is briefly recapitulated in the following section.

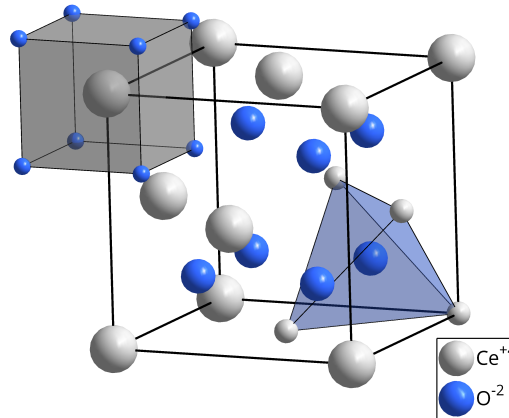
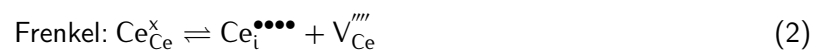
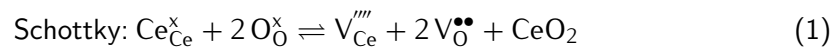


**Figure 2.1:** Cubic fluorite structure of  $\text{CeO}_2$  based on the crystallographic open database number 9009008.<sup>66–70</sup>

### 2.1.1 Pure Ceria

Ceria crystallizes in a cubic structure of  $\text{CaF}_2$  type. Its space group  $Fm\bar{3}m$  is a face centered cubic unit cell. A representation of the unit cell is shown in figure 2.1. The cerium cation is tetrahedrally coordinated by eight equivalent oxygen anions sitting at the corners of a cube. As the octahedral sites are unoccupied, the anion sub-lattice is a cubic primitive cell. The coordination polyhedra of the anions and cations are corner sharing.<sup>65</sup> This phase is stable up to 1300 °C for the stoichiometric compound  $\text{CeO}_2$ . Nevertheless, at elevated temperatures ceria tends to exorporate oxygen, forming a non-stoichiometric compound  $\text{CeO}_{2-\delta}$ .  $\text{Ce}(+IV)$  cations are reduced to  $\text{Ce}(+III)$  ions in order to balance the charges missing when  $\delta$  oxygen ions are excorporated.<sup>64</sup> The driving force behind this process is the oxygen activity within the material, that tends to balance with the oxygen activity in the gas phase. Due to this driving force intrinsic defects form in the material. These defects can be described using the Kröger-Vink notation<sup>71,72</sup>:



From an energetic point of view the Anti-Frenkel defects (3) are the most favorable defect type, leading to the formation of oxygen vacancies ( $V_O^{\bullet\bullet}$ ) and oxygen interstitials ( $O_i''$ ) in relatively low concentrations, without producing any deviation from the stoichiometric composition.

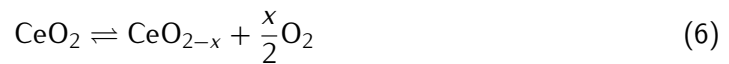
The defect equilibria can be influenced by the surrounding atmosphere. Electronic defects in the form of electrons in the conduction band and holes in the valence band are hardly created intrinsically due to the large band gap of 3–3.6 eV.<sup>73,74</sup> In a reducing gaseous atmosphere ceria gets reduced, which can be described by the equation:



0.5x moles of atomic oxygen are removed from the lattice, while the corresponding number (x moles) of  $O^{2-}$  sites are occupied by x moles oxygen vacancies. This leaves (2 - x) moles of oxygen ions in their original position. The oxygen vacancies formed lead to an overall positive charge in the crystal. Therefore, 2x moles excess electrons ( $\text{Ce}'_{\text{Ce}}$ ) per removed oxygen ion are formed. They are associated with two cerium atoms resulting in a change of charge from +IV ( $\text{Ce}_{\text{Ce}}$ ) to +III ( $\text{Ce}'_{\text{Ce}}$ ).



The two excess electrons can contribute to the electronic charge transfer in the form of small polaron hopping. Usually the mobilities of electrons are orders of magnitude larger than the ionic mobilities ( $\mu_e \gg \mu_{V_O^{\bullet\bullet}}$ ). Therefore, a deviation from stoichiometry does not lead to mixed conduction. However, in cerium dioxide the  $\mu_e$  is reduced due to the formation of small polarons, which can only migrate to an adjacent site by an activated hopping process. The resulting electron mobility is in the order of  $10^{-4} - 10^{-2} \text{ cm}^2/\text{Vs}$ .<sup>10,14,64</sup> This is only one too two orders of magnitude larger than typical ionic mobilities for CeO<sub>2</sub>- based samples, which explains the mixed ionic electronic character of ceria based oxides. Equation (4) can more generally be described by:



An important part of research in solid state ionics is the identification which kind of defects are present. The oxygen partial pressure dependence of conductivity data can be taken into account in order to distinguish between the different possibilities for a given system. For oxygen vacancies being the predominant defect one would expect a  $p_{\text{O}_2}^{-1/6}$  dependency of the conductivity over the whole oxygen partial pressure range.<sup>29</sup> These findings are affirmed in

other studies by more direct methods, like oxygen diffusion data<sup>75</sup> or neutron scattering data<sup>76</sup> for example.

### 2.1.2 The solid solution $\text{Ce}_{1-x}\text{Zr}_x\text{O}_2$ and its defect chemistry

As  $\text{Ce}_{1-x}\text{Zr}_x\text{O}_2$  solid solutions are very important for SOFCs, the phase diagram of this system was intensively studied since the 1950s.<sup>77–80</sup> The phase diagram is quite complex and still discussed in literature. This is due to the fact that already small amounts of cation doping leads to the stabilization of either a tetragonal or a cubic phase. Figure 2.2 shows the phase classification by Yashima et al., which was later adopted by other groups.<sup>81–83</sup>

As shown in the phase diagram below 1273 K the phase diagram shows a cubic (c) symmetry for  $\text{CeO}_2$  molar contents of larger than 80%. Below 1–2 mol-% of  $\text{CeO}_2$  there is a small region of monoclinic symmetry, like in pure  $\text{ZrO}_2$ . The intermediate region is still not completely clarified. In this region a number of tetragonal phases are reported, some of which are stable, some meta-stable.<sup>82–84</sup> Tetragonality occurs when the cubic fluorite lattice of ceria becomes critically strained due to an increasing concentration of smaller zirconium cations. The distortion occurs at the metal-oxygen bond length, leading to a decreasing coordination number of  $\text{Zr}^{4+}$  ions. In the monoclinic phase the coordination number is decreased to seven. It is very difficult to experimentally distinguish the different tetragonal phases in the miscibility gap. The  $t''$  phase is characterized by a displacement of the oxygen atoms from their initial positions in the cubic phase, which is why this tetragonal phase is often referred to as pseudo-cubic. The smaller the particle size of a  $\text{Ce}_{1-x}\text{Zr}_x\text{O}_2$  solid solution becomes the higher is the solubility of  $\text{ZrO}_2$  in cubic ceria. This effect could be important when analyzing

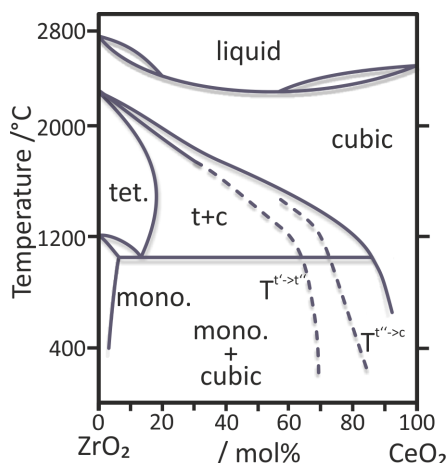


Figure 2.2: Phase diagram of the  $\text{Ce}_{1-x}\text{Zr}_x\text{O}_2$  system. Adapted from Varez et al.<sup>84</sup>

the Ce<sub>1-x</sub>Zr<sub>x</sub>O<sub>2</sub> thin films prepared within this project.

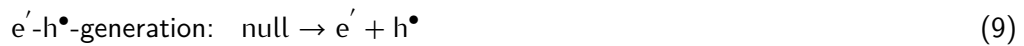
A large number of possible compositions of the CeO<sub>2</sub>–ZrO<sub>2</sub> solid solutions have been investigated in recent years.<sup>1,4,6,19,24,61,76,78,80,85–90</sup> Single phase zirconium-rich and single phase cerium-rich crystals, polycrystalline powders and layers, as well as mesoporous films were prepared and characterized structurally, electrochemically, and with respect to their catalytic activity. A lot of research was also carried out within the miscibility gap, in which phase transitions or also phase separation occurs. On the basis of the expected properties concerning the ion transport and the oxygen exchange, the compositions Ce<sub>0.5</sub>Zr<sub>0.5</sub>O<sub>2-δ</sub> and Ce<sub>0.8</sub>Zr<sub>0.2</sub>O<sub>2-δ</sub> were investigated.<sup>91</sup> Additionally, using neutron scattering data, Mamontov et al. were able to show that local inhomogenities may be present in Ce<sub>1-x</sub>Zr<sub>x</sub>O<sub>2-δ</sub> solid solutions, leading to domains with different compositions, that are not detectable with XRD experiments.<sup>92</sup> The smaller the particle size of a CeO<sub>2</sub>–ZrO<sub>2</sub> solid solution becomes the higher the solubility of ZrO<sub>2</sub> in cubic ceria is. This effect could be important when analyzing the CeO<sub>2</sub>–ZrO<sub>2</sub> thin films prepared within this project.<sup>81,82,84</sup>

The described structural changes are often accompanied by changes in the electrical properties as a function of composition and oxygen activity in the material and surrounding atmosphere. This can be understood by a suitable defect and transport model, which is described in the following paragraph. As Zr does not change its valence (+IV) as a function of temperature or oxygen activity, the defect chemistry is similar to that of pure ceria. The Anti-Frenkel reaction, the cerium reduction reaction, and electron-hole pair generation are formulated below together with the corresponding mass action law.

#### Intrinsic defects

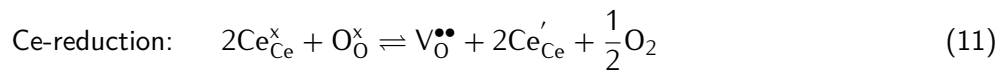


$$[\text{V}_\text{O}^{\bullet\bullet}][\text{O}_\text{i}''] = K_{\text{AF}}(T) = \exp\left(-\frac{\Delta H_{\text{AF}}}{k_B T} + \frac{\Delta S_{\text{AF}}}{k_B}\right) \quad (8)$$



$$[e'][h^\bullet] = K_e(T) = N_C N_V \exp\left(\frac{-E_g}{k_B T}\right) \quad (10)$$

#### Extrinsic defects



$$[\text{V}_\text{O}^{\bullet\bullet}][\text{Ce}'_{\text{Ce}}]^2 p\text{O}_2^{1/2} = K_{\text{Red}}(T) = \exp\left(-\frac{\Delta H_{\text{Red}}}{k_B T} + \frac{\Delta S_{\text{Red}}}{k_B}\right) \quad (12)$$

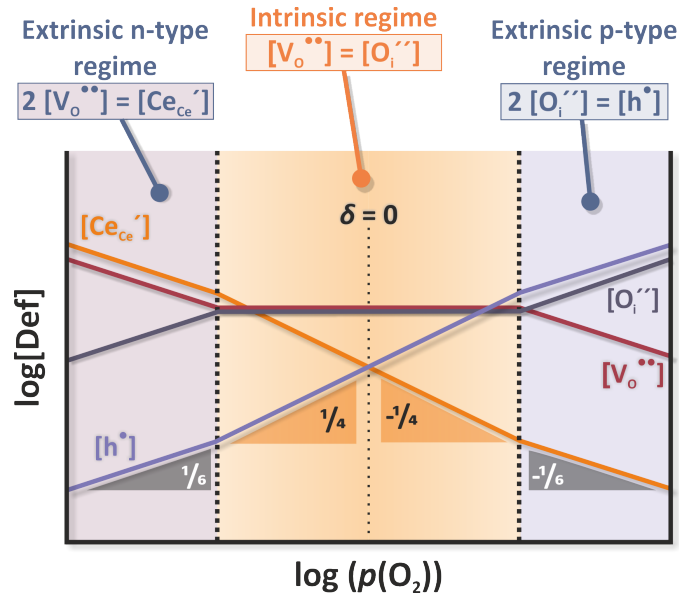


Figure 2.3: Brouwer diagram of  $Ce_{1-x}Zr_xO_{2-\delta}$ .

Here, the concentration of oxide ions on oxide sites  $[O_O^x]$ , and the concentration of cerium ions on cerium sites  $[Ce_{Ce}^x]$  are approximated to be constant and thus hidden in the mass action law constant.  $V_o^{..}$  are oxygen vacancies carrying two positive charges,  $O_i^{''}$  are two times negatively charged oxygen interstitials and  $Ce_{Ce}^{\cdot}$  are small polarons (quasi localized electrons) on Ce ion sites.  $\Delta H_{Red}$  and  $\Delta S_{Red}$  stand for the entropy and enthalpy of reduction in equation (12) and  $\Delta H_{AF}$  and  $\Delta S_{AF}$  describe the entropy and enthalpy of Anti-Frenkel pair generation in equation (8).  $E_g$  is the band gap and  $N_V$  and  $N_C$  are the valence and conduction band density of states in equation (10). "null" in equation (9) denotes that the electron-hole pairs are generated from a virtually perfect crystal lattice.  $K_{AF}$ ,  $K_{Red}$  and  $K_e$  are the equilibrium constants of the respective process. Using the charge neutrality equation given for the different regimes in figure 2.3, one can derive the defect mass action law equations above and generate a Brouwer diagram. From this diagram it is possible to estimate the dominant charge carriers at a certain oxygen activity. The dominant charge carrier species can be related to a measured conductivity of a sample under the respective  $pO_2$  atmosphere, being a measure of the oxygen activity.

From this simple picture one can assume that charge transport in a mixed ionic electronic conductor is dominated by the majority defects in the sample.

$$\sigma = \sigma_e + \sigma_i = e_0 \mu_e n + e_0 Z_i \mu_i [i] \quad (13)$$

Albeit, as electronic conductivity is given by the sum of electronic and ionic conductivity it becomes obvious, that the charge carrier concentration  $[i]$  and  $n$ , as well as the mobilities  $\mu_i$  and  $\mu_e$  need to be accounted for to determine the overall conductivity of the material. In the case of CZO the electric transport below the stoichiometric composition composes from the ionic contribution of anion movement in the anions sublattice, and an electronic contribution resulting from small polaron hopping. Charge transport can be described by a simple random walk diffusion law. Assuming a one-dimensional case the diffusion coefficient  $D_i$  is given by the jump frequency  $\omega_i$  of the charge carrier and the distance to be overcome by each jump, represented by the lattice constant  $a$ .

$$D_i = \frac{1}{2} \cdot \omega_i \cdot a^2. \quad (14)$$

Since both transport processes in cerium dioxide, the small polaron hopping and the ionic transport, represent an activated process, the temperature dependence of the random walk diffusion and thus the Nernst-Einstein relationship for the electrical conductivity is a function of the activation energy  $E_A$  and temperature according to equation (15):

$$\sigma = \frac{\sigma_0}{T} \cdot \exp\left(-\frac{E_A}{k_B T}\right) \quad (15)$$

The pre-exponential factor  $\sigma_0$  includes the attempt frequency, the lattice constant and a term for the entropy of migration  $\Delta S_m$ . Equation (15) includes extrinsic and intrinsic defect formation. The difference between those two cases is that in the extrinsic regime the Anti-Frenkel defect formation enthalpy  $\Delta H_{AF}$  also contributes to the activation energy.  $E_A$  is not equal to the migration enthalpy  $\Delta H_m$  anymore, as in the intrinsic case, but is given by the sum of the migration and the formation energy, as follows:

$$\text{Intrinsic regime} \quad E_A = \Delta H_m \quad (16)$$

$$\text{Extrinsic regime} \quad E_A = \Delta H_m + \frac{\Delta H_{AF}}{2} \quad (17)$$

This becomes important when discussing the influence of grain size and interfaces on the transport properties as  $\Delta H_m$  as well as  $\Delta H_{AF}$  can be influenced by interface effects. These aspects are discussed in section 2.2.

## 2.2 Defect chemistry in the vicinity of interfaces

When using polycrystalline thin films as model systems for conductivity measurements, one has to account for the effects space charge layers (SCL) have on the transport processes within and in between single grains. It is known from experiments on SrTiO<sub>3</sub> bi-crystals, that the misorientation angle between two adjacent grains determines their conductivity.<sup>93</sup> Maier was the first scientist to propose a space charge formalism for the quantitative treatment of ionic conduction at interfaces in 1985.<sup>94</sup> The methods he used were later applied to acceptor doped ceria by Tschöpe et al. in 2001.<sup>95,96</sup> Tschöpe proposed a model to explain the electrical conductivity of polycrystalline cerium oxide. This model will be explained in the following based on the respective publications.<sup>97</sup>

From experiments described in a first paper Tschöpe found that the oxygen partial pressure dependence of the bulk conductivity changes drastically, reducing the grain size in a disc shape pressed pellet of Gd doped CeO<sub>2</sub> from micrometer regime to the nanometer regime.<sup>95</sup> The main results are presented in two graphs taken from this paper in figure 2.4. The conductivity of the microcrystalline sample shows no oxygen partial pressure dependence. In contrast to that the nanocrystalline sample follows a power law with an exponent of  $-1/6$  and has a one to two orders of magnitudes lower conductivity. Additionally, the activation energy of the conductivity mechanism, determined for the nanocrystalline sample, was 1 eV higher.

The behavior of the microcrystalline sample can be explained by the standard defect model for acceptor doped ceria. The sample shows no pO<sub>2</sub> dependence in conductivity. Thus, the oxygen vacancy concentration is constant due to the acceptor doping ( $[V_O^{\bullet\bullet}] = \frac{1}{2}[A'_{Ce}]$ ). In order to explain the  $-1/6$  power law dependence of the nanocrystalline sample Tschöpe argues that such a behavior is expected for the Brouwer approximation (charge neutrality equation), that applies at low pO<sub>2</sub> for the extrinsic regime of the CeO<sub>2</sub> Brouwer diagram (figure 2.3 on page 14) ( $2[V_O^{\bullet\bullet}] = [Ce'_{Ce}]$ ). In this regime oxygen vacancies and electrons are controlled by the external equilibrium with the gas phase. In the nanocrystalline samples the electronic conductivity exceeds the ionic conductivity, due to the higher mobility of the small polarons compared to that of the oxygen vacancies. Tschöpe explains this phenomenon by an enrichment of aliovalent cations and acceptors in the SCL along the grain boundaries. This leads to a decreased ionic and increased electronic partial conductivity which is observed in the experiments. From these results Tschöpe developed a model for the effect of SCL on the grain size dependent conductivities in MIEC's.<sup>96</sup>

According to the space charge theory a space charge potential is the consequence of thermodynamic equilibrium. In the vicinity of an interface, the concentration of each type of

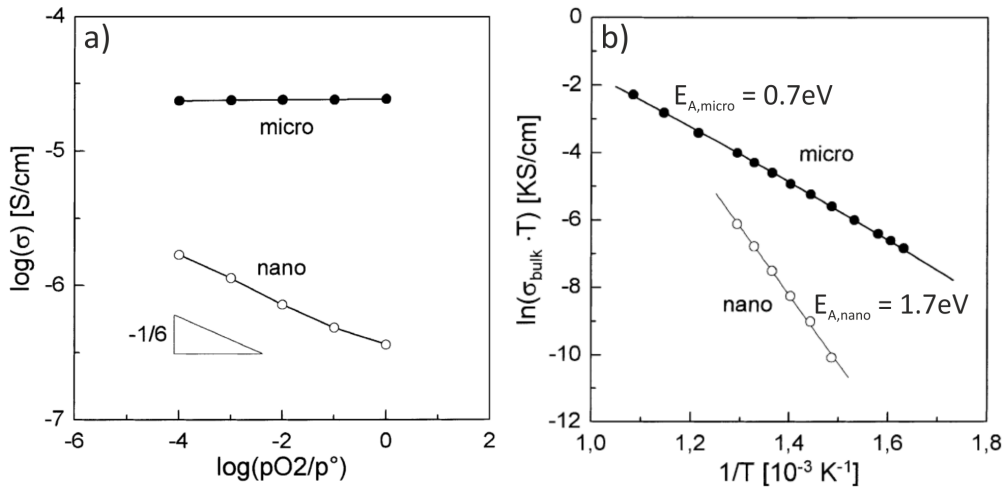


**Figure 2.4:** Experimental results of Tschöpe<sup>95</sup> reprinted with permission from Elsevier: a) Bulk conductivity of micro- and nanocrystalline CeO<sub>2</sub> at 500 °C as a function of oxygen partial pressure. b) Temperature dependence of bulk conductivity of microcrystalline CeO<sub>2</sub> at  $p_{O_2}/p = 10^{-4}$ .

defect is controlled by the difference in standard chemical potential of the defect between bulk and interface core.<sup>18</sup> The defect charges result in a certain space charge density in the crystal with an equal charge of opposite sign at the interface core. This leads to a potential difference  $\phi$  between the interior of the crystal and the defect source, the so called space-charge potential. In order to achieve charge neutrality inside the crystal the concentrations of charged point defects are not constant along the cross-section of a grain. This depletion or accumulation of charge carriers in the vicinity of interfaces imposes significant changes on the transport processes, resulting in a certain electrical response of a polycrystalline ionic conductor. Tschöpe adopted the formalism used in the Gouy-Chapman theory for liquid electrolytes in order to describe the point defect concentrations, taking the bulk concentrations as a reference derived from the mass action laws in combination with the charge neutrality condition as shown in figure 2.5 into consideration.<sup>98–101</sup>

This model can be adopted to a polycrystalline material, allowing to estimate the space charge region volume fraction  $\psi_{sc}$  of a cubic crystal with the side length  $L$  and the space charge layer thickness  $b$  to

$$\psi_{sc} = 6 \frac{b}{L}. \quad (18)$$

When minority charge carriers accumulate in the space charge layer a short circuit path is formed and the corresponding partial conductivity increases. Measuring impedance spectra of such a system, parallel SCL and bulk response merge into one semi-circle and might no

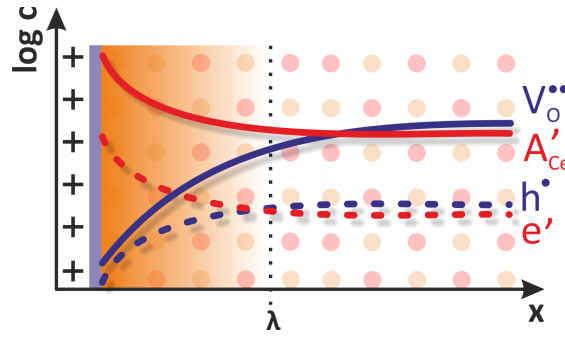


**Figure 2.5:** Concentration profiles for point defects of charge  $z = \pm 1, 2$  in an exemplary positive space charge potential. Figure adopted from Tschöpe et al..<sup>96,102</sup>

longer be separated. figure 2.5 shows the concentration profile of a point defect  $c_i(x)$  at the distance  $x$  from a grain boundary in a material with a point defect concentration  $c_{i0}$  in the bulk given by

$$\frac{c_i(x)}{c_{i0}} = c_{i0} \left( \frac{1 + \Theta \exp(-x/\lambda)}{1 - \Theta \exp(-x/\lambda)} \right)^{2z_i} \quad (19)$$

$\lambda$  is the screening length, correlated with the permittivity of the bulk.  $\Theta$  is a profile parameter related to the potential difference across the space charge ( $\Phi$ ). The defect charge number  $z_i$  contributes to the exponent, which makes the profiles of negatively and positively charged defects inverse to each other. In addition the depletion or enhancement effect increases with the power of the defect charge (see figure 2.5). Assuming a positive space charge potential, the concentration of positively charged defects  $[V_O^{\bullet\bullet}]$  or  $[h^{\bullet}]$  is decreased, while the electron concentration  $[e']$  and the negative acceptor defect concentration  $[A'_{Ce}]$ , which is never zero in a realistic material, is increased. This leads to an enhancement of the partial electronic conductance in the space charge region. With decreasing grain size, a transition between the dominant ionic to electronic conduction is obtained. As a consequence one can find a change of the exponent  $1/n$  of the power law dependence

$$\sigma \propto p_{O_2}^{-1/n} \quad (20)$$

as a function of the grain size, as shown in figure 2.6. As the exponent decreases, the activation energy for the electronic conduction process has to decrease as well, while the activation energy of the ionic process increases. The space charge model predicts though, that the partial pressure dependence of the conductivity becomes weaker with decreasing grain size.

The space charge model as presented here is derived under the assumption that the grain size  $L$  is much larger than the screening length  $\lambda$ . For ceria the minimal grain size at which

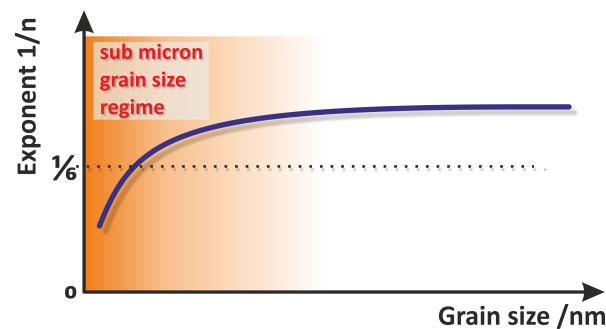


**Figure 2.6:** Change of the exponent  $n$  in the power-law dependence of the electronic conductivity  $\sigma \propto p_{\text{O}_2}^{-1/n}$  as a function of grain size of slightly acceptor doped ceria at  $T = 500^\circ\text{C}$ . Adopted from Tschöpe et al.<sup>96</sup>.

the space charge layer model is applicable is around 80 nm. When the grain size is in the sub-micrometer range, the equilibrium potential distribution needs to be calculated numerically. This is only possible when the defect formation Gibbs free energies are known. The Gibbs formation energy of oxygen vacancies in the grain boundary core is lower than in the bulk.<sup>93,103</sup> Thus, the grain boundary core exhibits an highly enriched vacancy concentration, which is plausible, as the grain boundary core is the space in between to grains, free from any lattice atoms. In the vicinity of this positive charge the Gibbs free energy of the oxygen vacancies is higher than in the bulk region, which is not influenced by the charge at the interface. The smaller the crystallites, the smaller the region becomes in which the oxygen vacancies are not influenced. When the crystal size gets as small as the screening length, it is found that the whole crystal is penetrated by the space charge, as shown in figure 2.7.<sup>97,102</sup> The space charge layers from opposite grain boundaries overlap leading to a different defect concentration distribution as it is found in the case that  $L \gg \lambda$ . The concentration throughout the cross section of the crystallite becomes constant, thus describing the upper limit to which the electrical conductivity will increase when grain size is reduced.

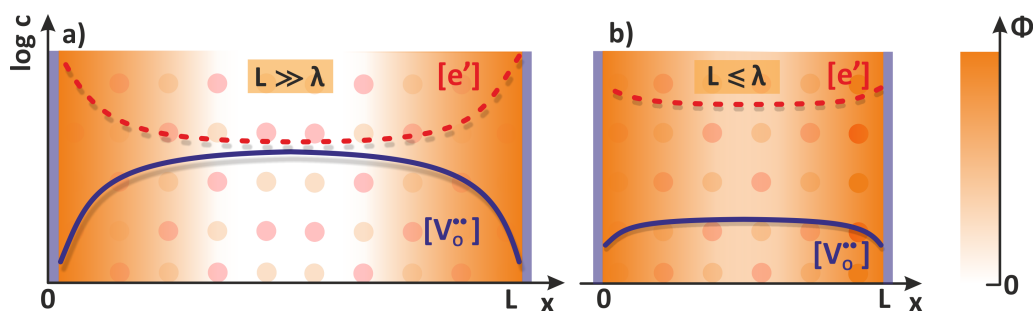


**Figure 2.7:** Schematic defect concentration distribution for electrons and oxygen vacancies within a nanoscopic grain for a)  $L \gg \lambda$  and b)  $L \leq \lambda$ . The space charge potential  $\Phi$  changes along the grain radius as shown by the scale bar on the right.<sup>97,102</sup>

In 2009 De Souza presented a model to calculate the magnitude of the enrichment of vacancies in the grain boundary core, based on the thermodynamic grain boundary model.<sup>93</sup> There are two drawbacks of this model by Tschöpe et al. and the extension by De Souza. The first is, that for overlapping space charge regions in nanometer scale grains no reference level inside the grain exists for the space charge potential, which makes it impossible to calculate “true” defect concentrations. The other drawback is that the effect of an applied bias to the sample also leads to a gradient in the bulk electrical potential. Here a reference potential would also be needed to describe the conditions in a small grain correctly. Van Laethem et al. provided a new solution strategy for this problem by using numerical methods.<sup>104</sup> They were able to calculate the grain boundary charge a priori in the absence of space charge layer overlap. Further, they provide a iterative calculation of the grain boundary charge in the presence of an overlap. A comparison of these simulations to literature data shows, that the model applied is not sufficient. Laethem et al. state that the inclusion of dopant-vacancy interaction as well as vacancy-vacancy interaction might be necessary. Additionally, the estimation of vacancy formation energies and site densities need to be replaced by data from atomistic simulations, in order to implement the influence of the grain boundary orientation. These improvements are subject to state of the art research in the field of theoretical predictions of the electrical response, showing that the basic model proposed by Tschöpe et al. is a sufficient background for understanding the nature of defect chemistry and transport properties in the vicinity of interfaces.

### 2.3 Influence of water at interfaces

Concerning the fact that for small crystallite sizes the space charge layer determines the electrical behavior of a nanocrystalline sample, one has to take into account how the space charge layer, and with that the defect chemistry, is influenced from the gas atmosphere at the interface. Here, not only the oxygen activity is of interest for a mixed ionic electronic conductor like CZO. Water at the interface, which is practically present in any technical relevant process, can also have a significant influence on the electrical conductivity, as an alternative pathway for conduction might be formed by protons moving in a chemisorbed or physisorbed layer at the interface. For a deeper understanding of that influence two temperature regimes need to be discussed, below and above 200 °C approximately.

In order to discuss the results and get a better understanding of the physicochemical processes, typical adsorption models are introduced in the following section, considering the two most prominent adsorption isotherms. This is followed by a summary of the state of

knowledge concerning the interaction of water with nanostructured ceria surfaces, and its impact on the electrical conductivity. This overview does not claim to be exhaustive but a representative summary about the research published on this field in order to give a guideline for the reader for further literature research. Recent advances in the field of solid oxide proton-conducting materials that belong to the class of perovskite-based materials (such as doped  $\text{BaCeO}_3$ ,  $\text{BaZrO}_3$ ,  $\text{BaCeO}_3\text{-BaZrO}_3$ ,  $\text{SrCeO}_3$ , and  $\text{LaScO}_3$ ) and to other classes of materials (such as doped  $\text{Ba}_2\text{In}_2\text{O}_5$  and  $\text{LaNbO}_4$ ) are explicitly excluded in this overview.<sup>105</sup>

### 2.3.1 Physisorption and chemisorption

The formation of water layers on ceramic oxide surfaces depends on the temperature, as well as on the surface properties. Heating results in desorption, while cooling results in adsorption of water from the humid atmosphere. In case the adsorbent is bound to the surface via Van-der-Waals interaction, this type of bonding is referred to as physisorption (acronym for “physical adsorption”). The physisorption enthalpy typically is in the range of the condensation enthalpy of the adsorbent, as the forces involved in the physisorption process are the same than those responsible for the condensation of vapor. Deviations can occur depending on the substrate chemistry and surface structure. An adsorbent that impinges on the surface can transfer the physisorption energy stepwise to the substrate, transforming the energy into heat which is dissipated by the substrate lattice. The adsorbent molecule typically remains intact during this process which is called accommodation.<sup>106</sup> Typical adsorption enthalpies are in the range of 20 – 90 kJ/mol.<sup>107</sup>

In contrast to physisorption the so called chemisorption on cooling the substrate already happens at rather high temperatures (roughly about 300 °C), as the chemisorption enthalpy is typically in the order of 100 – 200 kJ/mol. In this case the adsorbent forms a chemical (typically covalent) bond to the substrate. Thus, the chemisorption enthalpy is of the same order of magnitude as the respective chemical reaction. The adsorbing molecule (adsorptive) can be destroyed during this process. The discrimination between physisorption and chemisorption only by means of the enthalpies is rather imprecise. In order to describe the nature of the adsorption process spectroscopic methods can be used.<sup>106,107</sup>

The gas in the atmosphere is in a dynamic equilibrium with the adsorbent on the surface. Therefore, the surface coverage  $\Theta$  depends on the partial pressure of the adsorptive in the gas phase. This dependence is described by so called adsorption isotherms. These isotherms are models for the adsorption behavior taking the temperature, the partial pressure, and approximations concerning the interaction of the gas molecules and the substrate characteristics into account.

One of the first models describing the adsorption process was developed by Irving Langmuir in 1916.<sup>108</sup> Langmuir studied chemical reactions at low pressures and electron emission when he became interested in the phenomenon of adsorption and developed a theory that had been verified by a large number of experiments since then.<sup>109</sup> Directly influenced from Bragg's work on crystal structures, Langmuir derived that chemically unsaturated atoms at the surface of a solid exist.<sup>110</sup> Gas atoms impinging the surface, condense driven by the force to saturate these surface atoms. The kinetics of this process is described by the rate constant of adsorption  $k_{ad}$ . Once condensed, the molecules or atoms subsequently evaporate from the surface, described by the rate constant of desorption  $k_{des}$ . Langmuir described the dependence of the surface coverage  $\Theta$  of an adsorbed gas  $A$  on the pressure above the surface at a given temperature<sup>108</sup>:



Here  $M$  is a vacant surface site. Given that the coverage of the surface is proportional to the partial pressure  $p$  of  $A$  and to the number of vacant sites, which can be written as  $N(1 - \Theta)$ , with  $N$  being the number of all binding sites available on the uncovered surface, the change of coverage during adsorption with time is given by:

$$\frac{d\Theta}{dt} = k_{ad} p N (1 - \Theta) \quad (22)$$

The desorption is described by:

$$\frac{d\Theta}{dt} = -k_{des} N \Theta \quad (23)$$

Given that  $K = \frac{k_{ad}}{k_{des}}$  when an equilibrium is reached. The Langmuir isotherm can be derived from (22) and (23).

$$\Theta = \frac{K p}{1 + K p} \text{ with } K = \frac{k_{ad}}{k_{des}} = K_0 \exp\left(\frac{\Delta_{ad}H^\ominus}{RT}\right) \quad (24)$$

Figure 2.8 shows Langmuir isotherm plots for different values of  $K$ . The coverage increases with increasing pressure. As  $K$  is temperature dependent, fitting Langmuir isotherms measured at different temperatures by variation of  $K$ , the isosteric adsorption enthalpy can be determined from the van't-Hoff-equation. Langmuir made three assumptions deriving his model. The first is that adsorption only leads to one single monolayer of adsorptive on the adsorbent. Further a ideally flat and homogeneous surface is assumed. All binding sites are equal. The final assumption of the Langmuir model is that the occupation of a neighboring binding site does not influence the ability for adsorption of an adsorptive molecule. Despite

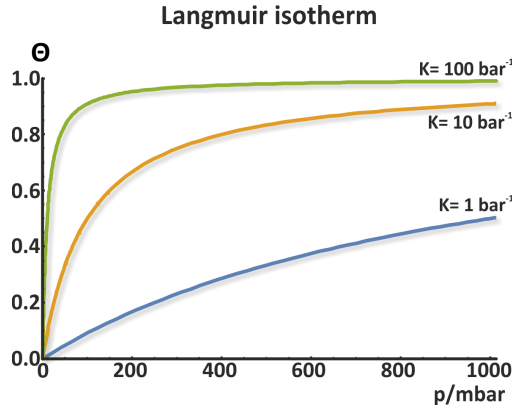


**Figure 2.8:** Langmuir isotherms for different values of  $K$ . The larger  $K$  becomes, due to a decrease in temperature, or a higher enthalpy of adsorption, the lower the partial pressure  $p$  at which the coverage  $\Theta$  gets unity, as described by equation (24).

these assumptions, the Langmuir isotherm typically describes chemisorption processes very well. A typical example for a adsorption process that can be described with the Langmuir isotherm is thus the adsorption of chemically active gases on metal surfaces.

For adsorption of water on metal oxide surfaces one typically observes adsorption of more than one monolayer. For these cases where the heat of adsorption becomes a function of the coverage and multilayer adsorption occurs, other isotherms were derived for the modeling of these processes. The so called BET isotherm, named after Brunauer, Emmett and Teller, who published this in 1938, is basically a generalization of the Langmuir isotherm to multi molecular adsorption.<sup>111</sup> Assuming that at equilibrium the rate of condensation at a given pressure  $p$  on an bare surface area  $s_0$  must remain constant, the condensation rate and the evaporation rate are equal, which is basically described by the Langmuir equation as well.

$$k_{ad,1}ps_0 = k_{des,1}s_1 \exp^{-\Delta_{ad}H_1^\ominus/RT} \quad (25)$$

The heat of adsorption of the first layer with the surface area  $s_0$  is given by  $\Delta_{ad}H_1^\ominus$ .  $k_{ad,1}$  and  $k_{des,1}$  are the rate constants of adsorption and desorption of the first layer and independent of the coverage in this layer.

The next layer  $s_1$  is also assumed to stay constant under given equilibrium conditions. Four different processes need to be taken into account. Condensation on the bare surface ( $k_{ad,1}ps_0$ ), condensation of a second on the first layer ( $k_{ad,2}ps_1$ ), and evaporation from the second ( $k_{des,2}s_2e^{-\Delta_{ad}H_2^\ominus}$ ), as well as first ( $k_{des,1}s_1e^{-\Delta_{ad}H_1^\ominus}$ ) layer. One obtains:

$$k_{ad,2}ps_1 + k_{des,1}s_1e^{-\Delta_{ad}H_1^\ominus/RT} = k_{des,2}s_2e^{-\Delta_{ad}H_2^\ominus/RT} + k_{ad,1}ps_0 \quad (26)$$

Comparing (25) with (26) one obtains that the rate of condensation on the top of the first layer is equal to the evaporation rate from the second layer.

$$a_2 p s_1 = b_2 s_2 e^{-\Delta_{\text{ad}} H_2^\ominus / RT} . \quad (27)$$

This holds true for all consecutive layers  $i$

$$a_i p s_{i-1} = b_i s_i e^{-\Delta_{\text{ad}} H_i^\ominus / RT} . \quad (28)$$

Brunauer, Emmett and Teller assume in their model, that the enthalpy of adsorption  $\Delta_{\text{ad}} H_i^\ominus$  for  $i > 1$  is equal for all layers, except the first one, and equal to the heat of liquification of the adsorptive:

$$\Delta_{\text{ad}} H_i^\ominus = \Delta_{\text{liq}} H^\ominus = -\Delta_{\text{v}} H^\ominus . \quad (29)$$

They also assumed that the adsorption and desorption rate constants for the second and higher layers have a constant ratio  $g$

$$\frac{k_{\text{ad},i}}{k_{\text{des},i}} = g . \quad (30)$$

With  $\Theta = \frac{V}{V_m}$ , where  $V$  is the total volume of gas adsorbed and  $V_m$  the volume of gas adsorbed, when the adsorbent is covered with one layer of adsorptive molecules, Brunauer, Emmett and Teller derived their isotherm equation by summation over all layers  $i$  and the surface areas  $s_i$ ,

$$\Theta = \frac{V}{V_m} = \frac{\sum_{i=0}^{\infty} i s_i}{\sum_{i=0}^{\infty} s_i} . \quad (31)$$

By introducing some abbreviations like

$$c = \frac{k_{\text{ad},1} g}{k_{\text{des},1}} e^{\left( \frac{\Delta_{\text{ad}} H_1^\ominus - \Delta_{\text{cond}} H^\ominus}{RT} \right)} \quad (32)$$

with  $\Delta_{\text{cond}} H^\ominus$  being the condensation enthalpy of the liquid phase of the adsorbate and solving the summations, they obtained

$$\Theta_{\text{BET}} = \frac{V}{V_m} = \frac{c \frac{p}{p_{\text{sat}}}}{\left(1 - \frac{p}{p_{\text{sat}}}\right) \left(1 - (1 - c) \frac{p}{p_{\text{sat}}}\right)} \quad (33)$$

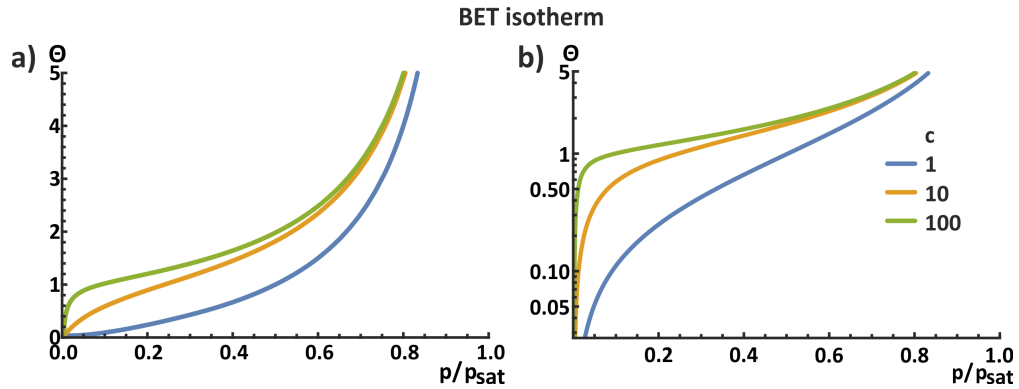


**Figure 2.9:** BET isotherm for different values of  $c$  with a) linear and b) logarithmic scaling of the ordinate. The curve progression can be decomposed into two regions, one below and the other above a coverage of  $\Theta = 1$ . The larger  $c$  becomes, due to an decrease in temperature, or a higher difference between the enthalpy of adsorption of the first layer and the liquification enthalpy, the lower the partial pressure  $p$  at which the coverage  $\Theta$  gets unity, and the tighter the curvature in both regions.

for the BET-equation. This equation results in a S-shaped isotherm. For  $c > 1$  the isotherm has two regions, as shown in figure 2.9. In the low pressure region the isotherm is concave towards the pressure axis and reduces to a special form of the Langmuir isotherm, thus describing the adsorption of a first molecular layer. As the pressure  $p$  approaches  $p_{\text{sat}}$ , the coverage  $\Theta$  becomes large and the curve becomes convex with increasing pressure. For  $p = p_{\text{sat}}$  the BET-equation has a pole, thus becomes infinite. When the coefficient  $c$  becomes large ( $c \gg 1$ ), the BET isotherm can be expressed in the following simplified formalism.

$$\Theta_{\text{BET}} = \frac{1}{1 - \frac{p}{p_{\text{sat}}}}. \quad (34)$$

This expression often is sufficient for describing nonreactive gases on polar surfaces for example, where  $c \approx 100$ . The heat of adsorption of the very first monolayer is large compared to the condensation enthalpy, and adsorption of the second layer occurs as soon as the first layer is filled. For  $c \gg 1$  and  $p \ll 1$  the BET becomes the Langmuir isotherm. Conversely, if  $\Delta_{\text{ad}}H_1^\ominus$  is smaller or equal to  $\Delta_{\text{cond}}H^\ominus$ ,  $c$  becomes small and multilayer adsorption already occurs while the first layer is still incomplete.

Using the Clausius-Clapeyron equation the isosteric heat of adsorption  $\Delta q_{st}$  (differential heat of adsorption) can be determined. The strength of the adsorbate bond determines under which pressure and temperature combination the same coverage is found. Measuring the adsorption of a gas at various temperatures over a certain pressure range of interest thus

gives the isosteric heat of adsorption:

$$\frac{1}{p} \left( \frac{\partial P}{\partial T} \right)_{\theta} = \frac{\Delta q_{st}}{RT^2} \quad (35)$$

The BET-model is based on the following assumptions. (i) The adsorption takes place on fixed sites. (ii) The sites are energetically identical. (iii) No lateral interaction is allowed between the adsorbed molecules. The inclusion of lateral adsorbate-adsorbate interaction leads to the formation of islands.<sup>112</sup>

With the theoretical background described in this section, in the following two sections the state of knowledge about the influence of water on electrical conductivity of ceria based materials is presented. As the driving forces of chemisorption and physisorption are different, the literature is divided into such works, investigating a temperature regime at elevated temperatures ( $T \gtrsim 150^\circ\text{C}$ ) where chemisorption is most likely the relevant process, and those studies with a focus on a lower temperature regime, where physisorption is most likely to occur. Nevertheless, it is emphasized that the transition between the two regime is diffuse.

### 2.3.2 Literature on the influence of humidity on the conductivity of ceria based materials

The first investigations on water adsorption on ceria were published in 1991 by Prin, Pijolat, Soustelle and Touret.<sup>113</sup> They studied the equilibrium between water and cerium dioxide powder by thermogravimetry between 300 and 100 °C. The interpretation of the isotherms revealed two distinct sites that differ in their standard enthalpy of adsorption and in their population for a microporous sample. Water is fixed on the ceria surface. Direct bonds to cerium atoms are formed and hydrogen bonding to hydroxyl groups located in the micropores occurs in samples that are not sintered at high temperatures. When sintering at higher temperatures is used for further densification, the samples do not contain a significant amount of micropores anymore.

Prin et al. determine the enthalpy of direct bonding of water molecules to the ceria atoms in the surface to be between  $-55$  and  $-59 \text{ kJ mol}^{-1}$  for the two different samples under investigation. This implies that these values correspond to the same nature of adsorption site in the two samples. This is confirmed by the fact that the population of this site type is in the same order for both samples (about  $10^{-5} \text{ mol m}^{-2}$ ). A second fixation enthalpy of  $23 \text{ kJ mol}^{-1}$  measured on the microporous sample is attributed to hydrogen groups already present in the sample at the surface of the micropores, to which water molecules are electrostatically bonded. These sites disappear after calcination at elevated temperatures of  $670^\circ\text{C}$ .

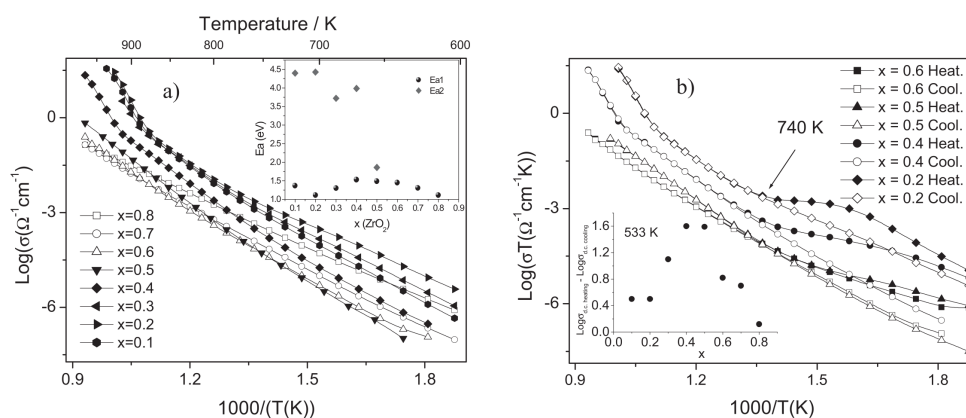


**Figure 2.10:** a) Arrhenius plot of the bulk conductivity determined by Jimenez et al. measured during cooling of the sample. Zirconia rich samples are represented by open symbols. Ceria rich samples are represented by closed symbols. b) Arrhenius plot of heating and cooling cycles. The enhanced conductivity in heating cycles is likely due to residual water in the samples, as they were not stored under dry conditions prior to the first heating cycle.

Measurements are conducted under nominally dry conditions, without drying the carrier gas before streaming into the oven. The residual humidity of 2-3 ppm water content in the gas is sufficient to enhance the conductivity of the samples during the heating cycles. Plots taken from the paper of Jimenez et al. reprinted with permission from John Wiley and Sons.<sup>57</sup>

Jimenez et al. investigated the influence of temperature,  $pO_2$  and  $pH_2O$  relative pressures on the conductivity of a series of  $Ce_{1-x}Zr_xO_2$  ( $0 < x < 1$ ) pressed pellets, prepared by solid-state reaction.<sup>57</sup> The pellets had a relative density of 85% and were contacted with gold electrodes on the larger faces. The temperature range investigated was 120 – 800 °C in heating as well as cooling runs. An YSZ based oxygen pump was used to control and monitor the oxygen partial pressure in the system. A similar setup as it was used for the measurements conducted in the experimental part of the work presented here. Samples were measured under dry and humidified (93% relative humidity) conditions.

Jimenez et al. report a rather complex temperature dependency of the conductivities as a function of temperature, depending on the composition, and whether a heating or cooling experiment was conducted. For cerium-rich pellets two activation energies are found in cooling experiments, as can be seen in figure 2.10. The Arrhenius plots can be divided in two regimes. The first regime is below 850 K approximately, where the slope in the Arrhenius plot is not changing, thus only one activation energy of about 1.5 eV is found, without showing a clear trend with composition. A change in slope is found above 850 K, showing activation energies of 3.75 – 4.5 eV. As Jimenez et al. is not distinct on this aspect the reader has to assume that these measurement cycles were conducted under nominally dry gas conditions with a residual water content of a few ppm. Thus, residual water in the gas atmosphere, which is adsorbed from the laboratory in the open pore volume of about 15%,

most probably influenced the sample conductivity during the heating experiments. Jimenez et al. also conducted measurements in intentionally humidified gas atmosphere. Unfortunately in their paper they did not present the temperature dependence of the conductivity under these conditions. Instead they studied the recovery of the samples conductivity when exposed to humidified gases. They report increasing conductivity in humid gas mixtures, when the sample is held at a constant temperature. Jimenez et al. report that the conductivity of their samples is dominated by electrons. They conclude this from the slopes of the DC conductivity measurements as a function of  $pO_2$ . An additional indicator for the electronically dominated conductivity is the fact that the imaginary part of the impedance vanishes at low frequencies ( $< 1$  Hz), indicating non blocking electrodes, thus a dominant electronic conductivity.

Jimenez et al. argue that water incorporation can be described by the following reaction, describing the formation of hydroxyl defects.



In case of  $Ce_{1-x}Zr_xO_2$  the oxygen vacancy concentration  $[V_O^{\bullet\bullet}]$  is not fixed by the dopant concentration, as in gadolinium or samarium doped solid solutions of ceria for example.<sup>48,49</sup> Albeit, it is influenced by the surrounding gas atmosphere via extrinsic ceria reduction equilibrium already introduced in section 2.1.2 equation (11). Hydroxyl defect formation consumes oxygen vacancies (see chemisorption type 1 in figure 2.18) shifting the cerium reduction equilibrium equation (11) to the product site, producing a larger amount of electrons ( $Ce'_{Ce}$ ). Additionally Jimenez et al. state that water incorporation can also break the associates of oxygen vacancies and electrons (small polarons), increasing the amount of electrons contributing to the conductivity. Thus, in humid atmosphere protons and localized electrons are the majority charge carriers. The latter are higher in concentration and mobility, preventing the observation of a dominant proton conductivity at elevated temperatures in the study of Jimenez et al..

The work of Jimenez mainly focuses on a water partial pressure regime, where chemisorption is most probably the transport process, influencing the conductivity of the samples. They investigated nominally undoped ceria pellets. In contrast to that Chueh as well as Haile and coworkers investigated the impact of hydration on the transport properties of micro-crystalline 15 mol% samaria doped ceria at higher water partial pressures.<sup>49</sup> For this purpose they prepared pressed powder pellets of the material with a density of  $\approx 95\%$  by a classic solid state reaction route. Impedance spectroscopy measurements in the temperature range of  $650 - 250^\circ C$  under  $H_2O$  saturated and  $D_2O$  saturated conditions were conducted under oxidizing and reducing conditions. By separating bulk from grain boundary contribution,

Chueh et al. were able to observe that under oxidizing conditions humidification caused a substantial increase in the grain boundary resistivity while the bulk impedance remained unchanged. The results under H<sub>2</sub>O and D<sub>2</sub>O hydration were identical in the temperature regime between 450 – 250 °C. The transport process involved showed a higher activation energy under humidified conditions. With decreasing temperature the impact of hydration became larger, as well as with increasing humidity.

In contrast to the conductivity enhancement often reported for oxides under humidified conditions, like Jimenez reported as well (discussed above), Chueh et al. report a decrease in conductivity for Sm doped ceria and explain this effect with the motion of hydroxylic or protonic species being the reason for the enhancement of the surface and grain boundaries conductivity. They argue with an combined brick layer and space-charge model, where the space-charge layer thickness decreases with the samaria concentration. From the mean grain size and the capacity ratio between grain interior and grain boundary, the space charge width was determined to be 0.8 – 1.2 nm under dry conditions at 250 °C. This is approximately two times the lattice constant of doped ceria. Chueh et al. assume the grain boundary core to be ion-reversible, as the grain boundary resistance increase upon humidification is a property not expected for transport limited by the core itself. This assumption was also made by Avila-Paredes et al., when they studied gadolinium doped ceria.<sup>52</sup>

With this assumption Chueh and coworkers calculated the increase of the space-charge potential to be 5 – 6 mV in the investigated temperature range. This increase in  $\Phi$  leads to a change in  $[V_O^{\bullet\bullet}]$  upon humidification. Depending on the boundary conditions chosen, the space-charge potential change varies around 0.5%, leading to a 4% difference in the oxygen vacancy concentration, that decreases by about 24 – 28% upon hydration. The magnitude of the space-charge potential increase depends on whether there is a proton uptake from the bulk or not. In case of bulk proton uptake one would assume a depletion of protons in the SCL, while the oxygen vacancy depletion would still be more significant.

A positive  $\Delta\Phi$  implies that the positive charge transported by cations in the grain boundary core is larger than that transported by anions. This effect can be described when anion sites in the core, that should be occupied by oxide ions, are occupied by hydroxyl groups instead, which are less negatively charged than oxide ions. The situation in microcrystalline doped ceria is different than that described in literature for nanocrystalline materials where proton transport via the grain boundary core in direction parallel to the current is reported to become dominant at low temperatures.<sup>45,48,58,114,115</sup>

So far, only studies on pressed powders were discussed. In order to have a better control of the porosity, researchers started to investigate thin films as model systems. A remarkable work on thin films is the study by Oh and coworkers from the research group of S. Haile.<sup>38</sup>

They prepared two nominally undoped ceria thin films by MOCVD methods and investigated the resistivity of their nanocrystalline columnar thin films, while varying the water partial pressure and the temperature systematically. This work is one of the rare works that used nanocrystalline columnar thin films with well known morphology, rather than using pressed pellets, whose density varies due to particle size, morphology and preparation technique. The 5.6  $\mu\text{m}$  thick thin films prepared showed a 30 % porosity (see figure 2.11a)). The conductivity measurements were done by EIS in a macroscopic two point electrode setup. The conductivity was thus measured through the thin film and the substrate, parallel to the columnar crystallites the film consisted of. The humidity was controlled by saturating high purity oxygen with water held at a specific temperature. The measurements were carried out by first heating the samples to 500 °C at first. After the impedance spectra were stabilized, the temperature was lowered with a ramp rate  $\leq 2^\circ\text{C}/\text{min}$  between dwells of  $\geq 30$  min. Under these measurement conditions Oh and coworkers found that increasing the humidity introduces a medium frequency arc for a small  $p(\text{H}_2\text{O})$  window only, that could not be fitted by means of standard equivalent circuit routines. Thus, they evaluated the impedance of the high frequency semicircle that they interpreted as a mixed response of the grains and the bulk. For polycrystalline, macroscopic samples, one often finds two distinct semicircles, one at high frequencies representing the bulk response, and one at slightly lower frequencies representing the grain boundaries. This does not hold necessarily for nanocrystalline thin films, as the space charge zones could overlap like already mentioned in section 2.2.<sup>95,96,102</sup> As the two contributions could not be separated, Oh et al. analyzed the resistance associated with the thin film response (bulk and grain boundaries). They found a increase of the conductivity with increasing water partial pressure in the temperature regime between 400 – 200 °C. This is the opposite of what Chueh et al. reported.<sup>49</sup> Oh et al. interpreted the resistive element to correspond to proton migration along the surface of the parallel grain boundaries and/or open surfaces. Plotting the resistivity against the water partial pressure in the atmosphere around the sample (see figure 2.11 b) ) shows a slope close to  $-\frac{3}{4}$  in the double-logarithmic form. Oh et al. conclude, that according to equation (36), describing the proton incorporation reaction, one would expect a power law factor of  $-\frac{1}{2}$ . This factor was reported for proton conducting Gd-doped ceria at 200 °C by Ruiz-Trejo and coworkers before.<sup>48</sup> Their studies were - like most of the work in literature - conducted on macroscopic pellets, with a less specific morphology, but a density of about 90 %. However, Oh et al. found a deviation from this power law and argue that the main reason is the low oxygen vacancy concentration in nominally pure ceria, leading to site saturation effects, which are not further discussed in their paper. Furthermore, they state that the characteristics found in the resistivity data should reflect the adsorption isotherm of nanocolumnar ceria. A state-

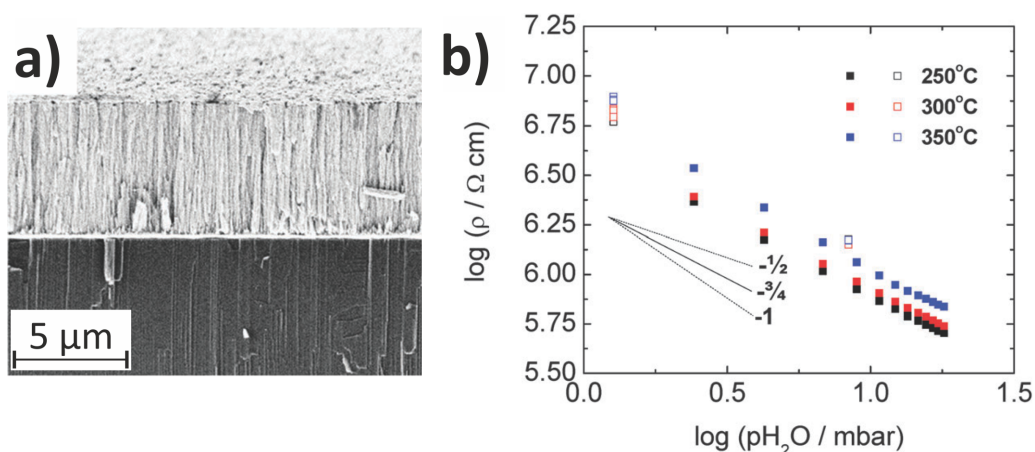


**Figure 2.11:** a) SEM cross section image of the nanocrystalline columnar thin film prepared by Oh and coworkers.<sup>38</sup> The film thickness is  $\approx 5.6 \mu\text{m}$ . b) Resistivity of a nominally undoped nanocrystalline ceria thin film at different temperatures as a function of the water partial pressure. The slopes of the doubly logarithmic graphs are close to  $-\frac{3}{4}$ . Both images are taken from the paper discussed in this paragraph.<sup>38</sup> Reproduced from Ref.<sup>38</sup> with permission from the PCCP Owner Societies.

ment that is addressed later in this thesis, as simulations of conductance data at various water partial pressures based on adsorption isotherms and percolation theory for the temperature regime  $T \lesssim 150^\circ\text{C}$  are part of the data interpretation. Oh et al. conclude that their results show proton transport occurring along the exposed grain surfaces and parallel grain boundaries, as no impedance due to grain boundaries normal to the direction of transport is observed.<sup>38</sup>

A further study on thin films was conducted by Gregori et al..<sup>46</sup> They studied epitaxial as well as dense and porous nanocrystalline thin films of ceria and 10 mol-% Gd-doped  $\text{CeO}_2$ , in order to evaluate the influence of residual pore volume on the conductivity enhancement due to proton conductivity. This is one of the rare works in this field, using thin films with controlled porosity as a model system. The films exhibit a thickness in the range of 200 – 400 nm. Their porosity was controlled by the preparation technique. Epitaxial and nanocrystalline dense films were prepared by PLD, whereas non dense nanocrystalline films were prepared by spin coating. The crystallite size of the spin coated film, was in the same range of the lateral crystallite size of the columnar grown PLD films. The films were contacted with parallel platinum electrodes and measured under dry (using a cold trap) and wet ( $p(\text{H}_2\text{O}) = 20 \text{ mbar}$ ) conditions. This study is one of the rare studies, that presents data on the conductivity of all thin film types over a large temperature range from 500 – 30 °C. For the higher temperature region above 100 °C Gregori et al. do not observe a significant difference between the nanocrystalline and epitaxial GDC thin films. Though quite remark-

able there is a slight decrease in conductivity of the pure CeO<sub>2</sub> samples (nanocrystalline and epitaxial) under dry conditions compared to wet conditions, which is not discussed further within the paper. In the low temperature region ( $T < 50\text{ }^{\circ}\text{C}$  under wet conditions the conductivities increase drastically for the epitaxial and the nanocrystalline dense samples. Gregori et al. attribute this conductivity enhancement to condensation of water on the top surface. For the porous samples the behavior in dry atmosphere is very similar to that of the other films under investigation. However, there is a significant conductivity enhancement, already at temperatures  $T < 300\text{ }^{\circ}\text{C}$ , in wet atmosphere. The conductivity difference between wet and dry conditions becomes more pronounced at lower temperatures as shown in figure 2.12. This findings confirm previous studies on the proton conductivity in nanocrystalline nominally pure and 6 mol% Gd doped ceria (GDC) by Shirpour and coworkers.<sup>58</sup> Shirpour and Gregori both conducted their research in the group of Joachim Maier in Stuttgart. Gregori et al. discuss in detail whether the proton conduction along the open pore walls is due to proton injection of protons into the material in the space charge zone below the surface, or whether conduction occurs predominantly within the water layer adsorbed on the surface of the pores. They conclude that proton conduction within the water layer adsorbed on the walls of the open porosity is absolutely plausible. This conclusion was made from an estimation of reasonable proton mobilities based on the brick layer model for percolating porosity using the following equation.<sup>18</sup>

$$\sigma_m = \frac{4a}{d} \varphi_P \sigma_{\infty,L} \quad (37)$$

Here  $a$  is the thickness of the adsorbed water layer,  $d$  is the average pore size,  $\sigma_{\infty,L}$  is the bulk proton conductivity and  $\varphi_P$  is the open porosity volume fraction ranging from 0.05 – 0.3. Thus, regarding to this work, the residual open porosity of the thin film sample is the key factor for the protonic conductivity, rather than the large grain boundaries density, as a dense nanocrystalline thin film does not show a conductivity enhancement below  $300\text{ }^{\circ}\text{C}$ . It remains unresolved whether the conduction occurs in the water layer on the surface or within the solid oxide space charge zone right at the interface between water and ceria.

In contrast to Chueh and coworkers who investigated microcrystalline material, Avila-Paredes et al. investigated nanocrystalline ceramics of GDC with an average grain size of 15 nm.<sup>52</sup> Their main focus was the temperature regime between  $400 - 30\text{ }^{\circ}\text{C}$ , in which they investigated the conductivity as a function of the dopant concentration. This temperature range seems reasonable in order to detect all effects probably caused by adsorbed water. They prepared nanocrystalline ceria pellets doped with 0.5, 10 and 20 mol% gadolinium and measured the bulk resistance by EIS under dry and wet conditions. Their results are shown in figure 2.13.

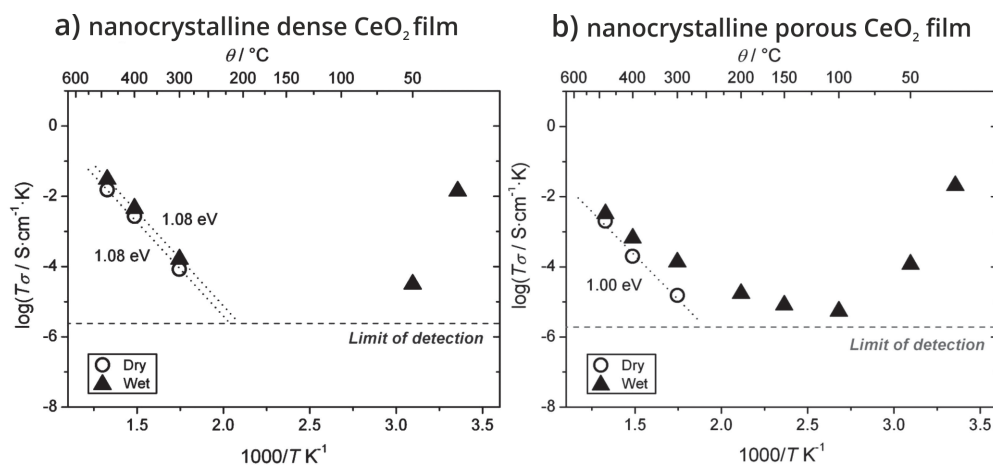


**Figure 2.12:** Main result (and graph) taken from the study by Gregory et al. reprinted with permission from John Wiley and Sons.<sup>46</sup> The conductivity of a porous  $\text{CeO}_2$  film under wet conditions b) starts increasing at  $T < 300^\circ\text{C}$  already, while a dense film a) only shows conductivity enhancement at  $T < 50^\circ\text{C}$ .

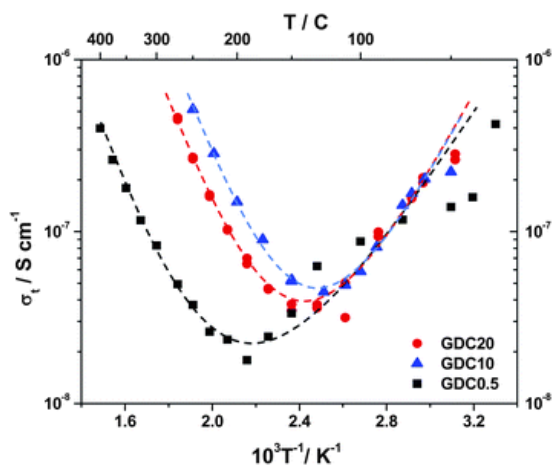


**Figure 2.13:** Main results of the work by Avila-Paredes and coworkers reprinted with permission from the Royal Society of Chemistry.<sup>52</sup> The total conductivity of GDC is dominated by the dopant concentration above  $200^\circ\text{C}$ . Below  $200^\circ\text{C}$  proton conductivity becomes dominant, without being a function of dopant concentration or grain size.

They found that the conductivity above 200 °C is clearly dependent on the Gd dopant concentration, as the total conductivity of the sample at these high temperatures is mostly dominated by the oxygen vacancy concentration and not by adsorbed water. At temperatures below 200 °C the total conductivity becomes dominated by the proton partial conductivity. The conductivity for low temperatures under wet conditions is the same for any composition. This stresses the fact that both the proton concentration and their mobility are not influenced by the dopant concentration. Thus, the bulk defect chemistry described by equation (36) is irrelevant for grain boundaries or interfaces, as there is no connection detectable between dopant concentration in the bulk phase and the proton concentration in the grain boundaries. This statement somewhat contradicts the idea of a space-charge layer in which the charge carrier concentrations are determined mainly by the space charge.

Avila-Paredes carried out the same experiment with nanocrystalline 8 mol-% yttria stabilized zirconia with crystallite sizes between 13 – 100 nm and found a non-linear dependence of the conductivity at temperatures below 150 °C on the mean grain size  $d$  of their powder samples:<sup>53</sup>

$$\sigma \propto d^{-n} \text{ with } n \approx 3 \quad (38)$$

Avila-Paredes state that if the brick-layer is a good approximation for microcrystalline structures the grain boundary conductivity should increase by one to two orders of magnitude if the grain size decreases from 100 – 10 nm. An effect that cannot be explained by the grain boundary density only. Avila-Paredes and coworkers therefore suggest changes in the defect distribution, leading to a charged grain boundary core, with an corresponding SCL to be responsible for the non linear behavior.

Interestingly these works are cited by Chueh et al.<sup>49</sup> in order to back up their theory of an ion-reversible grain boundary core as the reason for the grain boundary resistance increase upon humidification at elevated temperatures. A statement that is vague as Avila-Paredes and coworkers argue for a different temperature range.

From the context of operating SOFC's at temperatures below the usual 800 – 1000 °C in order to overcome technical obstacles and degradation problems Sangtae Kim and Manfred Martin together with their coworkers searched for alternatives to be operated at lower temperatures.<sup>45</sup> They build a water concentration cell using yttrium stabilized zirconia (YSZ) as a proton conducting electrolyte operating at room temperature. For that purpose they pressed nanostructured YSZ and SDC (20 mol-% samarium) dense pellets and measured the electromotive force (emf) when one side of the cell was exposed to dry air, while the other side was exposed to moist air or even dipped into liquid water. They measured emf values of up to 200 mV across the electrolyte and steady state currents of 30 nA. Reducing the grain

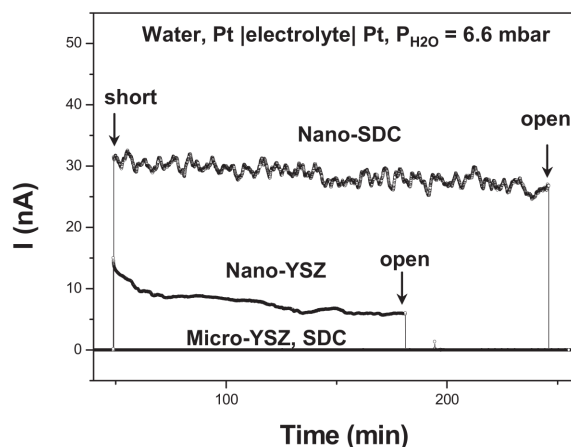


**Figure 2.14:** Short circuit currents measured in water concentration cells with nano- and microstructured 20 mol % SDC and 8 mol % YSZ at room temperature by Kim and coworkers. A Nano-SDC concentration cell delivers a remarkable current of 30 nA. Figure taken from the publication of Kim et al. reprinted with permission from John Wiley and Sons.<sup>45</sup>

size in the pellets by sintering the starting material, the emf measured in a concentration cell was the same, than for nanocrystalline material, but the currents measured on a short-circuited cell were smaller than 10 pA. Whether this decrease was only due to a change in the geometric scaling factor or due to a change in the nature of the grain boundary region was not elucidated by Kim et al.. For further proof that SDC and YSZ actually conducted protons, secondary ion mass spectrometry measurements were conducted on samples exposed to  $D_2O$  saturated air. A summary of these findings is shown in figure 2.14 taken from the respective paper.<sup>45</sup> The power output of the concentration cells is qualitatively similar to those of classical SOFC's but unfortunately the power densities in those cells are low.

Takamura and Takahashi describe the water adsorption behavior and electrical conductivity of 6 mol-% SDC nanoparticles.<sup>115</sup> They used volumetric water vapor adsorption at room temperature as well as thermogravimetry analysis (TGA) to study the adsorption behavior of nanoparticles powder samples with crystallite sizes below 50 nm. They compared a sample prepared by homogeneous precipitation using hexamethylenetetramine (HMTA) with a sample prepared by UV laser irradiation of a cerium and samarium nitride solution. For the HMTA sample they found a large amount of water adsorption reaching up to 3 mass – % at very low water pressures of only 368 Pa that most probably are often referred to as dry conditions in other works. Under the same conditions the UV sample only showed 0.12 mass – % water adsorption. From BET measurements Takamura and Takahashi conclude that this is mostly due to secondary particle size differences of the powders. A noteworthy observation in this study is, that the electrical conductivity of both samples, HMTA and UV, which show

a limited amount of water adsorption without capillary condensation, are in the same range. From this Takamura and Takahashi conclude that “neither condensed water in cavities nor excessively water is responsible for proton conduction”.<sup>115</sup> They assume that adsorbed water in the vicinity of oxide surfaces and/or protons incorporated into grains or grain boundaries of Sm-doped ceria are the origin of the conductivity enhancement in nanoparticles at low temperatures. Further direct evidence for this thesis is not given in that work. Whether the water layer in this case is chemisorbed or physisorbed is also not discussed. The results however seem to be a mixture of both, as physisorption will play a significant role at higher water partial pressures especially for the HMTA samples, while a chemisorbed water layer would explain the observation of conductivity enhancement of the UV samples at relatively dry conditions.

Raz et al. investigated the chemisorption and physisorption of water on YSZ powders by conductivity and TGA measurements in the whole temperature range between 35 – 800 °C.<sup>116</sup> Comparing the results of conductivity measurements in humid atmosphere with TG measurements, Raz et al. were able to determine the enthalpies of defect formation and migration of water on YSZ.

As the conductivity of dry compacted powder was significantly lower than that of humid powder, they excluded oxygen conduction as the responsible conduction mechanism. By measuring the open-circuit voltage of a concentration cell, with YSZ as an electrolyte exposed to two humid gases with different oxygen partial pressures, Raz et al. showed that the conduction was ionic, as the transference number was equal to unity.

By measuring the conductivity of samples in humidified conditions over a large temperature regime from 35 – 800 °C Raz et al. found that conduction by proton hopping in a chemisorbed layer becomes detectable between 150 and 450 °C. The Arrhenius plot measured by Raz and coworkers is shown in figure 2.15

Using the Langmuir isotherm as an estimate as well as TGA, the coverage of the surface by a chemisorbed layer was assumed to be larger than 50% for the compacted powder surface with crystallite sizes of 600 nm. From an Arrhenius plot of the conductivity the sum of the proton migration enthalpy and the defect formation enthalpy ( $\Delta H_{\text{mig}} + 1/2\Delta H_{\text{form.}}$ ) was calculated from the slope to be 0.3eV. As the formation enthalpy was reported by Blesa et al. to be  $\Delta H_{\text{form.}} = 0.23 \text{ eV}$ <sup>117</sup>, the migration enthalpy was calculated as  $\Delta H_{\text{mig}} = 0.19 \text{ eV}$ . For temperatures of about 100 °C Raz et al. state that the conduction in a single physisorbed layer becomes dominant. At 150 °C the curve in figure 2.15 flattens out, showing a slight decrease in resistance cooling down from 40 – 80 °C. In a physisorbed layer the coverage between 40 °C and 80 °C is not constant and not complete either. Thus, two contradicting processes need to be considered. On the one hand, a decrease in temperature increases

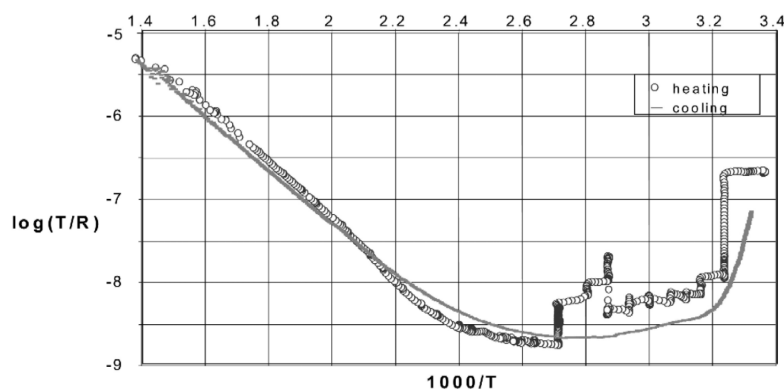


**Figure 2.15:** Original Arrhenius plot reprinted from the work of Raz et al. with permission from Elsevier.<sup>116</sup> T is the temperature and R the resistance of the YSZ powder sample under investigation.

the coverage. On the other hand, the mobility of hydronium ions decreases with decreasing temperature.

When the coverage of the first physisorbed layer is completed, the next water layer starts to become significant. In BET- theory, as well as in the publication by Raz et al. it is assumed that this water layer is bound by a single hydrogen bond to the first physisorbed layer. Further layers are coordinated similarly by single hydrogen bonds as in liquid water, and a three-dimensional water layer is formed. The enthalpy of adsorption of the second and further layers is slightly lower than that of the first layers adsorbed between 40 – 80 °C. The multiplayer adsorption on YSZ becomes visible in the conductivity measurements below 40 °C, when the resistance decreases drastically, due to an increase in the thickness of the conducting water phase. Raz et al. expect this change to happen, when most of the first physisorbed layer is completed. They conclude that proton conduction takes place in the physisorbed water layer, which becomes thicker with decreasing temperature, facilitating the ionic conduction by protons. As a side note Raz et al. state, that the increase in conductivity for  $T < 40$  °C could also be due to impurity ions on the surface, solved in the thicker water layer.

Ding et al. have studied the influence of water at low and elevated temperatures on nanostructured ceria by time-resolved Kelvin probe force microscopy tr-KPFM, measuring the surface potential of nanostructured ceria in the space and time domain. The fundamental mechanisms of proton injection and transport were investigated as a function of atmospheric conditions and the presence of a three phase boundary.<sup>42,118</sup> Within this study nanostructured ceria thin films with a thickness of less than 100 nm were prepared by chemical solution deposition and contacted by Pt- electrodes, created by sputtering. With these techniques Ding and his coworkers created an exposed and a covered electrode allowing the separation

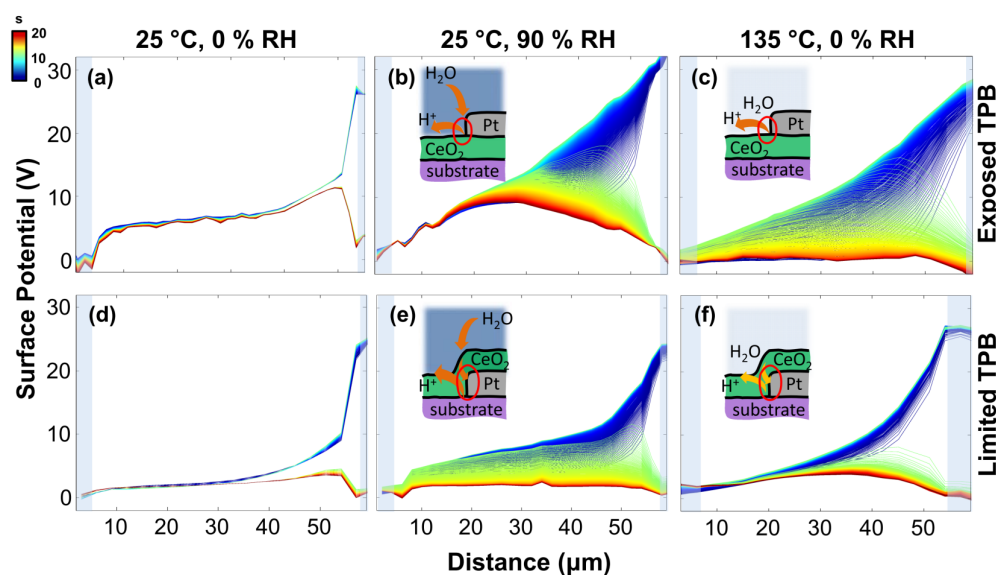


**Figure 2.16:** Temperature and RH dependence of surface potential versus time and position measured for exposed-TPB from the work of Ding et al.<sup>42</sup> Reprinted with permission from Elsevier.

of the two transport processes, responsible for the low-temperature proton conductivity of ceria.<sup>43</sup> tr-KPFM is a scanning probe microscopy technique that detects the surface potential with submicron spatial resolution over a period of time with a time resolution in the millisecond regime.<sup>119</sup> A bias of 30 V applied between working electrode and counter electrode may initiate electrochemical processes and charge carrier migration in response to the electric field, causing variations in the surface potential profile. When the bias is switched off after 10 s, charges start to redistribute on the ceria surface, changing the local surface potential. Increasing humidity and temperature changes this behavior. Figure 2.16 shows the main results of the polarization experiments. The initial surface potential does not undergo changes over time (figure 2.16 a) and d)) under dry conditions at 25 °C. Also there was no inter-electrode current detected under these conditions. This indicates a limited electrochemical activity and charge transport. At 90 rh% strong polarization and relaxation processes are observed (figure 2.16 b) and e)), indicating the generation of protons or additional conduction pathways. At elevated temperatures of 135 °C and nominally dry conditions (with residual water in the atmosphere) the sample with an open electrode setup still shows a surface potential affected by temperature (figure 2.16 c)). For the covered electrode at elevated temperature (figure 2.16 f)), the surface potential variation is limited. Ding et al. conclude that at elevated temperatures and high relative humidity a water splitting reaction takes place at the exposed three phase boundary. In order to explain the high activity monitored for the protected electrode setup, they argue that water and oxygen

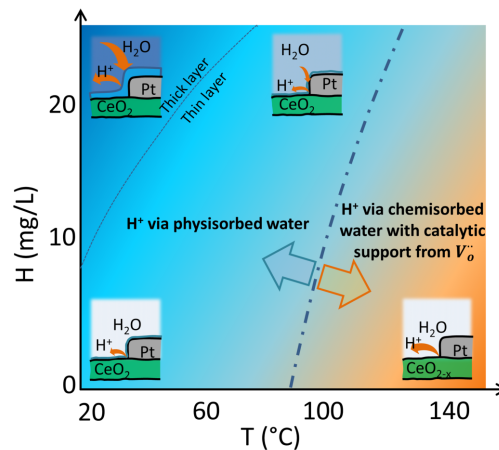
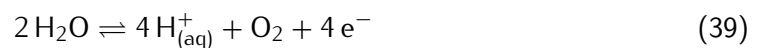


**Figure 2.17:** Schematic representation of the extent of the different environmental regimes for activation of the different mechanisms contributing to proton conductivity in or on nanostructured ceria thin films. Taken from the work of Ding et al.<sup>42</sup> Reprinted with permission from Elsevier.

could permeate the ceria film towards the electrode, resulting in a electrochemical activity. Under dry conditions at elevated temperatures the physisorbed water layer starts desorbing from the ceria surface, resulting in a decrease of transport pathways for the protons. Under dry conditions at elevated temperatures this diffusion-limiting process results in an activity breakdown on the buried electrodes in comparison to the activity under humidified conditions at the same temperature.

From their findings Ding et al. conclude that they can identify two environmental regimes for proton injection and transport in nanostructured ceria thin films (see figure 2.17). The first regime is found for temperatures below 100 °C, where proton generation and conduction occurs through a physisorbed water layer on the ceria surface even in what they state to be dry conditions, under which small amounts of water molecules are still present in the atmosphere and on the sample surface. The proton generation reaction at the anode is given by



This electrochemical process is triggered by the high polarization potential of 30 V used in this work. At temperatures above 30 – 60 °C the physisorbed layer under dry conditions gets so thin, that the proton generation and transport rates limit the overall conduction. In the second regime for temperatures between 100 °C ≤ T ≤ 135 °C more protons are generated and conducted through the chemisorbed water layer by a Grotthuss like hopping mechanism

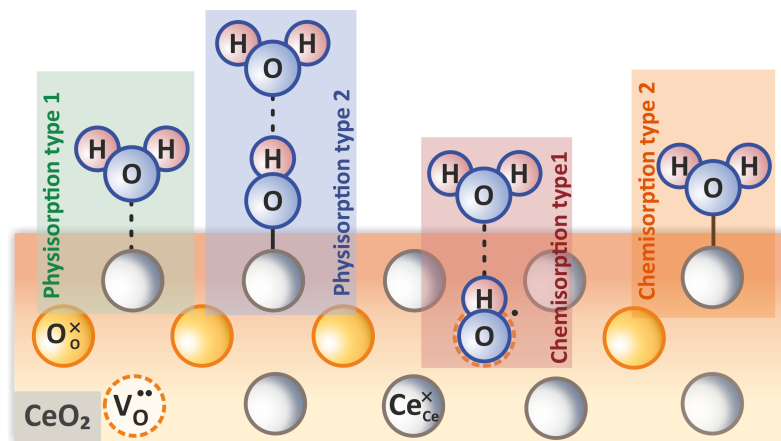


**Figure 2.18:** Possible configurations of first layer adsorbed water species at the surface summarizing the various species mentioned in literature.

Raz et al. already proposed for proton conductivity in YSZ samples (see next paragraph).<sup>116</sup>



In equation (40)  $(\text{Ce}_{\text{Ce}}^{\text{x}} - \text{OH}_2)$  symbolizes a water molecule physisorbed on the ceria lattice and  $(\text{Ce}_{\text{Ce}}^{\text{x}} - \text{OH}_3^{\bullet})$  indicates physisorbed water with an excess proton ( $\text{H}^+$ ). Furthermore, Ding et al. found evidence that the proton generation might be catalytically supported by oxygen vacancies. The literature overview given above shows that there is still an ongoing debate on the effects of humidity on the conductivity of ceria based materials. Examples can be found where humidity has a decreasing effect (Jimenez et al.<sup>57</sup>) on the conductivity as well as a slightly increasing effect (Oh et al.<sup>38</sup>) even at relatively high temperatures between 250 – 350 °C. Other groups report that no effects at all are detected (Gregori et al.<sup>46</sup>). Further reports state that the history of the sample, especially residual water on the surface is important.<sup>42,57,118</sup> It becomes obvious that the literature basis is not detailed enough to derive the behavior of polycrystalline nanocolumnar zirconia doped ceria thin films under humidified conditions. Furthermore, the conductivity data in literature is not correlated quantitatively with adsorption theory in order to derive information on the adsorption process of water from conductivity measurements. This would be a great tool in order to improve applications in humidified atmospheres like ceramic oxide humidity sensors for example. In order to give a general overview on the different adsorption mechanisms proposed in literature they are drawn as a schematic in figure 2.18. It shall be noted that only the first water monolayer adsorption is shown in the drawing. Of course additional water layers are adsorbing on this first water layer at increasing water partial pressures by forming hydrogen bonds to the

first layer water molecules. In order to combine conductivity measurements and adsorption theory, it was found in this work that applying percolation theory combined with adsorption theory in order to simulate the conductivity data is a promising approach. The concept of percolation theory is therefore presented in the next section.

## 2.4 Percolation theory

At this point a small outlook to the results of the conductivity measurements under humidified conditions and low temperatures is necessary. In order to describe the results that are described in section section 4.3.3, applying a discrete percolation approach to describe the water partial pressure dependence of the conductivities measured at low temperatures, turned out to be a reasonable approach. Describing the conductivity without assuming a percolating network of water, forming on the surface was not possible by applying several adsorption isotherms only. Thus, in the following section the basic concepts of discrete percolation theory are explained to the reader, trying not to focus too much on the mathematical concepts and theorems, but describing the main aspects together with some examples from literature which are similar to the problem addressed in this work.

The following abstract is mainly based on the book by Dietrich Stauffer and Amnon Aharony, which is highly recommended as an introduction to percolation theory, covering basic theory and also specialized fields.<sup>120</sup> According to Stauffer and Aharony the history of percolation theory starts with the work of two chemists, Flory and Stockmayer, who during World War II described how macro-molecules (in polymers) form from small branched molecules.<sup>121,122</sup> In this example the monomer molecules are the so-called *sites* or *vertices*. These are positions in a *lattice*, that can have a certain property. For example, they could be occupied or unoccupied. The macro-molecules forming from these monomers during the so called gel forming process, are *clusters* in percolation theory. A *cluster* is a group of neighboring sites with the same properties. In the so called *site percolation model* sites that share an edge are defined as neighbors, sites that share a corner are next neighbors. Beneath the site percolation model there is also the *bond percolation model*, based on a regular point lattice in n-dimensions. It considers the lattice edges as relevant entities. Bond percolation is considered to be less general, which is why in this work only discrete site percolation will be considered.

Discrete percolation theory is dealing with the clusters that are formed on such a lattice. Percolation theory became successful and applicable to many problems due to the availability of computers for science in the 1960s.<sup>120,123</sup> Considering a huge lattice, consisting of  $N$

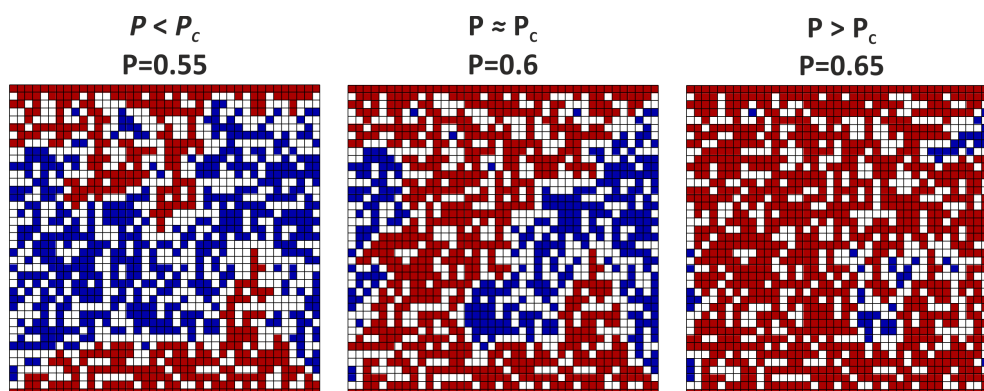


**Figure 2.19:** Simulation of a 2D lattice with 40×40 vertices, at different occupation probabilities. Blue sites (■) are occupied, white sites (□) are unoccupied. The red sites (■) are ones that can be reached from the top or bottom by going only on filled squares.<sup>124</sup>

vertices, it can be randomly occupied at a certain lattice point with the probability  $P$ .<sup>i)</sup> For a large lattice  $PN$  is the number of occupied squares, whereas  $(1 - P)N$  vertices are unoccupied.<sup>123</sup>

At a certain critical probability  $P_c$  the properties of the lattice change drastically. For example, when a closed path between two neighboring sides of the system is formed, this allows to reach the opposite side of the lattice only by moving along occupied vertices. Such a system can be simulated by available software tools.<sup>124</sup> figure 2.19 shows a simulation of a lattice with 40 by 40 vertices, at different occupation probabilities. For a probability of  $P \geq 0.6$  a cluster forms that spans from the top to the bottom layer. In this case the system is called percolating. Many phenomena of percolation occur in the vicinity of the probability  $P_c$ , at which a first percolating cluster is formed. These phenomena might be mathematical properties of a set of numbers, but it can also very well be connected to physicochemical properties of a system. From a physical point of view a system undergoes a phase transition at the critical probability  $P = P_c$ .<sup>120,123</sup> Per definition a phase transition is a discrete point at which the properties of a system change qualitatively, during a continuous variation of a certain parameter. Let us assume to apply a voltage between the top and the bottom layer in the example in figure 2.19. Lets further assume that every point in the system that is occupied becomes conductive, whereas an unoccupied lattice site is isolating, the resulting current flow between the top and bottom layer would change drastically in the vicinity of  $P = P_c$ , where a first shortcut is formed while  $P$  is increased from 0 to 1.

<sup>i)</sup>Often the symbol  $p$  is used for the probability in percolation literature. In order to avoid confusion with the partial pressure  $p$ , which is used in this work to describe a partial gas pressure, a capital “ $P$ ” is used for the probability in this text.

The exact solution for the probability  $P_C$  on a certain type of lattice is not trivial. For most lattice types there is no exactly defined threshold. In many cases  $P_C$  has to be numerically derived, or experimentally determined and then, extrapolated to an infinite system size.

Percolation theory does not only describe the properties of percolating systems, but also its behavior the vicinity of  $P_C$ . The physical properties of composites near percolation were for example reviewed by Nan et al. .<sup>125</sup> The significance of the percolation lies in the fact that transport properties like conductivity or diffusion coefficients exhibit a non linear scaling with the volume fraction of a minor phase mixed into a major phase with increasing volume fractions  $f$ .

$$\text{Properties} \propto |f - f_C|^{\pm m} . \quad (41)$$

The critical fraction  $f_C$ , at which the properties change depends on the shape of the fillers and the matrix for composite materials. For similar sized spherical shapes of filler and matrix  $f_C$  has a value of approximately 0.16, the so-called Sher-Zalen invariant. As this invariant only holds for micro- structural systems, other values for  $f_C$  varying between  $10^{-3}$  and 1 haven been reported in literature.

In case of mixing a minor component with a conductivity  $\sigma_1$  with an insulating matrix with a conductivity of  $\sigma_2$ , the total conductivity for a composite near percolation changes as follows. When  $f$  is smaller than  $f_C$  the isolating property of the matrix governs the total conductivity of the system  $\sigma_C$ .

$$\sigma_C \propto \sigma_2(f - f_C)^{-s} \text{ for } f < f_C \quad (42)$$

Typical values for  $s$  are in the range of  $s = 0.7 - 1.0$  for a three-dimensional system.

When  $f$  is just larger than  $f_C$ , the conductive component forms a conductive path throughout the matrix, as shown for the 2D case in figure 2.19 .  $\sigma_C$  is now determined by the conductivity of the filler following a non linear power law with an exponent  $m$ , which is typically in the range of  $m = 1.6 - 2.0$  for theoretically described 3D systems.

$$\sigma_C \propto \sigma_1(f - f_C)^m \text{ for } f \geq f_C \quad (43)$$

For continuum percolation in three dimensions (also referred to as the Swiss cheese model in literature) however, the percolation exponent is enhanced up to 2.38. For many experimentally investigated systems other scaling factors larger than 2 with values of up to 8.5 are reported.<sup>125-129</sup> Ahmad et al. studied the water sensing behavior of NiO/Al<sub>2</sub>O<sub>3</sub> nano composites in 2006.<sup>128</sup> They analyzed conductivity data of pressed pellets from powders, synthesized by sol-gel methods, at different relative humidities (RH) on a percolation theory based formalism.<sup>130</sup> By using impedance spectroscopy Ahmad and coworkers were able to

separate bulk, grain boundary and electrode response of the sample under test. Describing the conductivity change with the relative humidity they proposed the following relationship, correlating the relative coverage of the surface by water molecules  $\Theta$  to the systems conductivity:

$$\sigma \propto (\Theta - \Theta_C)^m \text{ with } m = 2.07 - 2.29 \quad (44)$$

$\Theta_C$  is the critical fractional coverage ranging from 0.7 to 0.25 in 2D or 3D systems respectively. Furthermore, they were able to show that increasing the NiO content leads to a decreasing resistance of the chemisorbed water layer. This is not further affected by increasing humidity, up to values that lead to physisorption of water on the chemisorbed layer, which provides a constant concentration of protons as mobile charge carriers in the physisorbed water layer.

---

## 3 Methods

In the following sections the target preparation and analysis methods are briefly described. The chapter is structured into three sub-chapters. The first sub-chapter describes the methods used to prepare and characterize the ceria based thin films, starting with the preparation of the targets used in the pulsed laser ablation process, by which the thin films investigated in this study were prepared. In the second chapter the methods used for the crystallographic and morphologic characterization of the thin films are described in detail. The last section describes the techniques and methods used for the electrochemical characterization of the thin films. For those measurements the thin films were contacted with interdigital electrodes produced by photolithography directly on top of the thin films.

### 3.1 Sample preparation

#### 3.1.1 Target preparation

In order to ablate thin films, a target is needed for the pulsed laser deposition (PLD) process. These targets were prepared from high purity starting powders mixed in stoichiometric compositions for 10CZO, 8CZO and 6CZO. Cer(IV)-oxide was commercially purchased from Sigma-Aldrich in 99.99% purity. Zr(IV)-oxide was commercially purchased in 99.95% purity with a mean particle size distribution of 5  $\mu\text{m}$ . The powders were mixed and dry ball milled in a planetary micro mill Pulverisette 7 from Fritsch, using zirconia grinding balls with 3 mm in diameter. The mixed starting powders were milled for 25 min in total, with 5 min of milling per cycle at 300 rpm and 5 min pause in between the 5 milling cycles, in order to prevent overheating of the mortar.

The resulting homogenized powder was pressed into pellets of about 1 cm thickness and 13 mm diameter in an uniaxial press, using a force of 30 kN. Afterwards the pre-pressed green body was isostatically pressed with a pressure of 3500 bar. The final green body was then sintered under laboratory atmosphere in a chamber furnace at 1500 °C. For 10CZO and 8CZO a heating and cooling rate of 5 °C/min was used. As the first 6CZO sintered bodies showed some cracks, that were most probably due to thermal stress, a reduced heating and

cooling rate of 2 °C/min was used for this composition.

XRD measurements were taken from the starting powder mix and the sintered pellets with an Panalytical powder diffraction instrument. The detailed experimental parameters chosen are explained in section 3.2.1.

Additionally SEM images of the surface were taken with a Zeiss Merlin high resolution SEM system, using acceleration voltages between 3 – 4 kV and sample currents of 90 – 120 pA at a working distance of about 4 mm.

Prior to the ablation of material from the sintered targets their surfaces were polished using a deburring wheel followed by fine sandpaper. This assured flat and plane-parallel faces of the target. Possible contaminants from this process were removed by ablation of some target material with the PLD laser, prior to ablation of the thin films.

### 3.1.2 Thin film pulsed laser deposition (PLD)

For the pulsed laser deposition a custom build PLD vacuum chamber was used with a target to substrate distance of 43 mm.<sup>i)</sup> The energy of the pulsed 248 nm KrF excimer laser beam was varied between 85 mJ and 125 mJ per pulse, measured behind the laser port before each ablation, in order to compensate for UV absorbing impurities on the laser port glass from previous ablation processes. For the majority of the samples discussed in this dissertation an energy of 86 mJ per pulse was used with a repetition rate of 2 – 10 Hz. Keeping the substrate too target distance, the laser energy and its repetition rate constant, the two parameters pressure and temperature were varied in order to archive different thin film morphologies. As Infortuna et al. showed in 2007, these are the two governing factors that control the morphology of the thin films, as predicted by the structural-zone model, originally developed for sputter-deposited films.<sup>131</sup> The interested reader is referred to an older, but still relevant review on the thin film growth models by Thornton.<sup>132</sup>

The variation of thin film thicknesses was achieved by a variation of the number of pulses. The growth rates for 6CZO thin films were 0.025 nm/pulse with a standard deviation of only 0.004 nm/pulse. Such a constant growth rate was not achieved for thin films with the composition of 10CZO and 8CZO. Here the growth rate was  $0.0535 \pm 0.025$  nm/pulse for 10CZO and  $0.064 \pm 0.024$  nm/pulse for 8CZO. This is twice as high as for 6CZO. The reasons for the higher ablation rate and standard deviation was not investigated in detail in this work. Most probably the morphology of the PLD targets is the reason. The roughness of the 10CZO and 8CZO target was higher, and the targets were more brittle than the 6CZO

---

<sup>i)</sup>For unambiguous identification: The internal name of the chamber within the work group was "Braunschweig".

target. Thus, polishing before ablation most probably lead to a smoother surface of the 6CZO target, absorbing the same laser energy on a smaller surface area, while more material was vaporized for the slightly rougher 10CZO and 8CZO target. As the roughness of the latter was higher, scattering in the resulting ablation rates and thus also in the deposition rate can be explained.

In order to grow films with different morphologies the substrate heater temperature was varied in the temperature range between 30 – 700 °C. The sample was heated under the desired oxygen gas background pressure of  $10^{-2}$  mbar. Once the desired temperature was reached the sample was allowed to get into thermal equilibrium before the ablation process was started. The standard laser frequency was 10 Hz. A series with variation of the repetition rate between 2 – 10 Hz for 8CZO films showed no significant influence on the thin film morphology or deposition rate.

After deposition the thin films were annealed at various temperatures for 48 h between 600 °C and 1100 °C in order to allow crystallite growth and relaxation of strain that might have been introduced during the PLD ablation process.

## 3.2 Crystallographic and morphologic characterization

### 3.2.1 X-ray diffraction (XRD)

X-ray diffraction analysis were carried out on a PANalytical Empyrean powder diffractometer, just like for the targets. Non-monochromatic X-rays were created by a copper anode operated at 40 kV and 40 mA, creating radiation with a  $\text{Cu-K}\alpha_1$  wavelength of 1.5406 Å and a  $\text{Cu-K}\alpha_2$  wavelength of 1.54443 Å. For the starting powders and sintered targets powder diffraction data were recorded in  $\theta - 2\theta$  geometry in a  $2\theta$ -range of 20 – 95°, using a 0.04 rad soller slit, an anti-scatter slit of 0.5°, a fixed divergence slit of 1°, and a irradiation length mask of 10 mm for the incident beam optics. Using a linear detector in scanning mode the step size was 0.017°/step and the integration time was set to 80 – 300 s, depending on the desired signal to noise ratio.

For the thin film samples two X-ray experiments were conducted for each thin film as follows. One experiment in Bragg-Brentano geometry ( $\theta - 2\theta$ ), the other in grazing incidence geometry ( $\omega - 2\theta$ ). For both measurements the  $1 \times 1 \text{ cm}^2$  samples were mounted in a special sample holder, assuring the correct height and a non-tilted position of the sample. For Bragg-Brentano measurements the  $2\theta$ -range was 20 – 95° and the beam optics were the same than for the target measurements. The step size was 0.026°/step, using an integration time of 300 s.

In addition grazing incidence measurements were conducted for some of the thin films using a parallelized beam with an incidence angle of  $\omega = 2^\circ$ . The anti-scatter slit was set to  $0.5^\circ$  and the divergence slit was fixed at  $0.125^\circ$ . Additionally in the diffracted beam optics a  $0.27^\circ$  parallel plate collimator was used, scanning a  $2\theta$ -range of  $25 - 85^\circ$  with a step size of  $0.1^\circ/\text{step}$ , integrating the signal for 20 s per step.

### 3.2.2 Morphological and chemical characterization

Like for the targets, scanning electron imaging analysis was carried out on a Zeiss Merlin equipped with a Gemini II column, operated at 3kV with probe currents between 30 – 90 pA and working distances of 3 – 4 mm, depending on the detector used. Typically the secondary electron detector was used, as its function of representation is optimized for representing the morphology of the surface giving topographic contrast. Additionally, the in-lens detector was used to check for edges on the sample surface, as this detector shows high contrast for out of plane objects. As the SEM system was equipped with an EDS detector, some thin films were also analyzed using this technique. Two different EDS systems were used. First an Oxford Instruments X-Max Silicon Drift Detector (SDD) with  $50 \text{ mm}^2$  detector size was used. In order to gain enough characteristic X-ray intensity the SEM electron beam was operated at 10 kV with a current of 300 pA. The EDS system was upgraded during the time of this study with an additional  $150 \text{ mm}^2$  SDD that was operated in parallel with the  $50 \text{ mm}^2$  detector, allowing the operation at lower acceleration voltages (7 kV) and currents (200 – 300 pA). This had the advantage that the sampling depth as well as the surface charging was reduced. Here one has to keep in mind, that the information depth for EDS can be roughly up to  $500 \mu\text{m}$  in  $\text{CeO}_2$  for the acceleration voltages used, which means that some of the characteristic X-rays measured will be generated in the substrate and not in the thin film<sup>133</sup>.

Thus XPS was used as a more surface sensitive technique to determine the thin film composition of the dense thin films. Photoelectrons typically escape the sample from a depth between 0 – 10 nm. Photoelectron signals generated in deeper layers of the sample, are attenuated exponentially, as the electrons have to travel through the sample to the detector. The XPS measurements were carried out with a PHI VersaProbe II (ULVAC-PHI) using an Al X-ray source producing monochromatic radiation of 1486.6 eV at 96.5 W with a beam diameter of about  $100.0 \mu\text{m}$ . In order to compensate surface charging a neutralizer filament was used for flooding the sample with low energy electrons operated at 3.0 V with 20.0  $\mu\text{A}$ . The samples were mounted electronically flooded on the sample holder with double sticky tape. Survey spectra were acquired using a pass energy of 187.85 eV, an energy resolution of 0.8 eV/step

and an integration time of 0.2 s/step. Detail spectra of specific energy regions of interest were acquired with a pass energy of 23.5 eV progressing with 0.2 eV/step using individually set integration times depending on the signal intensity ranging from 1.2 – 6.0 s/step.

### 3.3 Electrochemical characterization

#### 3.3.1 Photolithography

In order to measure the current response of the thin films on an applied alternating potential in parallel to the surface platinum interdigital electrodes had to be deposited on the surface. In order to prepare the small electrode structures necessary to achieve cell constants between  $10 - 100 \text{ cm}^{-1}$  a photolithographic process was developed for the application on ceria based thin films. The resists and solvents for developing, as well as the UV irradiation parameters (time and intensity) are optimized for silicon wafer based applications and provided by the distributor of those chemicals.<sup>134</sup> In case of the ceria based thin films prepared in this work feasible parameters were searched starting with previous works by Hartmann et al., who prepared interdigital electrodes on mesoporous ceria based thin films in the same laboratory, with chemicals from the same manufacturers as in the present study.<sup>4,90,135</sup> Nevertheless, during this process it turned out that the parameters for mesoporous thin films do not work well for dense thin films with lower surface roughness. This will be discussed later in this section. First of all the process used for most of the samples prepared in this study is described.

The photolithographic preparation work was carried out in the Micro- and Nanofabrication Laboratory (MiNa) in the Physics department of the University in Giessen under controlled clean room conditions. After deposition and characterization of the thin films they were transferred to the clean room facilities and cleaned with ethanol, acetone and isopropanol in an ultrasonic bath to remove any surface contamination. Afterwards the samples were heated on a hotplate at  $180^\circ\text{C}$  for 5 – 10 minutes, in order to remove any residual water on the surface. In the next step the samples were spin coated with  $90 \mu\text{L}$  of the negative resist ma-N 1420 from *micro resist technology GmbH* at 3000 rpm for 30 s in order to achieve the desired resist film thickness of approx.  $2 \mu\text{m}$ . The samples were pre-baked at  $100^\circ\text{C}$  for 120 s and radiated with UV radiation from a mercury-vapor lamp (HBO 350, Osram), covering the areas of the resist that were supposed to be removed during the development step with a photomask positioned with a photomask aligner (MA56, Karl Süss). The intensity of the Hg lamp was  $4.5 \text{ mWcm}^{-2}$  measured at 365 nm. The radiation time was set to 86 s. The resist was developed for 80 s in ma-D 533/ S development solution from *micro*

*resist technology GmbH* as well. The developing process was stopped by rinsing the sample with deionized water. Afterwards a hardbake of the samples was carried out ramping up from 50 °C to 100 °C in 15 min in order to reduce pattern reflow, followed by a temperature dwell for 30 min with the intention to stabilize the produced polymer structure by removing residual solvent from the resist.

On those structured samples a chromium adhesion layer of nominally 7 nm thickness was deposited via thermal vapor deposition. In this step it was assured that the thermal stress for the resist was as low as possible. Therefore, the sample temperature during chromium deposition was kept below 50 °C.

Platinum thin films were deposited either by magnetron sputtering or pulsed laser deposition. The Pt film and thus the electrode thickness was varied between 50 – 250 nm. For the PLD process the same chamber and laser was used as for the ablation of the ceria thin films. The pulse energy of the 248 nm KrF excimer laser was set to 350 – 400 mJ, depending on the beam energy measured behind the laser port of the chamber under ambient atmosphere, which was set to 125 mJ. At a sample temperature of 30 °C the Ar background pressure was set to  $10^{-2}$  mbar. 15000 – 30000 pulses were fired at the platinum target at 10 or 20 Hz repetition rate. Pt film thicknesses between 100 nm and 500 nm were ablated. The ablation rate increased when increasing the repetition rate. Although favorable for the Pt thin film stability, higher substrate temperatures during the ablation process were not feasible as the resist was not tolerant against elevated temperatures under vacuum conditions.

The alternative preparation by magnetron sputtering was conducted in the Physics department of the University of Giessen. Here a 200 nm thick platinum layer was deposited at a work pressure of  $6 \cdot 10^{-3}$  mbar, applying a sputtering power of initially 15 W for 2 min and 30 W for 14 min to the Pt sputter target.

After depositing the platinum layer the excess resist was removed with acetone (recommended by the resist manufacturer) assisted by an ultrasonic bath. Unfortunately, for most of the samples prepared via this route the platinum interdigital electrodes, that were supposed to stick to the thin film surface, were ripped off together with the resist and the platinum on it. This behavior was observed for almost all platinum films thicker than about 200 nm, although SEM images of the prepared resist structures showed that their undercut was sufficient to avoid a connection between the platinum on the resist and on the bare ceria surface. As a result it was decided to prepare thinner platinum electrodes. This unfortunately lead to problems during the electrochemical impedance spectroscopy experiments, as the thin platinum electrodes showed a high tendency to dewett on the ceria films with surface roughnesses in the nanometer regime, due to the temperatures of up to 550 °C applied. This dewetting behavior is also described in literature.<sup>136–138</sup> The thinner a platinum electrode, the higher

its tendency to dewett under the high temperatures applied in the EIS experiments. During the work of Raika Oppermann, who's specialization project and master thesis was carried out as sub-projects of the doctoral studies presented in this thesis, another photolithographic preparation route was developed using the positive resist ma-P 1215 from *micro resist technology GmbH*. The samples were cleaned and preheated at 180 °C to remove any residual contamination. Afterwards, the bonding agent hexamethyldisilazane (HDMS) was applied for a residence time of 30 s and then removed by 3000 rpm spinning, before the sample was spin coated with the positive resist at 3000 rpm for 30 s. The resist was then prebaked at 100 °C for 90 s. The sample was covered with a positive photomask and illuminated with the same Hg lamp than used for the negative resist. The illumination time was 16 s. The development agent ma-D 331 from *micro resist technology GmbH* was applied for 40 – 50 s, so that the radiated part of the resist was removed. Afterwards platinum was deposited by magnetron sputtering as described above. The liftoff was carried out under mild ultrasonification. This route using a positive resist ma-P 1215 in combination with sputter deposition of a platinum layer turned out to deliver the most reliable results during the liftoff step.

### 3.3.2 Electrochemical impedance spectroscopy under controlled atmosphere

The electrochemical impedance spectroscopy experiments were carried out in a temperature range between 30 – 550 °C under controlled atmosphere with oxygen partial pressures between  $10^{-6}$  – 1 bar as well as water partial pressures between  $10^{-5}$  –  $4.2 \cdot 10^{-3}$  bar. These water partial pressures correspond to a range of 0 – 100 % relative humidity in the gas feed of the gas tight oven, where the experiments were conducted in.

The ovens used during for the experiments conducted over a period of three years in this thesis varied in size and gas volume, but were all equipped with a similar set of sensors and gas feed technology. A schematic drawing of the most sophisticated, custom build measurement setup is shown in figure 3.1. The experimentally most suitable oven was the one with the smallest quartz tube volume. The tube was closed on one side (in the other ovens used, the tube was open on both ends), and the gas inlet was connected to an alumina capillary tube, that reached almost to the end of the tube in order to assure a quick gas atmosphere exchange controlled with mass flow controllers. The gases used in the feed were dry 5.0 O<sub>2</sub> as well as dry 5.0 Ar from compressed gas cylinders both supplied by Praxair. The desired gas mixture was roughly adjusted by the corresponding flow ratio with gas flow controllers. For humidified gas mixtures, the gas was humidified by directing it through an impinger in

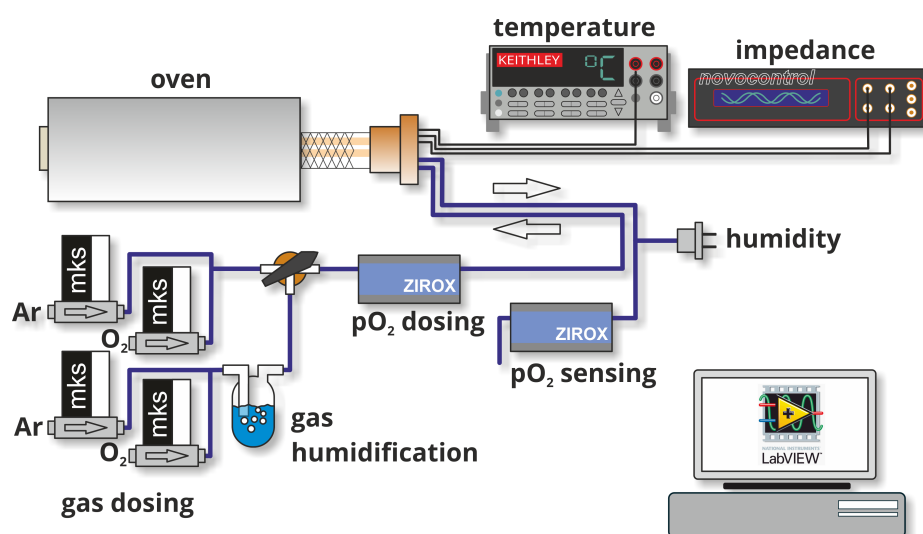


**Figure 3.1:** Scheme of the measurement setup. The sample was heated within the oven. A Pt/PtRh thermocouple was used to measure the sample temperature together with an Keithley multimeter. The Novocontrol Alpha AN frequency analyzer was used for the impedance measurements. The gas atmosphere was controlled using mks mass-flow controllers and ZIROX SGM5EL oxygen electrolysis devices, which were also used to determine the oxygen partial pressure in the ovens gas outlet. The humidity was measured using a HYT 939. The temperature and atmosphere control, as well as the data logging of all sensors and measurement equipment was done by a custom made LabVIEW program, except for the Novocontrol impedance analyzer, which was controlled by the suppliers software.

which deionized water was kept at a constant temperature of 21 °C ( $\pm 1$  °C). In order to measure the humidity of the gas atmosphere a humidity sensor was installed in the exhaust stream of the oven. This Hygrosens HYT 939 capacitive polymer based sensor is designed to measure the relative humidity in a range between 0 – 100 % ( $\pm 1.8$  %) at 23 °C with an reproducibility of  $\pm 0.2$  %.<sup>139,140</sup> Different water partial pressures were adjusted by mixing humidified and dry gas streams, using computer controlled mass flow controllers. From the relative humidity measured with the sensor the respective water partial pressure in the gas mixture entering the oven was calculated.

The mks mass-flow controllers were used to adjust the desired oxygen partial pressure roughly by mixing the respective amount of oxygen with argon as carrier gas, using a volume flow of 50 sccm in total. The precise adjustment was done with a zirconia based oxygen electrolysis device *SGM5EL* from ZIROX. It served for removal or dosing of oxygen into the carrier gas. To an electrolysis cell, consisting of a zirconia tube with porous platinum electrodes, a potentiometric cell voltage is applied, keeping the desired set point of a potentiometric measurement cell constant by using a PID control circuit. As the current of the electrolysis cell is proportional to the oxygen pumped through the zirconia into or out

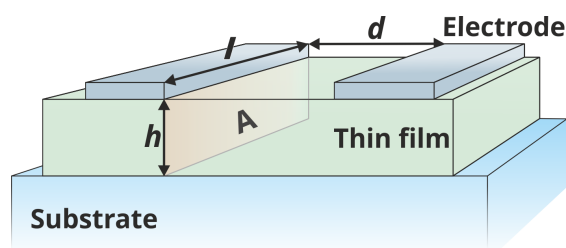


**Figure 3.2:** Scheme for the determination of the cell constant of an interdigital electrode on a thin film by equation (45). The ratio of the electrode distance  $d$  and the area  $A$  (orange) define the cell constant.  $A$  is a virtual electrode surface approximated by the finger length  $l$  times the film thickness  $h$ .

of the carrier gas, the oxygen partial pressure could be precisely set. Additionally, it was also possible to use the devices measurement cell only for monitoring the oxygen partial pressure within an relative error of  $< 5\%$  in the exhaust stream of the oven as well.<sup>141</sup> It was observed that there was no significant difference in oxygen partial pressure at the inlet and outlet of the oven, even for oxygen partial pressures as low as  $10^{-20}$  bar, proving that the whole system was gas tight, as any leakage would have been detected that way.

The quartz glass tube, containing the sample and its connecting platinum wires, was mounted in a computer controlled tube furnace, in order to automatically adjust the oven/ sample temperature, which was measured by a thermocouple in the direct vicinity of the sample under test.

Within this tube the sample was contacted with  $100\ \mu\text{m}$  thick platinum wires, that were mechanically fixed on the sample with an alumina based ceramic paste (Ceramabond 503 or 668).<sup>142</sup> The electrical contact to the microelectrode was established by applying platinum paste (Heraeus) to the wire and the contact pad, prepared together with the interdigital electrode. The other end of the thin platinum wire was point welded to a thicker platinum wire, that was connected to the impedance analyzer. Figure 3.3 shows an image of the contacted sample with its structured electrode.

Each electrode had 20 fingers of  $3\ \text{mm}$  length with a width of  $40\ \mu\text{m}$  and a gap of  $40\ \mu\text{m}$  in between the fingers. Thus, the overall active electrode length  $l$  was derived from the number of intact electrode finger pairs (intact finger on both sides of the electrode) times their length. For a fully intact interdigital electrode a total electrode length  $l$  of  $0.6\ \text{m}$  was determined. This length times the film thickness  $h$  gives a reasonable first order approximation for the electrode area  $A$ , needed to derive the cell constant (see figure 4.14). Here one assumes that the entire film beneath the electrode is active. Together with the distance between the electrode fingers  $d$ , the cell constant  $Z$  for each sample could be determined

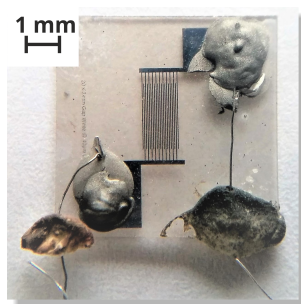


**Figure 3.3:** Photograph of a contacted ceria thin film as prepared for the electrochemical impedance spectroscopy. The photograph shows the substrate of  $1 \times 1 \text{ cm}^2$  covered with a 8CZO thin film, contacted by a platinum interdigital electrode. Each finger of the electrode is 3 mm long and  $40 \mu\text{m}$  in width. In addition one can see the platinum wire that is used to establish the contact to the impedance analyzer, together with the platinum paste drops to ensure good electric contact and the ceramic paste drops ensuring mechanic stability.

individually by

$$Z = d/A = \frac{d}{h \cdot l}. \quad (45)$$

The resulting cell constants in this work were in the range of  $19 - 158 \text{ cm}^{-1}$ , depending on the number of intact fingers after the lift off process and the thin film thickness.

In order to characterize the samples with electrochemical impedance spectroscopy, typically a controlled atmosphere regarding oxygen and water partial pressure was adjusted while heating up the oven and sample to  $550^\circ\text{C}$ . After an equilibration time of about 4 h, at the end of which the impedance data did not change significantly anymore the temperature was lowered by  $3^\circ\text{C}/\text{min}$  in  $25^\circ\text{C}$  steps. After the next temperature level was reached, a temperature dwell was set for 3 h, before the ramp down to the next lower temperature level was started. At  $300^\circ\text{C}$  typically the temperature steps were increased to  $50^\circ\text{C}$  per step, as here for most of the samples and atmosphere conditions the impedance was so large, that no reliable data could be measured. For temperatures around  $150^\circ\text{C}$  and lower, the step size was decreased again to  $25^\circ\text{C}$  per step, as here the impedance was smaller again for elevated humidities. It should be noted, that the dwell time was optimized regarding time efficiency from experiment to experiment. For higher temperatures the impedance data often stabilized after a short time already whereas this took longer at lower temperatures. Taking this into account the dwell times for the different temperature steps were set individually, in order to get reproducible data in a time efficient way. Without this a single impedance measurement for one atmospheric condition and the whole temperature range easily took about five days. Optimizing the dwell times, it was possible to reduce this to about 26 h, including the heating and atmosphere exchange and equilibration between two experiments.

All AC conductivity impedance measurements were carried out with a 2-electrode-4-wire setup connecting the sample to a Novocontrol alpha-A impedance analyzer, equipped with a ZG4 interface. In order to minimize the effect of leakage currents the Faraday cage was kept at the potential of the high impedance terminal, by connecting it to the driven shield of the ZG4 interface. The impedance spectra were recorded within a frequency range of 10 mHz to 1 MHz with an oscillation voltage amplitude of 20 mV. The impedance data was exported from the Novocontrol software into ASCII files. Those were then combined with ASCII based data sets including temperature, partial pressure and humidity sensors of the oven setup using their common time stamp. A custom made plugin kindly provided by the vendor of the data analysis software RelaxIS (rhd-instruments) used in Version 2 and 3 allowed importing the impedance data together with the oven and gas atmosphere information.<sup>143</sup> This turned out as a very reliable and convenient way to make sure that the environmental conditions are precisely known for any single data point of the impedance spectrum.<sup>ii)</sup> This is not the case for other typical setups, as the environmental information during the measurement are averaged over the impedance cycle. In addition the RelaxIS software package allows to handle large data sets of impedance measurement series efficiently. The results of the impedance data fitting were then exported to Origin 2018 (OriginLab corporation) for further data analysis and plotting purposes.<sup>144</sup>

---

<sup>ii)</sup>In the beginning of this project the data were then analyzed with the ZSimpWin software package. Unfortunately version 3.21, which was available, is not the latest version, suffering from compatibility problems with modern computer hard- and software. With this software the environmental parameters, like oven temperature, and gas partial pressures had to be correlated with the impedance data manually.



## 4 Results and discussion

In this chapter the results of the experiments are presented and discussed. In the first section the results of the target preparation are going to be outlined. It will be shown that the target preparation route chosen in this study was feasible for the preparation of such targets needed for the pulsed laser deposition process regarding the composition and their density. Therefore, the results of SEM, XRD and XPS measurements on the targets will be presented. A good characterization of the starting material for the PLD process is essential for a sufficient characterization of the thin films prepared from those targets. In a further section it will be shown that it was possible to prepare thin films with different morphologies via PLD and post-ablation annealing. Here, the focus will be set on the structure and morphology measurements by XRD, GI-XRD and SEM as well as EDS and XPS compositional analysis. Finally, in the last section of this chapter the results of the EIS measurements are presented.

### 4.1 Morphology and chemical composition of the PLD targets

Characterizing the phase composition of a solid bulk material, one of the most important techniques nowadays is X-ray diffraction. Figure 4.1 shows the results of the XRD measurements on the 10CZO, 8CZO and 6CZO targets. The stacked graphs on the left show the XRD pattern as measured with the powder diffractometer in  $\theta/2\theta$  geometry between  $20^\circ$  and  $80^\circ$ . The respective reflex assignments are based on the space group for the pattern given in the right graphs. In those plots the region between  $69^\circ$  and  $72^\circ$  is shown in detail for the three samples, demonstrating the splitting of the (004) reflex for the cubic space group into the (004) and (220) reflex for the tetragonal pattern. The analysis of the X-ray diffraction pattern show no evidence for any other phase than the one that was intended to be prepared by the route described in section 3.1.1. No impurity phases were detected. Whereas the  $\text{CeO}_2$  (10CZO) and the  $\text{Ce}_{0.8}\text{Zr}_{0.2}\text{O}_2$  (8CZO) target show a pattern that corresponds to the cubic space group  $\text{Fm}\bar{3}\text{m}$ , the pattern of the  $\text{Ce}_{0.6}\text{Zr}_{0.4}\text{O}_2$  (6CZO) is assigned to the tetragonal space group  $\text{P}4_2/\text{nmc}$ .<sup>145–147</sup>

As described in section 2.1.2 tetragonality occurs when the cubic fluorite lattice of ceria

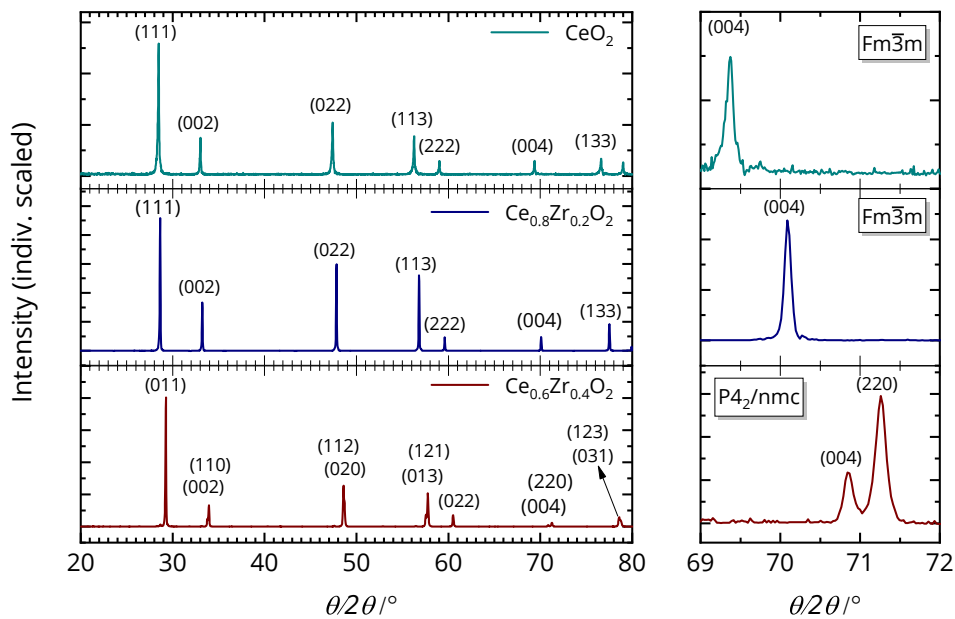


**Figure 4.1:** Comparison of the  $\theta/2\theta$  XRD scans of the 10CZO, 8CZO and 6CZO target. The intensity is scaled individually for every scan. The left graphs show the x-ray diffraction pattern as measured between  $20^\circ$  and  $80^\circ$  with the respective reflex assignments based on the space group for the pattern given in the right graphs. In the right graphs the region between  $69^\circ$  and  $72^\circ$  are shown in detail. The ordinate is individually scaled for each graph. The x-axis scale is the same for each column of graphs in this figure.

becomes critically strained with an increasing concentration of smaller zirconium cations. The ionic radius of a cerium cation is  $r(\text{Ce}^{4+}) = 0.97 \text{ \AA}$  whereas the radius of the zirconium cation is  $r(\text{Zr}^{4+}) = 0.84 \text{ \AA}$ .<sup>148</sup> The reflexes shift towards higher diffraction angles, showing a decrease in the lattice constant from 10CZO to 8CZO. The X-ray diffraction pattern in figure 4.1 confirm this. Once the critical strain is reached, the cubic phase is not stable anymore and a tetragonal phase is formed. As the selection rules for a tetragonally strained cubic lattice change, the cubic reflexes split into two tetragonal ones. The larger the diffraction angle, the larger is the splitting on the  $\theta/2\theta$ -axis. This can be seen in the right detail graphs in figure 4.1 for the cubic (004) reflex, splitting into two reflexes for the tetragonal 6CZO target. As the tetragonal distortion is only small for the  $\text{CeO}_2$  -  $\text{ZrO}_2$  system, the splitting is not visible for all reflexes. Especially for low order reflexes only a small asymmetry of the reflexes can be detected by x-ray diffraction. Thus, it cannot be excluded that a small amount of tetragonal material also exists in the 8CZO target material. But within this study and the sensitivity of the used methods no evidence for that was found.

The XRD analysis confirms the expected formation of a cubic or tetragonal single phase

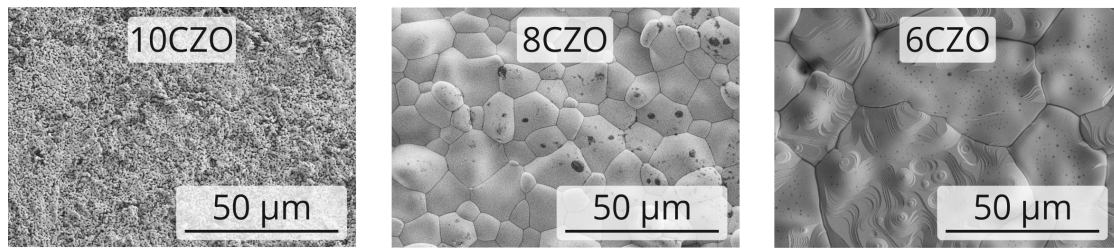


**Figure 4.2:** SEM images (before the first use) of the targets used in the PLD process for this study. The 10CZO target has grain sizes that are in the range of that of the mother powder. The 6CZO surface shows evidence (black domains) for a second phase, like reported by Mamontov et al.<sup>92</sup> The dark features on the 8CZO target surface are due to surface contaminants.

material as reported in the literature before. Whether local inhomogeneities with a different crystallographic phase exist in the targets containing zirconium, as found by Mamontov et al., cannot be excluded, as the necessary neutron diffraction experiments were not conducted.<sup>92</sup> Nevertheless, some evidence for this theory was found in the surface of the 6CZO target. In the SEM image of the surface small domains (dots) within the grains were found that showed a lower contrast, using the secondary electron detector (SE2) that is sensitive to secondary electrons, as well as high energy backscattered electrons. The localized lower contrast indicates a different material or crystallographic surface from which less secondary and/or backscattered electrons are produced. On the contrary, the features observed here are several orders of magnitude larger than those reported by Mamontov et al., who found domains of  $\text{Ce}_{0.4}\text{Zr}_{0.6}\text{O}_2$  with a size of only  $25 - 30 \text{ \AA}$  in a matrix of  $\text{Ce}_{0.7}\text{Zr}_{0.3}\text{O}_2$ .<sup>92</sup> Thus, the features in the 6CZO target surface could very well also be minor phase impurities or originate from local differences in the crystallographic orientation towards the detector of the 6CZO phase itself.

Except for the shift of the reflexes and the splitting, the x-ray diffraction pattern also exhibit differences in intensities between the different targets, although the experimental setup and conditions used were the same. Especially the intensity of the 10CZO diffraction pattern is rather small compared to those of 8CZO and 6CZO. This is evidence that the crystalline quality in the 10CZO target is not as high as that of the 8CZO and 6CZO target. This observation can be explained by taking a look at the SEM images in figure 4.2. Here it is nicely resolved that the average crystallite size of the material in the sintered 10CZO target is significantly smaller than that of the targets containing zirconia, being an indicator for less perfectly grown crystals. As the melting temperature decreases when adding zirconia to ceria, the sintering temperature also decreases. For pure ceria the oven temperature of  $1500 \text{ }^\circ\text{C}$  during the sintering process was not high enough, promoting the growth of large crystallites. The melting temperature of pure ceria is about  $2477 \text{ }^\circ\text{C}$ .<sup>149</sup> As a result of this

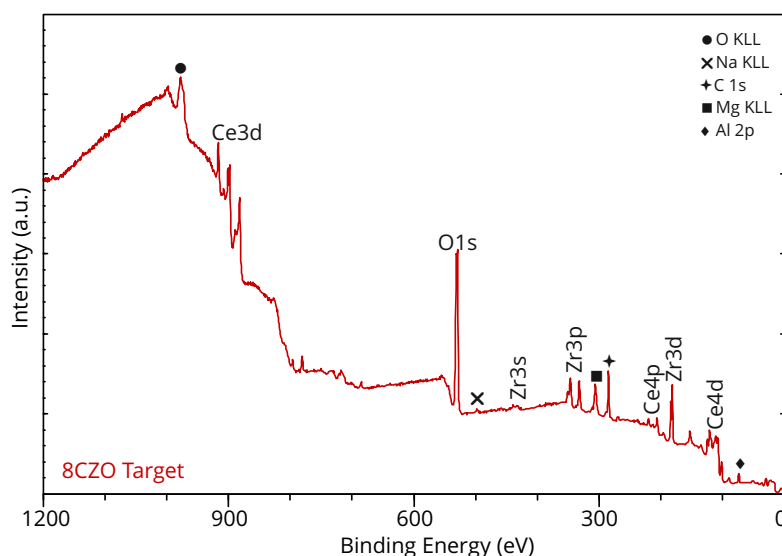


**Figure 4.3:** The graphs shows a survey spectra of the 8CZO target used for thin film ablation via pulsed laser deposition.

the 10CZO target still reveals open pore volume after the sintering process, while the other two targets show a dense surface. Porous targets often lead to a higher droplet formation during the PLD process. As for this study the formation of droplets was rarely observed using the porous 10CZO target, no attempt to enhance the density of the target by higher temperatures or other preparation techniques was made. For the 8CZO and 6CZO targets the temperature of 1500 °C was sufficient to promote the sintering process. All three targets were mechanically stable, which was essential for the use in the PLD process.

In order to determine the composition of the targets and check for impurities not visible in the XRD experiments, the EDS data was evaluated. For 8CZO the sum formula was determined to be  $\text{Ce}_{0.79}\text{Zr}_{0.21}\text{O}_2$ , assuming a stoichiometric amount of oxygen per formula unit. Small concentration of Ca (0.4 at.%) and Al (0.2 at.%) contaminants were found, which is almost below the detection limit of this technology. For the 6CZO target the sum formula was determined to be  $\text{Ce}_{0.60}\text{Zr}_{0.40}\text{O}_2$ . No contaminants were found. The same holds true for the 10CZO target. Its composition was the same as that of the mother powder and no contaminants were found.

In addition to the EDS analysis, XPS measurements were performed on the 8CZO target as described in the experimental section. A survey spectrum of these experiments is shown in figure 4.3. From integrating the area below the Ce4d, Zr3d and O1s region one can estimate the composition. It was taken into account that two different oxygen species were detected, shown by two peaks in the O1s region. By determining the area below each peak separately

and multiplying it with their respective relative sensitivity factors, as well as the other areas, the Ce/Zr atomic ratio was determined to be 4.0, which is exactly the expected value. Except of the Ce, Zr and O signals expected for the 8CZO target, the survey spectrum also contains signals of contaminants, like Mg, C and Al. As the sample was not sputter cleaned before being transferred into the XPS instrument, the detected carbon contaminations were within the typical intensities to be expected. The Mg and Al signals are more interesting. Al on the surface could very well originate from the corundum crucible used in the sintering process. Using the Al2p signal for quantification the area corresponds to 5.1 at.% of aluminum on the surface of the 8CZO target. In addition 3.3 at.% Mg were detected. Nevertheless, it can be concluded that the targets prepared were suitable to be used for the PLD process. The result of this process is going to be described in the next section.

## 4.2 Morphological and chemical characterization of the thin films

In this section the results of the morphological and chemical characterization of the thin films prepared from the different targets by pulsed laser deposition are described. The morphological characterization of the 6CZO thin films described here was done by Raika Oppermann in an affiliated project under the authors supervision. In order to present a complete picture, the results of this affiliated work will briefly be summarized in this section together with the characteristics of the other thin films prepared for this study.

With the intention to determine the chemical composition of the thin films, EDS and XPS measurements were carried out as described in the experimental section (section 3.2.2). Beforehand the morphology and crystallography of the thin films were investigated by SEM and XRD.

**SEM results** In order to examine the thin films morphology, SEM images were taken at various experimental stages, i.e. after the thin film deposition, after the annealing, and after the EIS measurements. Figure 4.4 shows a series of images from a 8CZO sample deposited at a substrate temperature of 700 °C. The film was annealed at 900 °C for 48 h afterwards. The last image on the right was taken after the impedance spectroscopy measurements were conducted.

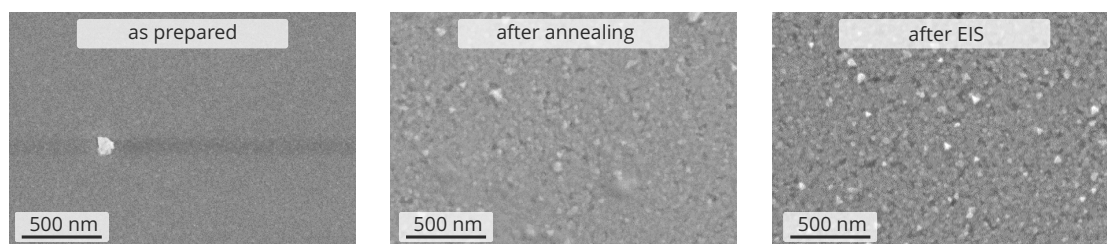


**Figure 4.4:** REM images of a 8CZO thin film deposited at 700 °C (left), annealed at 900 °C for 48 h (middle) and after all impedance spectroscopy experiments (right).

It can be seen that the film after deposition is dense and has a homogeneous crystallite size. After the heat treatment at 900 °C for 48 h the crystals grew from 15 nm to 22 nm, determined from the FWHM of the (111) XRD reflex, using the Scherrer equation.<sup>150,151</sup> As the temperature during the EIS experiments is cycled between rather high temperatures (550 °C to 25 °C) several times, one could expect some additional crystal growth during those experiments. This is not observed in the SEM images taken after the EIS measurements for any sample under investigation. Thus, it is reasonable to assume that no significant change in thin film morphology occurs during the EIS experiments if a sample is pretreated at higher temperatures than those applied during the impedance measurements. Even for samples that were not treated at temperatures higher than those applied during the impedance measurements, a significant grain growth during the electrochemical experiments was not observed.

The same stated above for the 8CZO thin films also holds true for the 6CZO films. For thin films not containing any zirconia a slight difference is observed. Image 4.5 shows a 10CZO thin film annealed at only 600 °C. Although the thin film was deposited at room temperature and annealed at 600 °C only, compared to 900 °C for the 8CZO thin film above, an average crystallite size of 30 nm was determined by XRD, which is 8 nm more than for a comparable 8CZO film. This was confirmed by the SEM images. Comparing SEM images of a 8CZO and 10CZO sample annealed under the same conditions, it can nicely be seen in figure 4.6, that the grain growth for 10CZO is faster at elevated temperatures than for the zirconium containing sample. The shape of the 10CZO grains is better defined than for the 8CZO sample, which shows a rather undefined surface structure in the SEM images. Before annealing the 10CZO grains were 22 nm large in average. For both samples the absolute grain growth was 7 nm and 8 nm respectively, although the 10CZO sample was annealed at 600 °C only. This phenomena was observed for all 10CZO samples deposited and annealed under similar conditions as the 8CZO and 6CZO samples.

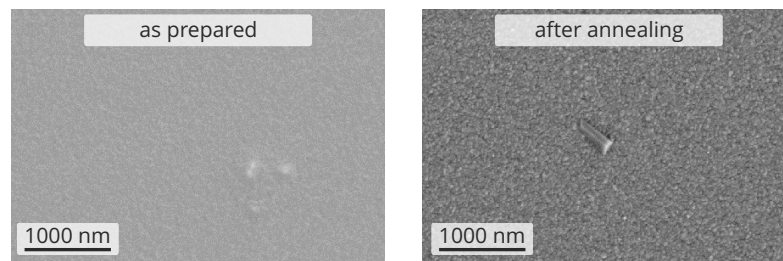


**Figure 4.5:** SEM images of a 10CZO thin film deposited at 25 °C (left) and after annealing at 600 °C for 48 h (right).

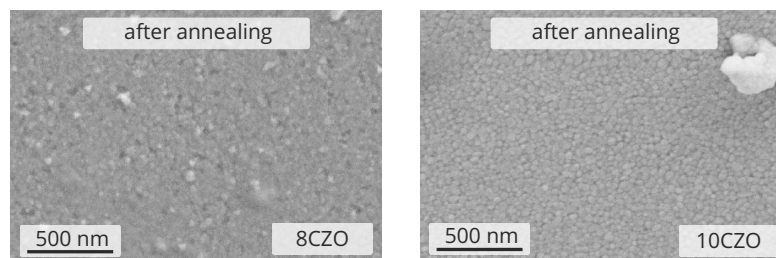


**Figure 4.6:** SEM images of a 8CZO thin film deposited at 700 °C (left) and a 10CZO film deposited at 25 °C (right) after annealing. Both films were annealed at 900 °C for 48 h.

**XRD results** As shown in the SEM results already, the tendency of samples containing zirconium (8CZO and 6CZO) for grain growth is limited. For most of the samples investigated by SEM it was difficult to quantitatively investigate the crystallinity and grain size. Therefore, XRD measurements were performed at room temperature. Figure 4.7 shows the (111) reflex of 10CZO thin films annealed at different temperatures for 48 h. The reference position of the ceria (111) reflex given by the dashed line is extracted from single crystals, as well as powder diffraction data, measured at room temperature.<sup>146,152</sup> The reference position of the (006) sapphire substrate reflex was calculated assuming the space group  $R\bar{3}c$ , and the cell parameters given by the supplier CrysTec.<sup>153</sup> Upon annealing the ceria (111) reflex FWHM decreases from 0.524° for the as deposited thin film (30 °C) to 0.223° after heating the sample to 900 °C for 48 h. Due to the fact that samples with different thicknesses were compared in the measurements shown in figure 4.7, the (111) intensity measured varies between the samples, not allowing a direct comparison. Nevertheless, a comparison of the (111) reflex intensity between as deposited and annealed samples showed an increase in intensity and thus a higher crystallinity of the thin films after heat treatment. An example for this is also shown in figure 4.7. The diffractograms shown were taken at 30 °C and 800 °C from the same sample. Whilst the reflex position of the as deposited sample is shifted to

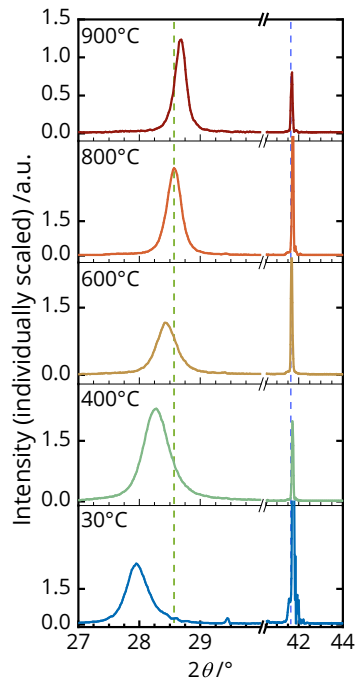


**Figure 4.7:** (111) reflexes of 10CZO thin films annealed at different temperatures for 48 h, measured at room temperature. The intensity axis is individually scaled for each graph. The dashed green line at lower diffraction angle shows the (111) reflex position from two ICSD reference patterns (98-026-2755 and 98-015-5604). The dashed blue line represents the (006) reflex position of the sapphire substrate (*r*-plane) calculated from the lattice constants given by the supplier.

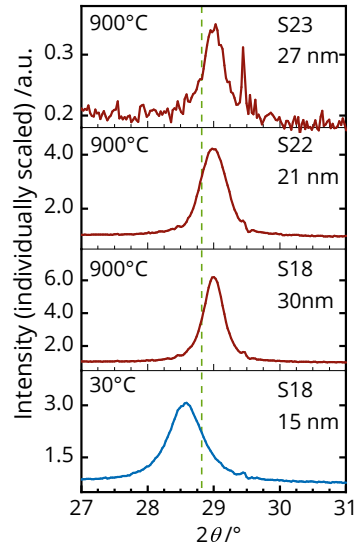


**Figure 4.8:** (111) reflexes of 8CZO thin films annealed at different temperatures for 48 h, measured at room temperature. The intensity axis is individually scaled for each graph. The dashed green line at lower diffraction angle shows the (111) reflex position from two ICSD reference pattern (98-015-7417). The index in the upper right corner of any graph depicts the sample number as well as the crystallite size determined with the Scherrer equation.<sup>150</sup>

lower diffraction angles, compared to the reference position, the position of the (111) reflex of the heat treated sample exactly matches the reference position. A reflex shift towards lower diffraction angles indicates compressive planar stress in the thin films, most likely caused by the lattice mismatch between sapphire and ceria. Upon annealing this stress vanishes.

Figure 4.8 shows the (111) reflex diffraction data of the 8CZO samples used for the impedance experiments. After deposition all samples were annealed at 900 °C for 48 h. Comparing the reflex position of the as deposited (30 °C) sample with the position of the other samples, it can be seen that the compressive planar stress again relaxes upon annealing. Compared to the powder diffraction data, represented by the dashed line, the reflexes of the sample annealed at 900 °C is shifted to higher diffraction angles indicating a tensile stress in the thin film.

Regarding the reflex width (FWHM), a decrease from 0.634° to values between 0.343 to

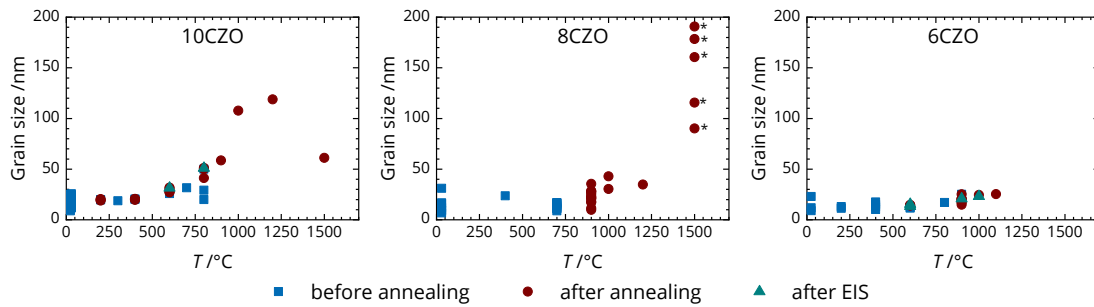


**Figure 4.9:** Grain sizes of all samples determined before annealing, after annealing and after the EIS experiments. For data points before annealing the temperature depicts the deposition temperature. For data points after annealing the temperature axis gives the annealing temperature. Trends in grain growth can nicely be monitored. Data points marked with “\*” symbolize 8CZO samples that were subsequently (6h, 6h, 12h, 12h, 12h) treated for a total of 48 h at 1500 °C. Comparing the graphs it can nicely be seen, that the tendency to form larger grains is most pronounced for 10CZO thin films. Film containing Zirconium show less grain growth at moderate temperatures during deposition as well as during annealing.

0.462° with increasing temperature is observed for this sample composition. Taking the Scherrer equation as an approximation of the grain size as a function of the reflex broadening, one can calculate the grain size of all thin films deposited in this work. These are compared before and after annealing, as well as after conducting the impedance experiments in figure 4.9. Comparing the three graphs it can nicely be seen that the grain growth for moderate deposition as well as annealing temperatures up to 900 °C is more pronounced for 10CZO thin films, compared to those films containing zirconium (8CZO and 6CZO). For these films only subsequent heating at very high temperatures (1500 °C) leads to grain growth. The drawback here is that the 8CZO thin films dewetted under these harsh annealing conditions, forming isolated islands, thus not allowing to measure the electric resistance perpendicular to the surface in EIS measurements anymore.

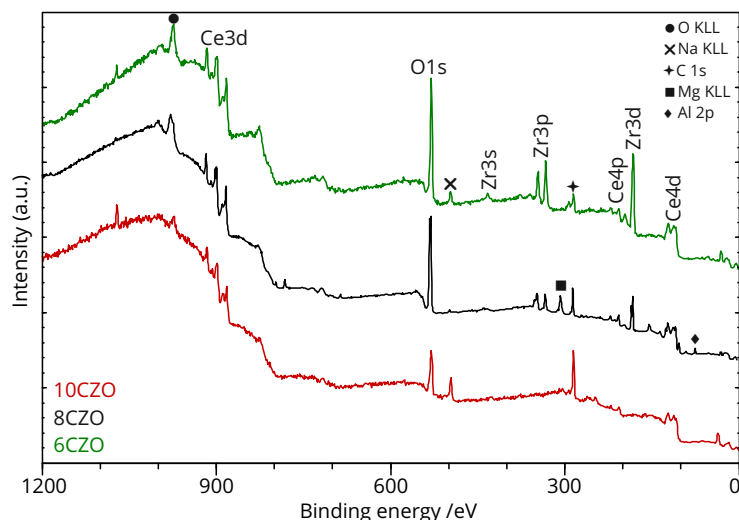


**Figure 4.10:** XPS spectra of a **10CZO** (red) thin film annealed at 800 °C for 48 h, an **8CZO** (black) film annealed at 900 °C for 48 h, and a **6CZO** (green) annealed at 900 °C for 48 h as well. The spectra are shown with an offset and are normalized to their individual maximum. Only minor evidence of impurity signals are found in all films. The Mg and Al signals detected on the **8CZO** thin film most probably originate from the ceramic paste that was used to fix the Pt wires on the samples. It might also result from a contamination of the PLD target material.

**XPS results** Figure 4.10 shows the XPS survey spectra for a 10CZO, 8CZO and 6CZO thin film. The spectra mainly consist of signals that are related to ceria and zirconia being the main components of the thin films. Additionally some small signals from surface impurities, namely Na, Mg, Al, and adventitious carbon are detected. Magnesium and aluminum are only detected on the 8CZO film. These impurities are unique to this specific film, as it was measured after the platinum wires were attached to the sample with Ceramabond ceramic paste, mainly consisting of MgO and Al<sub>2</sub>O<sub>3</sub>. Measurements of another 8CZO sample did not show these impurities. The fact that Mg was only measured as an impurity on the electrically contacted thin film shows that the impurities are most likely surface contamination's due to the ceramic paste used to fix the Pt wires. The XPS analysis of the PLD targets (see subsection 4.1) also revealed Mg and Al contaminations. These could principally have been transferred to the thin films during the PLD process. However, as some of the target material is always irradiated by the laser before material is actually ablated on the surface of the substrates, these surface contaminations of the target are removed prior to the ablation. Table 4.1 shows the composition of the different thin films, determined from the XPS spectra above. The sum formulas were determined as described in section 4.1. As expected, the thin films show the same composition as the targets within the uncertainty of the method. The atomic composition was determined by fitting an underground to the O1s, Ce4d, and Zr3p

**Table 4.1:** Composition of the thin films determined from the XPS spectra in figure 4.10. All three films show the same composition as the targets they were produced of. The oxygen composition is calculated from those peaks in the O1s region at energies below 531 eV.

Sample	Composition /At-%			Ce/Zr	Formula
	O1s	Ce4d	Zr3p		
10CZO	59.6	27.9	0	-/-	Ce <sub>0.99</sub> O <sub>2.12</sub>
8CZO	39.1	16.4	4.2	3.9	Ce <sub>0.87</sub> Zr <sub>0.22</sub> O <sub>2.08</sub>
6CZO	31.8	11.6	8.0	1.5	Ce <sub>0.62</sub> Zr <sub>0.43</sub> O <sub>1.69</sub>

region, calculating the composition using the respective relative sensitivity factors. In order to get the composition of the thin films correctly, it was necessary to divide the O1s area into two areas, determined by the method described before in section 4.1. The detail spectra from the O1s region revealed that the signal was composed of two components. Eliminating the component at energies above 531 eV resulted in the compositions given in table 4.1.<sup>154</sup> Concluding the above paragraph on the morphology and the composition of the ceria-zirconia thin films, it can be noted that samples containing zirconium tend to show less grain growth upon elevated annealing or deposition temperatures than pure ceria thin films. Deposition or annealing of the thin films at high temperatures leads to higher crystalline quality of the thin films, as well as relaxation of compressive stress. For the samples prepared in this work the grain sizes were in a quiet small regime, below 60 nm for all three compositions. It was one goal of this work to find methods for preparing CZO thin films in a controlled manner, having the possibility to tune the thickness, morphology and especially the grain boundary density. While tuning the thickness is easily achieved by variation of the laser energy and number of laser pulses, tuning the grain boundary density over a wide range was difficult to achieve, due to the fact that zirconium seems to hinder the grain growth at moderate annealing temperatures. Going to temperatures as high as 1500 °C, grain growth starts, but the thin films tend to dewett as well. For the desired in plane measurement of the impedance dewetted films are not suitable. In addition, within another project affiliated with this work, carried out by Julian Zahnnow under supervision of the author of this dissertation, evidence for a chemical reaction between ceria zirconia thin films and the sapphire substrate were found, forming an aluminum containing phase at high temperatures.<sup>155,156</sup> This had to be avoided for the use of the thin films within the experiments in this project.

### Discussion of thin film growth conditions and morphology

For the impedance experiments conducted on the ceria thin films, it was crucial to know, whether the films would change during the heating treatment. Therefore, the grain size as a function of deposition and annealing temperature was evaluated. The results are shown in figure 4.9 on page 65. The tendency for grain growth for the pure ceria thin films is relatively moderate and limited at temperatures below 900 °C. Thin films containing zirconium show even less grain growth. These findings are contradicting the generalized grain growth model.<sup>157</sup> Bruke's and Turnbull formulated the well known parabolic grain growth model for metals.

$$G^n - G_0^n = 2M\gamma t \text{ with } n = 2 \quad (46)$$

For metal oxides many grain growth experiments showed a non parabolic grain growth behavior with grain growth exponents of  $n = 2 - 4$ , instead of 2 as in the parabolic growth in equation (46).<sup>158</sup> Based on these models a continuous grain growth would be expected as the average grain size  $G$  as a function of growth time  $t$  is proportional to the grain boundary energy  $\gamma$  and the grain boundary mobility  $M$ .  $G_0$  is the initial grain size after thin film deposition in this case. In contrary to this expectation, nanocrystalline materials are known to show grain growth up to a certain limited size, when only moderate temperatures are applied.<sup>159–161</sup> This is caused by the limited grain boundary migration and can in addition be affected by defects in the material. As already discussed by Cahn in 1962, nanocrystalline materials tend to show grain growth at intermediate temperatures, comparable to those applied in the annealing procedures in this work, as long as the microstrain is decreased.<sup>162,163</sup> As soon as the microstrain is relaxed the growth process stops at a meta-stable state. Only if the temperature is significantly increased, as it was done for some 10CZO and 8CZO samples in figure 4.9, further grain growth is promoted. These effects were studied by Rupp and coworkers on ceria thin films as well.<sup>158</sup> They observed that for spray pyrolyzed films microstrain was relaxed after 5 – 15 h heat treatment between 600 °C – 900 °C. The grain size trends shown in figure 4.9 are consistent with these findings. After pulsed laser deposition the grain sizes are smaller than 30 nm for most of the thin films, independent of the substrate temperature during deposition. Significant grain growth is not observed during annealing for 48h, if the annealing temperature does not exceed 850 °C. In addition, it can also be concluded that the introduction of zirconium into the ceria lattice seems to hinder the grain growth during annealing. The more zirconium-rich the samples are, the less grain growth is observed.

The relaxation of microstrain can be monitored in the shift of the XRD (111) reflex center

shown in figure 4.7 and 4.8 on page 64. Additionally the FWHM of the reflex decreases with temperature, indicating crystallite growth. The ex situ measurements presented here were confirmed by in situ XRD heating experiments not shown in the main text of this dissertation. Unfortunately several attempts to conduct in situ heating XRD experiments on thin films for several days failed during the experimental work period of this project, which was mainly due to technical reasons and limited accessibility of the XRD instrument. In order to give the reader an impression of such an experiment, the data of one of the experiments is plotted in S.6.1 in the supplementary section. The thin film samples were mounted within a gas tight, heatable sample oven, equipped with beryllium windows, transparent for x-ray light. Using this equipment it was possible to anneal the thin films under defined atmosphere and a programmed temperature profile. Such a setup does also allow studying the influence of the oxygen partial pressure on the annealing behavior of the thin films, as the oven is gas tight, and has inlets for applying a controlled gas atmosphere. It would certainly be interesting to conduct long term in-situ annealing measurements for a series of samples of different compositions, in order to further confirm that the crystallite growth actually stops after a certain time at a given temperature. In conclusion, the XRD results confirm the interpretation that the thin films relax strain during the annealing process.

Considering the results of the thin film characterization as a function of the preparation conditions and chemical composition, one can conclude the following. For the PLD ablation process changes of the morphology as a function of the preparation conditions within the 10CZO, 8CZO and 6CZO thin films series are rather small, not significantly depending on the deposition temperature. This is remarkable, as it is common sense that thin film ablation via PLD is sensitive to variations on the aforementioned parameters.<sup>164</sup> In contrast to this, a study on the impact of ablation parameters on the film morphology of GDC and YSZ thin films by Infortuna and coworkers showed that an oxygen pressure of  $10^{-2}$  mbar during the ablation results in dense GDC and YSZ films, not significantly influenced by the temperature in the range of 30 – 900 °C.<sup>131</sup> The results achieved in this work show that these findings can also be applied on aliovalently doped CZO thin films. All thin films ablated using substrate temperatures between 30 – 700 °C were dense due to the relatively low oxygen background pressure of  $10^{-2}$  mbar. A low background pressure assures that no agglomerates are formed in the plasma plume before the material hits the substrate surface. This results in the growth of dense films even at substrate temperatures as low as 30 °C. Infortuna et al. reported that for lower deposition temperatures disordered but coherent grains are deposited forming a dense film.<sup>131</sup> This was not studied in detail in the course of this work, nevertheless a cross-section SEM image of a 10CZO thin film deposited at a substrate temperature of only 30 °C shown in figure 4.11 confirms the findings of Infortuna

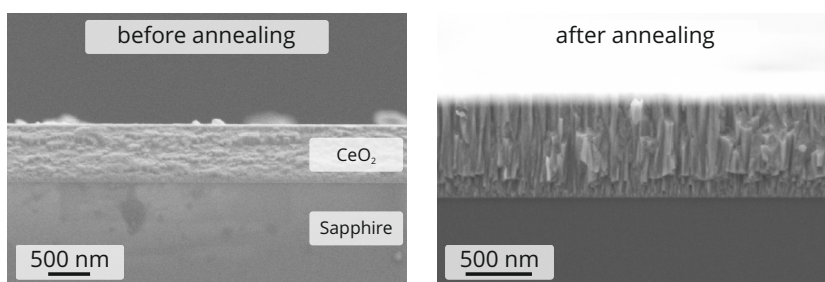


**Figure 4.11:** SEM images of 10CZO thin film cross sections before (left) and after (right) annealing. Before annealing the thin film is composed of disordered and coherent grains. After annealing the thin film shows a columnar grain structure.

and coworkers. Interestingly a cross-section SEM image of a sample that was ablated at 30 °C and annealed afterwards at 600 °C shows columnar grain shapes. The formation of columnar grains is a result of the driving force for the grain growth in these films, which is microstrain relaxation. Once the microstrain is relaxed, grain sizes of the thin films do not change significantly anymore, if the annealing temperature does not exceed a certain limit. This has a certain implication for the other experiments conducted in this work. The lower the temperature of a sample during a respective experiment, the slower the microstrain will be released and the slower grains will grow. This allows for long series of EIS experiments at moderate temperatures up to 550 °C without a significant change in the thin film morphology, even if the samples still show residual strain. The aforementioned effect is especially important for the measurements on the thin films with the smallest average crystallite sizes. As it is reasonable to assume that the average grain size of the thin films does not change during the EIS experiments, changes of the grain boundary density do not have to be taken into account, when discussing the results of the impedance measurements.

Aside from the thin film morphology, the determination of the thin film composition is crucial for the understanding of the impedance spectroscopy results. The XPS experiments presented in section 4.1 reveal that some of the films contain Na, Mg and Aluminum in minor concentrations. The materials and devices used for the preparation of the targets, and the annealing of the samples give rise to the assumption that these are most probably surface contaminations coming from the crucibles used to load the PLD targets and thin film samples into the oven for annealing. In addition a ceramic paste was used to fixate the electric platinum connection wires to the samples, that is known to contain the detected contaminations. The identification of the source of this contamination would be helpful for further experiments of this kind, as the contaminants might influence the defect chemistry of the thin films, and thus the impedance results. Alkali earth metals or other elements

like those detected in the XPS experiments could result in a doping of the thin films. The elements detected are potential acceptors in the sense of defect chemistry and could potentially fix the vacancy concentration in the material over a certain oxygen partial pressure range. For getting a better understanding whether the contamination is only on the surface or incorporated in the thin films, systematic studies by more surface sensitive techniques are indicated. This could be time-of-flight secondary ion mass spectrometry (TOF-SIMS) for example. This technique allows to detect contaminations of this kind with very high sensitivity down to the ppb range. Unfortunately, this technique is only semi-quantitative. Thus, defined standards would be needed to determine the concentration of a certain contamination. Preliminary results obtained on some thin films during this work showed that the method is absolutely suitable to clarify whether certain dopant elements can be detected on the surface or in the bulk of the thin films.

## 4.3 Electrochemical impedance spectroscopy results

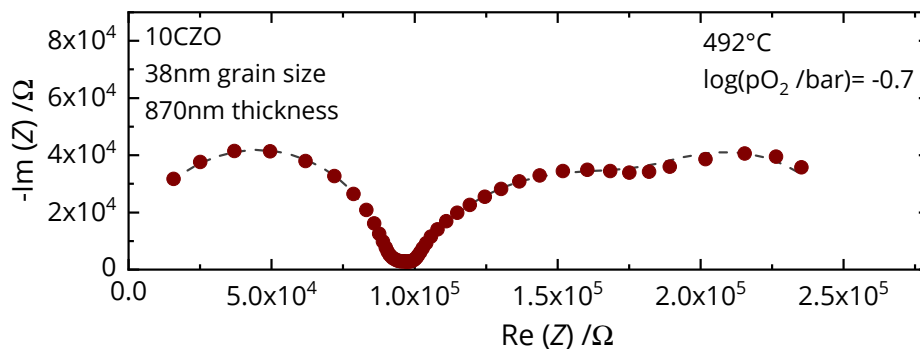
In the following subsections the results of the EIS experiments are presented. This section is structured into subsections in order to give the reader an easier overview over the results. First, the results under dry conditions will be presented and discussed in section 4.3.1. In the following two sections 4.3.2 and 4.3.3 the results under humidified atmosphere are presented dividing them into two temperature regimes.

### 4.3.1 Measurements under dry atmosphere

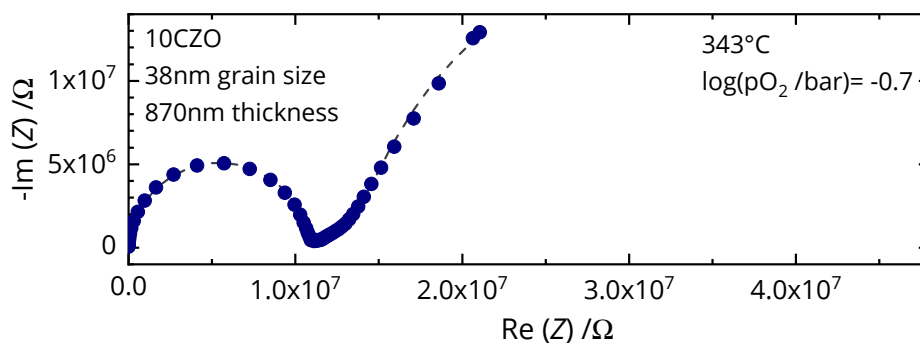
#### 10CZO thin films

Figure 4.12 exemplary shows a Nyquist plot of the electrochemical impedance experiment data measured at 492 °C under dry atmosphere containing 80 % Ar and 20 % O<sub>2</sub>, resulting in an oxygen partial pressure of  $pO_2 = 200$  mbar or  $\log(pO_2 / \text{bar}) = -0.7$  on a logarithmic scale. At this temperature three nicely separated semicircles are measured. Going to lower temperatures the third semicircle at low frequencies (on the right side in the Nyquist representation) increases stronger than the other two. Due to this higher impedance in the low frequency regime in combination with only a slight increase of the pseudo-capacity from 4.5 fF to 6.0 fF with decreasing temperature, the low frequency semicircles and the medium frequency arc cannot be separated anymore. Instead, another feature in the impedance spectra becomes visible at intermediate frequencies. In the lower temperature regime the Nyquist plots show a semicircle between the high and low frequency semicircles (see figure 4.13), that is not as clearly separated from the other features as at higher temperatures. A similar feature in impedance data of mixed electronic ionic conductors was investigated by McNealy and coworkers.<sup>165</sup> In this publication the intermediate frequency impedance arc is associated with a spreading resistance that is a function of the excitation frequency arising from the sample and electrode geometry, as well as the relative impedances of the electrolyte and the electrolyte-electrode interface.

Due to the above observations quiet simple equivalent circuits were found to be suitable for the simulation of the impedance spectra. For high temperatures between 500 °C and 550 °C four parallel RQ elements serially connected with each other were used. Here, R symbolizes an ohmic resistance and Q symbolizes a constant phase element (CPE).<sup>166,167</sup> Between 300 – 500 °C three parallel RQ elements in series were applied. For lower temperatures the low frequency semicircles vanished subsequently, so that equivalent circuits of only two or one RQ element in series were used for fitting the EIS data.



**Figure 4.12:** Nyquist plot of one impedance measurement conducted on a pure ceria thin film (10CZO) with 38 nm grain size and 870 nm thickness at a temperature of 492 °C in the sample vicinity and a oxygen partial pressure of  $\log(pO_2 / \text{bar}) = -0.7$ . The blue dots depict the impedance at different frequencies, whilst the gray dashed line depicts the simulated data, calculated with the equivalent circuit shown.



**Figure 4.13:** Nyquist plot of one impedance measurement conducted on a pure ceria thin film (10CZO) with 38 nm grain size and 870 nm thickness at a temperature of 343 °C in the sample vicinity and a oxygen partial pressure of  $\log(pO_2 / \text{bar}) = -0.7$ . The blue dots depict the impedance at different frequencies, whilst the gray dashed line depicts the simulated data, calculated with the equivalent circuit shown.

This approach is a solely phenomenological one, driven by the amount of observed features in the Nyquist and Bode (figure 4.14) plots, not accounting for possible physical pathways of charge carriers. A similar approach is also used in literature.<sup>168</sup> Other more complex equivalent circuits might also be applicable to simulate the impedance data, taking several possible parallelly and serially connected charge transport pathways in the columnar CZO thin films into account. A possible approach is presented by Jasinski et al..<sup>169</sup> Here, it is assumed that a difference between the grain boundary and grain impedance is detectable. This does not apply for all the data measured in the course of this project. The relatively simple equivalent circuits were used in order to allow batch processing of several impedance spectra from one measurement series. Only by this approach it was possible to evaluate the

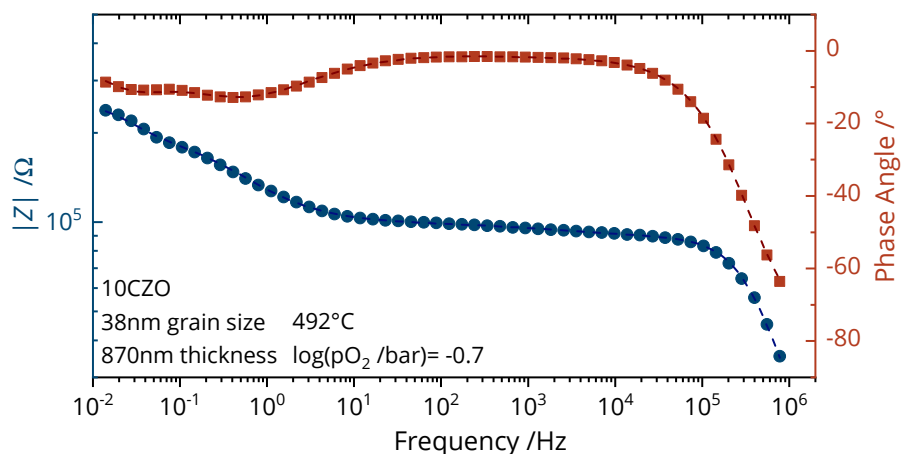


**Figure 4.14:** Bode plot of one impedance measurement conducted on a pure ceria thin film (10CZO) with 38 nm grain size and 870 nm thickness at a temperature of 492 °C in the sample vicinity and a oxygen partial pressure of  $\log(pO_2 / \text{bar}) = -0.7$ . The blue dots depict the impedance, whilst the red squares depict the phase angle at different frequencies. Dashed lines depicts the simulated data, calculated with the respective equivalent circuit.

huge amount of data generated by the electrochemical impedance spectroscopy experiments in a reproducible way and reasonable amount of time. Albeit the shielded measurement setup the impedance data at temperatures between 200 °C and 250 °C were barely evaluable under dry conditions. This is due to the fact that for the measurements under dry conditions the resistances of the sample is too high to be measured without too much noise from external electromagnetic fields, coupling into the setup or exceeding the maximum range of the measurable impedance of the impedance analyzer used in this project.

For all equivalent circuits used to fit the data it was assumed that the first semicircle at high frequencies depicts the electric response of the CZO thin films. In the following the result of the data evaluation on the data collected under dry conditions are described, starting with the nominally pure ceria thin films. Figure 4.15 and 4.16 show Arrhenius type plots of the two 10CZO films measured at an atmosphere with an oxygen partial pressure of 200 mbar which is equivalent to a value of  $\log(pO_2 / \text{bar}) = -0.7$ . For the sample with 38 nm average crystallite size two slopes in the Arrhenius plot are monitored. In the temperature regime between 250 °C – 400 °C the slope is more negative than in the high temperature regime. As the slope in this kind of Arrhenius plot is directly connected to the activation energy of a hopping transport process of the charge carriers (see equation (15)), the activation energy was calculated to be  $E_{A, \text{high T}} = 1.00 \text{ eV}$  for the temperature regime between 425 °C – 550 °C and  $E_{A, \text{low T}} = 1.45 \text{ eV}$  in the lower temperature regime for the 10CZO sample with a film thickness of 870 nm. For the slightly thinner sample with a thickness of 770 nm and an

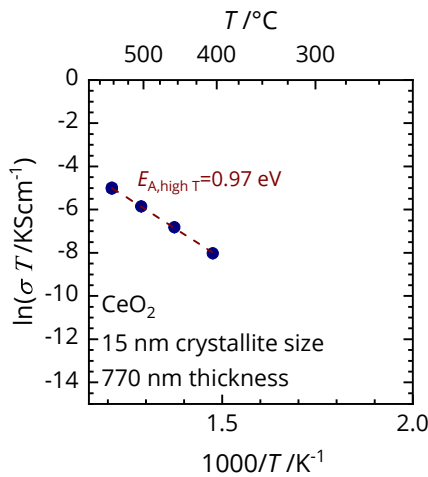


**Figure 4.15:** Arrhenius plot derived from the impedance measurement conducted on a pure ceria thin film (10CZO) with 15 nm grain size and 770 nm thickness between 400 °C–550 °C and a oxygen partial pressure of  $\log(p_{\text{O}_2}/\text{bar}) = -0.7$ . The data points are the bulk conductivity derived from the bulk impedance of the equivalent circuit.

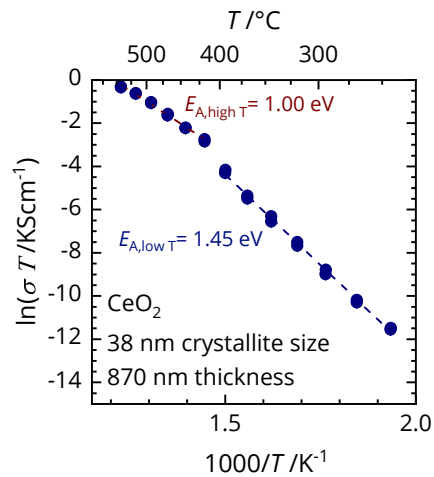


**Figure 4.16:** Arrhenius plot derived from the impedance measurement conducted on a pure ceria thin film (10CZO) with 38 nm grain size and 870 nm thickness between 250 °C – 550 °C and a oxygen partial pressure of  $\log(p_{\text{O}_2}/\text{bar}) = -0.7$ . The data points are the bulk conductivity derived from the bulk impedance of the equivalent circuit.

average crystallite size of only 15 nm a similar slope, and thus a similar activation energy of  $E_{A,\text{high } T} = 0.97$  eV was determined for the high temperature regime. For the low temperature regime the impedances measured were too high to measure reliable data.

It shall be mentioned here that all graphs shown for the results of the impedance measurements contain error bars, albeit they are almost not visible in any graphs. These errors are calculated assuming an uncertainty of  $\Delta T = 1$  K for the temperature measurement, as well as the absolute fitting error  $\Delta\sigma$  from the least mean squares fitting routine determining the resistances from the equivalent circuit simulation.

The impedances of all samples were measured at different oxygen partial pressures between  $10^{-6}$  bar – 0.2 bar. For understanding the defect chemistry of the ceria thin films under investigation, it is crucial to determine how the oxygen partial pressure influences the charge carrier concentration, and thus the conductivity. Figure 4.17 and 4.18 show the results of the measurements for the 10CZO thin films. The conductivity is shown on a logarithmic scale as a function of the logarithmic oxygen partial pressure. The temperature is given by a color scale next to the graph. In addition, data points from the same temperature series have the same symbol shape. It can be nicely seen, that the conductivity does not change as a function of the oxygen partial pressure for a given temperature. In addition one can observe, that the conductivity of the thin film with bigger crystallites (figure 4.18) is about one to two

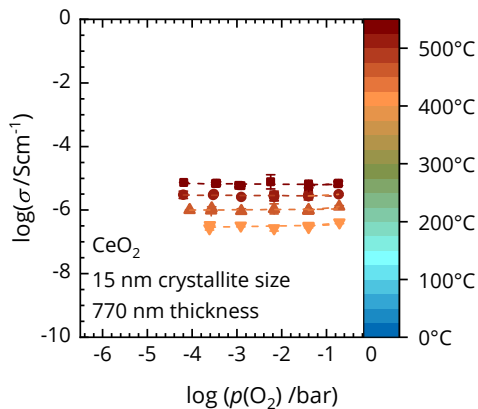


**Figure 4.17:** Bulk conductivity of a ceria thin film (10CZO) with 15 nm grain size and 770 nm thickness at different oxygen partial pressures and different temperatures. Sample temperatures are given by the color scale. The dashed line is intended to give a guide to the eye.

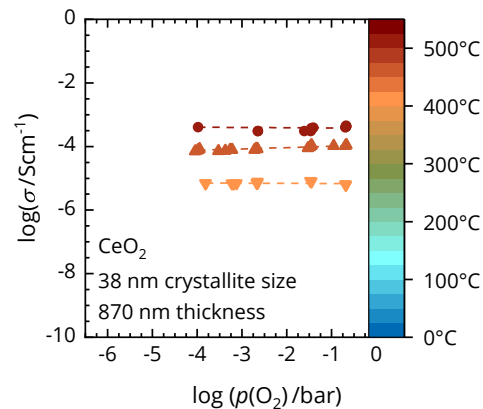


**Figure 4.18:** Bulk conductivity of a ceria thin film (10CZO) with 38 nm grain size and 870 nm thickness at different oxygen partial pressures and different temperatures. Sample temperatures are given by the color scale. The dashed line is intended to give a guide to the eye.

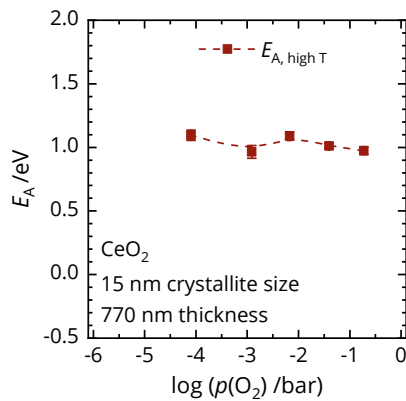


**Figure 4.19:** Activation energies of a ceria thin film (10CZO) with 15 nm grain size and 770 nm thickness at different oxygen partial pressures. The dashed line gives a guide to the eye.

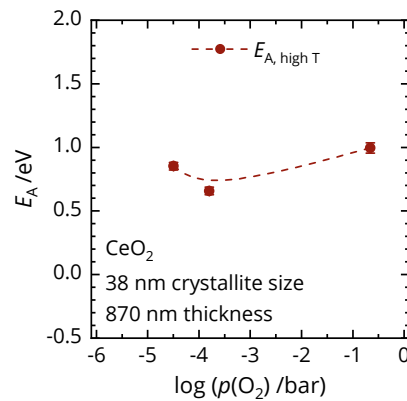


**Figure 4.20:** Activation energies of a ceria thin film (10CZO) with 38 nm grain size and 870 nm thickness at different oxygen partial pressures. The dashed line gives a guide to the eye.

orders of magnitude higher than that of the sample with smaller crystallites (figure 4.18). Figure 4.19 and 4.20 show the activation energies extracted from the Arrhenius plots in figure 4.15 and 4.16 as a function of the  $p_{O_2}$ . The activation energies of the 10CZO samples for the investigated temperature range are relatively stable over the  $p_{O_2}$  range investigated in this project. Albeit, slight changes without clear trends occur for the 15 nm crystallite size sample in figure 4.19. For the 38 nm crystallite size sample it shall be noted that the data

points for  $\log(pO_2/\text{bar}) = -2$  and  $-3$  are missing due to the fact that for this particular sample run an experimental setup had to be used in which it was not possible to adjust the missing oxygen partial pressures in a stable manner. Unfortunately, after the measurements under humid conditions described later were done, the samples interdigital electrode was damaged when some parts of the measurement setup had to be fixed before being able to perform the missing measurements.

### 8CZO and 6CZO thin films

Analogue to the 10CZO results figure 4.21 shows the Arrhenius plots of the temperature dependent measurements of the three 8CZO samples at oxygen partial pressures in the range of  $10^{-6} - 0.2$  bar. The data points are color-coded by the partial pressure that was recorded during the measurement of the temperature series.

In literature on mixed ionic electronic conductors typically one activation energy is given for the whole temperature range. Looking at the plots carefully, one can see that most of the Arrhenius plots exhibit two different slopes. One slope is found in the high temperature regime corresponding to a activation energy  $E_{A,\text{high T}}$  between  $425 - 550^\circ\text{C}$  and one in the lower temperature regime between  $250 - 400^\circ\text{C}$ , corresponding to  $E_{A,\text{low T}}$ . figure 4.25 shows the activation energies as a function of  $pO_2$ . For two 8CZO samples with 12 nm and with 21 nm crystallite size, changes of the activation energy in the low and high temperature regime with  $pO_2$  were evaluated, whilst the activation energies of the third sample with 27 nm does not change with oxygen partial pressure.

Whilst the trends in activation energies are quiet different between the samples, they still show similar trends in the temperature dependent conductivity with changing  $pO_2$ , as shown in figure 4.21. For all three 8CZO samples the conductivity is larger in the high temperature regime for low oxygen partial pressures, subsequently increasing with decreasing oxygen partial pressure. This shows that for the 8CZO samples the conductivity is a function of the oxygen partial pressure. This trend can even better be seen plotting the conductivity of the samples at the same temperature as a function of the oxygen partial pressure, as done for the temperature range between  $425^\circ\text{C}$  and  $550^\circ\text{C}$  in figure 4.23. Here it can nicely be seen that the conductivities of the 8CZO layers show a slope in the range of  $-0.13$  to  $-0.10$ , slightly higher than  $-\frac{1}{6}$ , in the double-logarithmic plots against the oxygen partial pressure. One exception from this is the thinnest 8CZO thin film (left graph in figure 4.23). Here the slope flattens from  $-0.11$  to  $-0.02$  with decreasing temperature.

Before describing the results of the 6CZO thin films under dry atmosphere it shall be noted that most of these results were measured within the Master's thesis of Raika Oppermann as

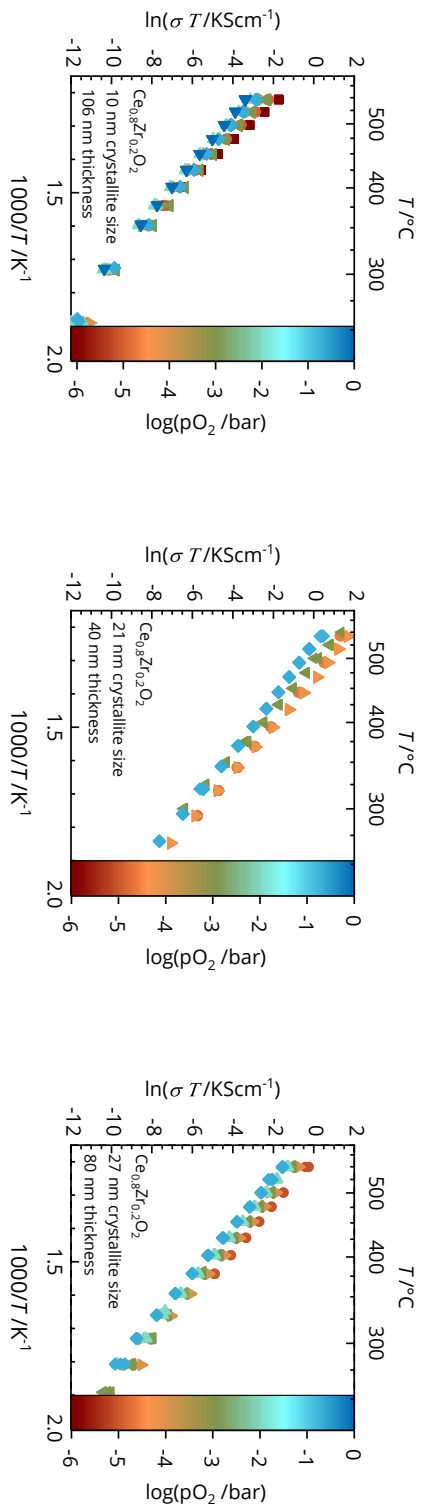


**Figure 4.21:** Comparison of the Arrhenius plots derived from the impedance measurement conducted on a  $\text{Ce}_{0.8}\text{Zr}_{0.2}\text{O}_2$  thin films (8CZO) with *left*) 10 nm grain size and 106 nm thickness, *middle*) 21 nm grain size and 40 nm thickness, and *right*) 27 nm grain size and 80 nm thickness between 550 °C - 250 °C for different oxygen partial pressures shown by the color scale in each graph.

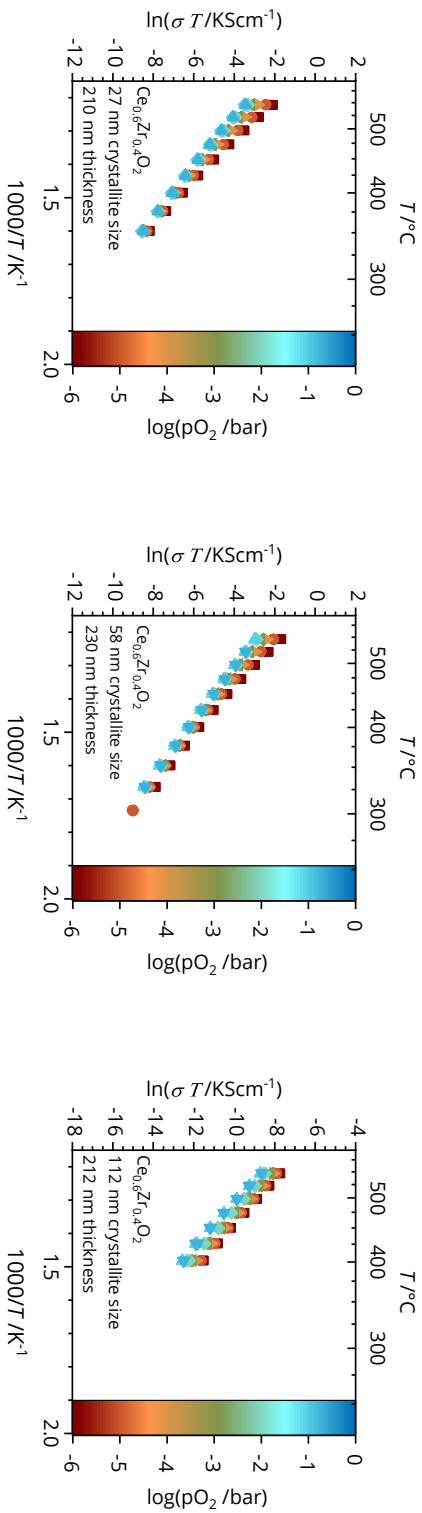


**Figure 4.22:** Comparison of the Arrhenius plots derived from the impedance measurement conducted on a  $\text{Ce}_{0.6}\text{Zr}_{0.4}\text{O}_2$  thin films (6CZO) with *left*) 27 nm grain size and 210 nm thickness, *middle*) 58 nm grain size and 230 nm thickness, and *right*) 112 nm grain size and 212 nm thickness between 550 °C - 300 °C for different oxygen partial pressures shown by the color scale in each graph.

a sub-project under the authors supervision during this dissertation research project.<sup>170</sup> In order to present a complete and comparative picture, the data was reevaluated here using the same impedance models, batch fitting routines, and graphical templates as for the rest of the data in this manuscript.

Figure 4.22 shows the Arrhenius plots of the 6CZO samples under dry conditions in the temperature range between 300 – 550 °C. It can nicely be seen, that the trends and slopes are the same than for the 8CZO samples. For analyzing this in more detail, the conductivity of the 6CZO films is plotted as a function of the oxygen partial pressure in figure 4.24, together with the results for the 8CZO thin films on the same page in figure 4.23. The conductivity of the 6CZO samples decreases with increasing oxygen partial pressure, just like in the 8CZO films. Using the double logarithmic plots it can nicely be seen that the slopes for the 6CZO layers are almost constant with temperature, and in the same order than for the 8CZO samples. Just like for the latter ones, the 6CZO sample with the smallest average crystallite size also shows a slope increasing with decreasing temperature from  $-0.12$  to  $-0.03$  for the logarithmic conductivity plotted against the logarithmic oxygen partial pressure. It is noteworthy here, that the average crystallite size for the 8CZO samples is only 10 nm, whilst the average size of the 6CZO sample is 27 nm. This mean crystallite size is the same than that of the 8CZO layer with the largest crystallites, not showing a change of the slope in the  $\log \sigma$  vs.  $\log(pO_2)$  plots, in contrary to the 6CZO thin films.

Like the conductivity, the activation energies also show a similar trend with changing oxygen partial pressure for the 6CZO (figure 4.26) samples as for the 8CZO (figure 4.25) thin films. The two samples with the smallest average crystal size exhibit two slopes in the Arrhenius plots, resulting in two activation energies, one for the high temperature  $E_{A,high T}$ , and one for the low temperature range  $E_{A,low T}$ . The difference in  $E_{A,high T}$  and  $E_{A,low T}$  gets smaller with increasing oxygen partial pressure. An exception is found for the 8CZO and 6CZO thin films with the largest grains, where the activation energies for both temperature regimes are almost equal and constant for the partial pressure range investigated. Looking at the activation energy plots of the samples with intermediate mean crystallite sizes, one can note that for the 8CZO sample the activation energy in the low temperature regime is larger than for the high temperature regime. This behaviour is also found for the 10CZO sample with 38 nm crystallite size in figure 4.16. For the 6CZO sample this is not the case. For all 6CZO samples investigated in this study  $E_{A,high T}$  is equal or larger than  $E_{A,low T}$ .

Regarding the absolute conductivity values of the thin films measured under dry conditions it can be noted that these are in a quiet broad range of about four orders of magnitude for the different 6CZO and 8CZO samples at the same temperature, which can be seen more nicely in figure 4.27, discussed later.

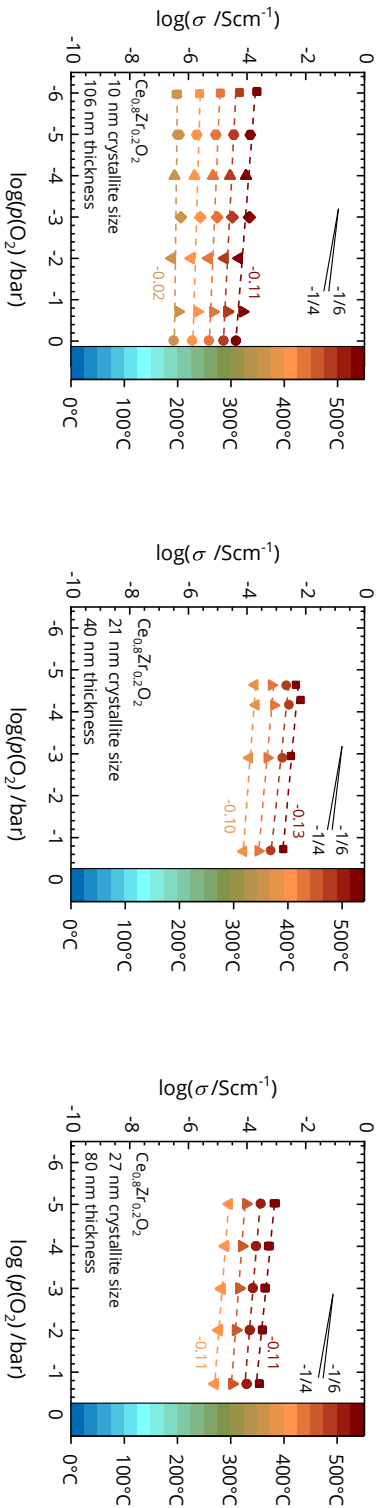


**Figure 4.23:** Comparison of the bulk conductivity of  $\text{Ce}_{0.8}\text{Zr}_{0.2}\text{O}_2$  thin films (8CZO) with increasing grain size from 10 – 27 nm (left to right) and 40 – 106 nm thickness at different oxygen partial pressures and different temperatures. Sample temperatures are given by the color scale. The dashed lines represent a linear fit of the data. For the highest and the lowest temperatures the value of the slopes that correspond to characteristic values derived from the Brouwer diagram (figure 2.3) are shown for guidance.

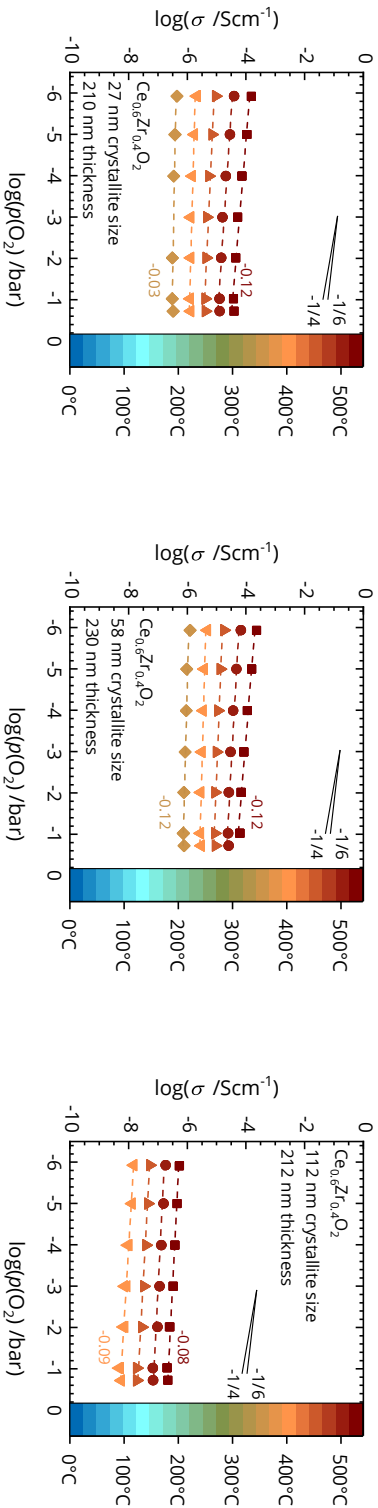


**Figure 4.24:** Comparison of the bulk conductivity of  $\text{Ce}_{0.6}\text{Zr}_{0.4}\text{O}_2$  ceria thin films (6CZO) with increasing grain size from 27 – 112 nm and 210 – 230 nm thickness at different oxygen partial pressures and different temperatures. Sample temperatures are given by the color scale. The dashed lines represent a linear fit of the data. For the highest and the lowest temperatures the value of the slopes are given in the respective color. In addition slopes that correspond to characteristic values derived from the Brouwer diagram (figure 2.3) are shown for guidance.

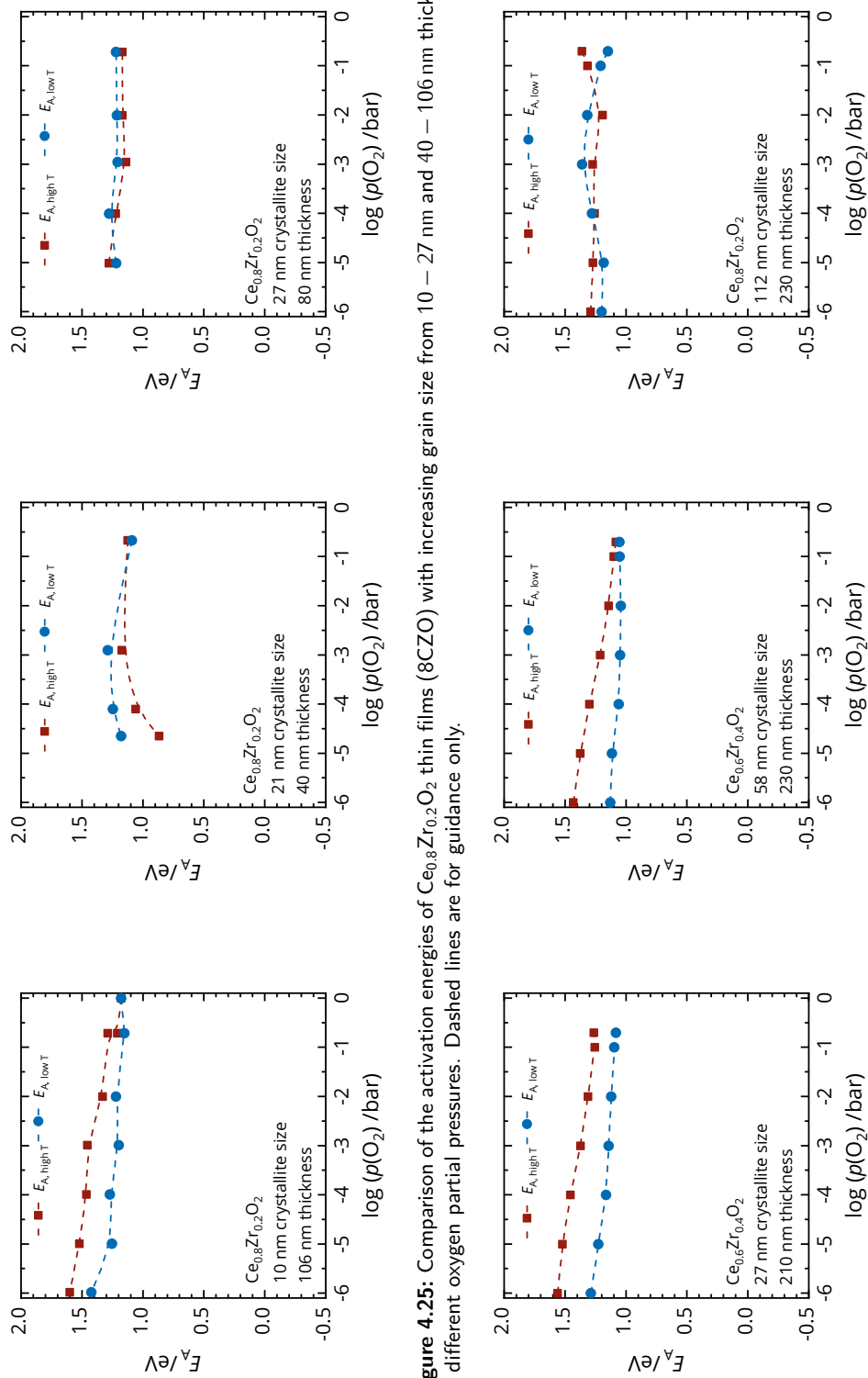


**Figure 4.25:** Comparison of the activation energies of  $\text{Ce}_{0.8}\text{Zr}_{0.2}\text{O}_2$  thin films (8CZO) with increasing grain size from 10 – 27 nm and 40 – 106 nm thickness at different oxygen partial pressures. Dashed lines are for guidance only.

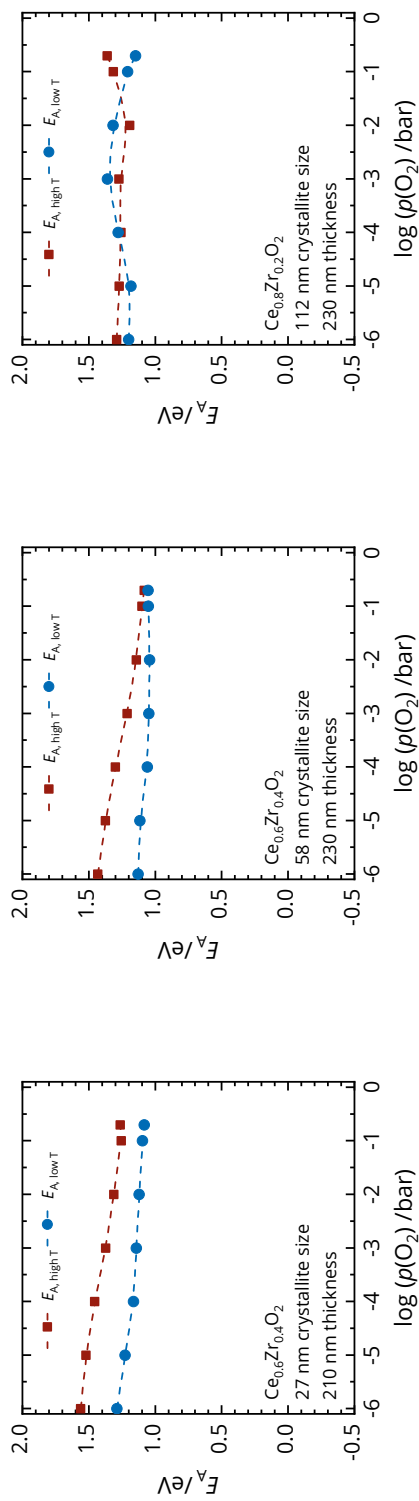


**Figure 4.26:** Comparison of the activation energies of  $\text{Ce}_{0.6}\text{Zr}_{0.4}\text{O}_2$  ceria thin films (6CZO) with increasing grain size from 27 – 112 nm and 210 – 230 nm thickness at different oxygen partial pressures. Dashed lines are for guidance only.

### Discussion of EIS measurements under dry conditions

Summarizing the results for the pure ceria samples (10CZO) it can be concluded that they do not show any slope in the  $\log \sigma$  vs.  $\log(pO_2)$  plot for the temperature and oxygen partial pressure range analyzed. This result can be understood by looking at the Brouwer diagram of Anti-Frenkel defect dominated pure ceria, introduced in section 2.1.

The total conductivity  $\sigma_{tot}$  is given by the sum of the oxygen vacancy conductivity  $\sigma_V$  and the electronic conductivity  $\sigma_e$ .

$$\sigma_{tot} = \sigma_V + \sigma_e \quad (47)$$

Combining equation (47) with the equilibrium constant  $K_{Red}$  for the cerium reduction

$$K_{red} = [V_O^{\bullet\bullet}]^2 \cdot n^4 \cdot pO_2 \quad (48)$$

and equation (13), relating the partial conductivity to the mobility of the respective charge carrier, one finds that the total conductivity is proportional to the vacancy concentration and the oxygen partial pressure:<sup>4</sup>

$$\sigma_{tot} \propto \mu_V [V_O^{\bullet\bullet}] + \mu_e \cdot pO_2^{-\frac{1}{4}} \quad (49)$$

Equation (49) shows that in materials with a high oxygen vacancy concentration the total conductivity is not a function of the oxygen partial pressure as  $\mu_V [V_O^{\bullet\bullet}] \gg \mu_e \cdot pO_2^{-\frac{1}{4}}$ , unless the mobility or concentration of the vacancies becomes very small due to lattice distortions for example. In the latter case the conductivity would exhibit a slope of  $-1/4$  in the double-logarithmic  $\sigma$  vs.  $pO_2$  plot. For pure ceria one would expect the electronic charge transport to be dominant in the intrinsic regime.<sup>27,171</sup>

What is to be expected from the defect chemistry of pure ceria described above is obviously not the case for the 10CZO samples in this work, as the slope in figure 4.17 and 4.18 in section 4.3.1 is zero. From this it can be concluded that the conductivity of the pure ceria thin films is mostly ionic and not electronic over the  $pO_2$  range investigated in this work. This is a notable result as it is in contrast to the predictions of the well established defect chemistry models, described above and in the theoretic section of this work. Interestingly, the same invariance of the ceria thin film conductivity to the oxygen partial pressure at moderate temperatures was also reported by several research groups in literature.<sup>2,21,27,172</sup> In these works it was concluded that very small acceptor dopant concentrations of a few 10 ppm are already sufficient to cause ceria to show ionically dominated charge transport. This

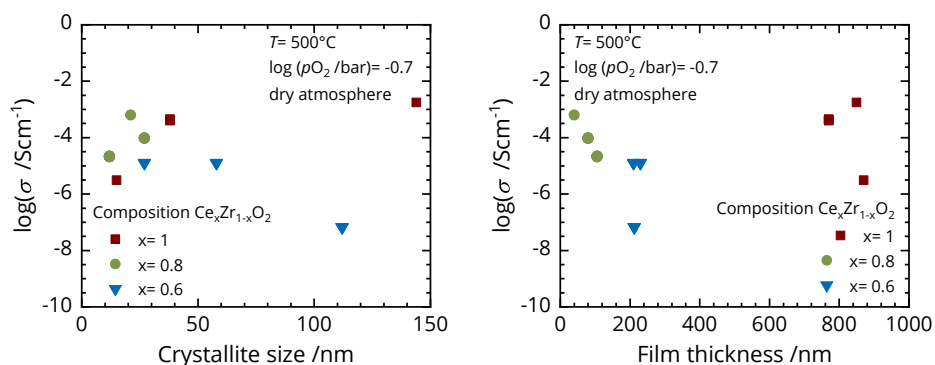


**Figure 4.27:** Plot of the conductivity as a function of grain size for the different compositions at approx.  $500^\circ\text{C}$  and an oxygen partial pressure of  $\log(p\text{O}_2 / \text{mbar}) = 0.7$ .

holds true especially at moderate temperatures as those applied in the present work. Higher temperatures at a given oxygen partial pressure correspond to more reducing conditions, causing the generation of more electrons, so that these become the major charge carriers. For moderate temperatures their concentration is not high enough to dominate the charge transport process.

The aforementioned conclusion is confirmed by the activation energies measured for the 10CZO thin films. They are in the range of 1.0 eV above  $400^\circ\text{C}$ , which is in accordance with literature values reported for an ionic transport process of oxygen vacancies the intrinsic regime ranging around 1 eV as well.<sup>21,172</sup>

In contrast to the pure 10CZO thin films the samples containing zirconium show a different behavior in the oxygen partial pressure range under investigation.

Comparing the absolute conductivity values of the thin films, one finds a relatively large scattering of the data. Especially the 6CZO sample with the largest average grain size shows a very low conductivity. In order to visualize the scattering of the absolute values, the conductivities of all samples discussed in this report is plotted in figure 4.27 for a given temperature and oxygen partial pressure as a function of their crystallite size, as well as their film thickness. A trend following the crystallite size would be an indicator for the grain boundary density to significantly influence the conductivity. For both thin film parameters no obvious trends are indicated by the graphs. Thus, no simple correlation between the thin films morphology and the measured conductivity perpendicular to the thin film surface can be deduced.

The reason for the scattering is not clear. Nevertheless, several possible explanations for this observation do apply. One possible reason is that the contact area between the electrode and the thin film is not as one would deduce from the geometry of the interdigital electrode

only. Depending on the frequency at which the impedance is measured and the platinum finger width, the active electrode area contributing to the charge transfer might change. This would change the electrode distance and thus the cell constant that is used to calculate the conductivity.<sup>165</sup> In addition the approximation used for estimating the cell constant in this work, does not take the contact area into account. This could also be different between the samples, or change during the measurements due to degradation of the electrode. As a consequence of the above mentioned effects, the true cell constant could deviate from that estimated by the method described in section 3.3.2 and equation (45). This would result in conductivities, determined for the different samples at different stages of the experiments, that are not comparable on an absolute scale. However, for the results shown in this manuscript it was made sure that the electrode was not significantly degraded, by checking its morphology after the EIS experiments. Some crystal growth within the platinum fingers was monitored, but the geometrical parameters were not significantly changed, nor could any evidence be found that the contact area between the thin film and the electrode changed during the EIS experiments.

Dewetting of the electrode was an issue during the experiments in this work, but no samples depicted in this report showed this kind of degradation of the electrode. Assuming that only differences in the cell constant are the reason for the huge deviations of the absolute values, the cell constant between the sample with the smallest conductivity of  $10^{-7.2} \text{ Scm}^{-1}$  ( $\approx 63.1 \text{ nScm}^{-1}$ ) and the sample with the highest conductivity of  $10^{-2.7} \text{ Scm}^{-1}$  ( $\approx 2.0 \text{ mScm}^{-1}$ ) at  $500^\circ\text{C}$  (see figure 4.27) would need to have changed by 4.5 orders of magnitude. This is of course only a very rough estimation, but still it becomes obvious that such huge differences cannot only be caused by a change of the contact area or quality.

Another possible explanation for a significant change of the contact area, and thus the cell constant, could be the roughness of the thin films below the interdigital electrode. Significant differences in the thin film roughness could possibly result in changes of the contact area between the film and the electrode and thus influence the true cell constant, as these effects are not taken into account by the simple estimation. This is generally a similar argument as the aforementioned, however the cause of the geometrically incorrect determined cell constant would be a different one. In order to exclude this aspect as well, the arithmetic roughness  $R_a$  values of the thin films, reflecting the arithmetical mean deviation of the assessed profile, were measured with a stylus profiler. For some samples an SPM measurement was conducted additionally. The determined roughnesses were in the same order of magnitude for all films investigated. Assuming that  $R_a$  is correlated with the surface contact area, this potential difference between the real cell constants and the estimated ones is not suited to describe

the huge difference of more than four orders of magnitude in the conductivity of the samples. Nevertheless, it could be part of the explanation for the deviation of those samples that only show small deviations of one to two orders of magnitude from each other. In order to study this in more details a dedicated experiment design would be necessary, aiming to reduce the variable set for possible conductivity deviations to geometrical factors only. Judging from the experiences made in the course of this work, that would be a very challenging task for the material class and geometry studied. For the present study the absolute conductivity values will not be correlated with any material parameters for the reasons given above. Nevertheless, the relative changes of the measured thin film conductivities as a function of the film morphology, as well as temperature and atmospheric conditions is suited to reveal interesting insights into the defect chemistry and conduction processes occurring in the samples under investigation.

As it is shown in figure 4.23 and 4.24 the conductivities of the 8CZO and 6CZO samples exhibit a similar response to a change of the oxygen partial pressure and thus the oxygen activity in the gas atmosphere around the samples for each composition. For the highest temperatures (550 °C) the slope of the double-logarithmic plot of the conductivity against the oxygen partial pressure is in the range of almost  $-1/6$ . In accordance with the defect model of aliovalently doped ceria, this slope is characteristic for electronic charge transport (small polaron hopping) in the extrinsic regime, as described in the theoretic part of this manuscript.<sup>12</sup> However, it is rather unlikely to have such a high reduction level in the high partial pressure range during the present experiments compared to other works, where electronic charge transport is typically observed at oxygen partial pressures as low as  $\log((pO_2)/\text{bar}) \approx -20$ , explaining a slope of  $-1/6$ .<sup>2,4</sup>

The explanation for the slope measured is more likely a different one described in the following. For the given conditions both, electrons and oxygen ions contribute to the overall conduction, formally given by the sum of the ionic and electronic partial conductivities (see equation (13)). The larger the contribution of electrons, the more the slope changes at a certain transition regime from 0 towards  $-1/4$ . For lower temperatures the ionic conductivity contribution (slope 0) dominates in a wider oxygen partial pressure range, causing the point of transition to shift towards lower partial pressures with decreasing temperature, as schematically shown by figure 4.28 on the following page. Thus, in the transition area between ionically ( $\sigma_i$ ) and electronically ( $\sigma_e$ ) dominated conductivity the slope changes from 0 to almost  $-1/6$ . With decreasing temperature the electron mobility and concentration in the material decreases as well. Therefore, a lower oxygen partial pressure is necessary to trigger the generation of enough electrons for dominating the overall conduction process. In this case it is very likely that the slope at higher temperatures as those that were applied in this

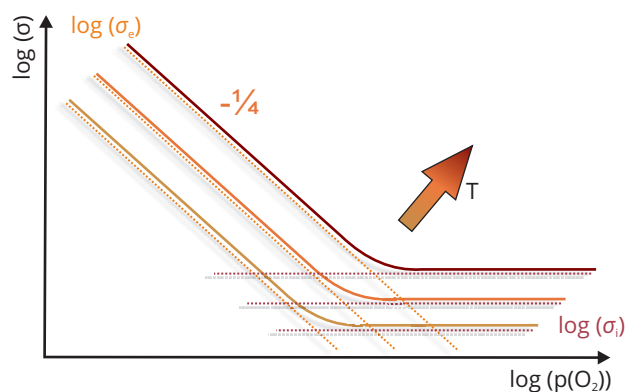


**Figure 4.28:** Schematic illustration of the superposition of ionic conductivity  $\sigma_i$  and electronic conductivity  $\sigma_e$  as a function of the partial pressure of oxygen in a double logarithmic plot. Adapted from the Master thesis of Raika Oppermann, during which the results on the 6CZO samples under dry conditions were obtained, under the supervision of the author of this work.

work becomes  $-1/4$ , which is what the defect model represented by the Brouwer-Diagramm in figure 2.3 predicts.

The fact that the power law exponent does not exhibit this value, but stays close to 0, even for the highest temperatures, can also be explained by the influence of the small crystallite sizes the thin films under investigation are composed of. As already described in chapter 2.2 on page 16, with decreasing grain size a transition between ionic and electronic conduction is obtained. As a consequence the exponent of the power law dependence between conductivity and oxygen partial pressure (see equation (20) and figure 2.6 on page 19) becomes smaller due to the enhanced electronic conduction in the space charge layers of the nanocrystalline thin films. The space charge layer model by Tschöpe et al. predicts that the  $pO_2$  dependence of the conductivity becomes weaker with decreasing grain size (see figure 2.6). This could also be a reason, why a slope of only  $-1/6$  instead of  $-1/4$  is observed.

The results in this work do not contradict this prediction. However, for the grain size range of the thin films investigated in this work a significant change of the exponent is predicted by the theory of the space charge layers. The 6CZO sample with the largest grain sizes shows an exponent of -0.08. Consequently following the theory of Tschöpe et al., the two samples with smaller crystallites should have exponents closer to 0, which is not the case (see figure 4.24). The overall grain size is too large to show a significant space charge effect as described by Tschöpe et al..

The most probable reason for the slopes flattening out with decreasing temperature is thus the transition from the electronic to the ionic conduction under the given conditions, as described in the former paragraph and schematically illustrated in figure 4.28.

Along with the reduction of the exponent the model by Tschöpe et al. predicts an increase of the activation energies for the conduction process with decreasing crystallite size. Tschöpe reports an activation energy for the charge transport of 1.7 eV for pure nanocrystalline ceria with a mean crystallite size of 21 nm, within a similar temperature range for one given oxygen partial pressure.<sup>95</sup> A trend of slightly increasing activation energies with decreasing grain sizes is also found for the samples in this work. On an absolute scale the activation energies determined for the 8CZO and 6CZO thin films in this work are slightly smaller (see figure 4.25 and 4.26) for the same oxygen partial pressure of  $10^{-4}$  bar as reported by Tschöpe. Further literature by Lee et al. on the electrical conductivity of the  $\text{CeO}_2$  -  $\text{ZrO}_2$  system contains similar values for the activation energy as in this work, but for a higher temperature regime.<sup>25</sup> The observation of two different activation energies in the temperature regime under investigation, as it was observed in this work (see figure 4.25 and 4.34 on page 93) was to the best of the authors knowledge not discussed in detail in literature reports on ceria-zirconia based thin film materials before. Chiodelli et al. reported the same change of activation energies in the temperature regime between 350 – 500 °C for sintered pellets CZO samples but did not discuss the reasons for this.<sup>61</sup> A possible explanation for this finding shall thus be proposed here.

At high  $p\text{O}_2$  the conductivity, and thus the observed activation energy, of the thin films is only determined by the oxygen vacancy migration enthalpy in the temperature regime under investigation. Thus only one activation energy, or only a small difference between the activation energy at low and high temperature is observed (see figure 4.25 and 4.26 on page 81). This activation energy being close to 1 eV is directly related to the migration enthalpy of the oxygen vacancies. Impurities like alkali earth metals or low-valent metal ions, like  $\text{Al}^{3+}$  or  $\text{Gd}^{3+}$  for example, cause acceptor doping of the thin films and thus increase the oxygen vacancy concentration in the intrinsic region, making these the dominant charge carriers. Increasing the temperature, oxygen is removed from the sample due to the more reducing conditions, leaving a vacancy and two electrons behind. Thus, there is an additional contribution due to the oxygen vacancy formation enthalpy (see equation 17) to the activation energy determined in the measurements, leading to an increase of the activation energy above 375 °C, in case of the samples investigated in this work. Therefore, figure 4.25 and 4.26 show a high and a low temperature regime activation energy. The low temperature activation energies only represent the migration enthalpy of oxygen vacancy migration, whilst the high temperature activation energies inhibit an additional contribution of the formation enthalpy for additional oxygen vacancies. More reducing conditions, being sufficient to reduce Zirconium doped ceria, due to its tendency to be reduced easier than pure ceria, cause the formation of additional vacancies.

Of course not only the temperature is important in this regard. In addition it can also be observed in figure 4.25 and 4.26, that the oxygen partial pressure has an influence. For most of the samples the high temperature activation energies increase with decreasing oxygen partial pressure, due to the additional contribution of the vacancy formation enthalpy to the overall activation energy determined in a more reducing environment. This effect is more pronounced the lower the oxygen partial pressure is. Chiodelli et al. also report that for higher temperatures at approximately 750 °C it is expected that the activation energy for zirconium doped ceria stays constant while it increases further for pure ceria.<sup>61</sup> During this work it was tried to conduct similar measurements. Unfortunately the dewetting of the platinum electrodes described in section 3.3.1 was too severe at temperatures above 550 °C, causing a loss of contact and/or a change in the cell constant during the impedance measurements. Nevertheless, the results extrapolated for higher temperatures are expected to be in line with those published by Chiodelli et al., who determined activation energies of 0.9 – 1.0 eV for the intrinsic and 1.5 – 1.6 eV for the extrinsic regime up to 1000 °C, depending on the sample composition of  $\text{Ce}_{1-x}\text{Zr}_x\text{O}_{2-\delta}$  sintered powder samples.<sup>61</sup>

Most of the literature results compared with the present data so far were measured on bulk samples. The measurements were done on sintered powder pellets of a few mm thickness. Two studies by Kosacki and Suzuki, worked with ceria based thin films instead, investigating the effect of different grain sizes and film thicknesses on the electronic conductivities.<sup>21,26</sup> They report that increasing film thickness and increasing grain sizes lead to increasing activation energies and thus decreasing conductivities at a given oxygen partial pressure. Both studies were conducted at higher temperatures. Comparing their results with our activation energies for the zirconia containing ceria thin films, the absolute values, as well as the trends for the activation energies with changing grain size and thin film thickness match.

Summarizing the discussion above, it can be concluded that unfortunately due to the scattering of the absolute conductivity values of the samples no trends that could be related to certain morphological parameters like the sample thickness, or the mean grain size were found. Nevertheless, the impedance measurements allow to get a detailed understanding of the defect chemistry of the thin films, and thus which charge carriers are dominating the transport in the columnar thin films perpendicular to the sample surface. The results obtained are in good agreement with those results already reported for ceria-zirconia samples in literature, proving that the experimental procedures and setups developed in this work are able to produce accurate results on this challenging sample system.

### 4.3.2 Measurements under humid atmosphere at elevated temperatures ( $200\text{ }^{\circ}\text{C} > T > 550\text{ }^{\circ}\text{C}$ )

After having investigated the samples under dry atmospheres, experiments under different degrees of humidification at a given oxygen partial pressure were conducted. For this, several tests were done in advance to study how the experiments need to be executed. It turned out that it is very difficult to work with decreasing humidities, as the time until the system reaches a steady state of the impedance response at a given water and oxygen partial pressure was very different from sample to sample. In addition it varied depending on the water partial pressure difference between two series of measurements. The more humid the atmosphere in the measurement setup was before going to a less humidified gas mixture, the longer it took to get into a steady state. After some further test measurements, it turned out that the most reliable way to measure under different humidities was to conduct temperature series just like under dry conditions and then subsequently increase the water partial pressure. Having reached the highest possible humidification, the measurement setup was flushed with dry gas for at least 24 h at  $400\text{ }^{\circ}\text{C}$  in order to prepare for the next temperature series with subsequently increasing water partial pressures.

The impedance spectra measured in humidified atmospheres did not show any qualitative differences compared to the spectra under dry conditions. In the high temperature regime the impedance spectra consist of three semicircles. With increasing resistances, thus decreasing temperatures the semicircles merge into each other, until only a single half semicircle is left for temperatures around  $< 350\text{ }^{\circ}\text{C}$  just like under dry conditions. This picture changes for very high humidities, larger than 80 rh%. Here three time constants are measured for the higher temperatures. Decreasing the temperature, the intermediate semicircle vanishes, leading to impedance spectra with two separable semicircles. This will be discussed in more detail later in this chapter.

Figure 4.29 shows the conductivities of the two ceria thin films (10CZO) determined from the impedance of the high frequency semicircle in humidified atmosphere with an oxygen partial pressure of 202 mbar. It can be seen that the conductivity for each temperature and water partial pressure is higher for the sample with 38 nm average grain size, just like for the measurements under dry conditions. In addition both samples show a certain slope of the conductivity as a function of  $p_{\text{H}_2\text{O}}$  for high temperatures. For lower temperatures  $< 300\text{ }^{\circ}\text{C}$  the slope tends towards zero. However, there seems to be some scattering in the data. Leaving the data points for the lowest water partial pressures out, one finds a slope of almost zero for all temperatures.

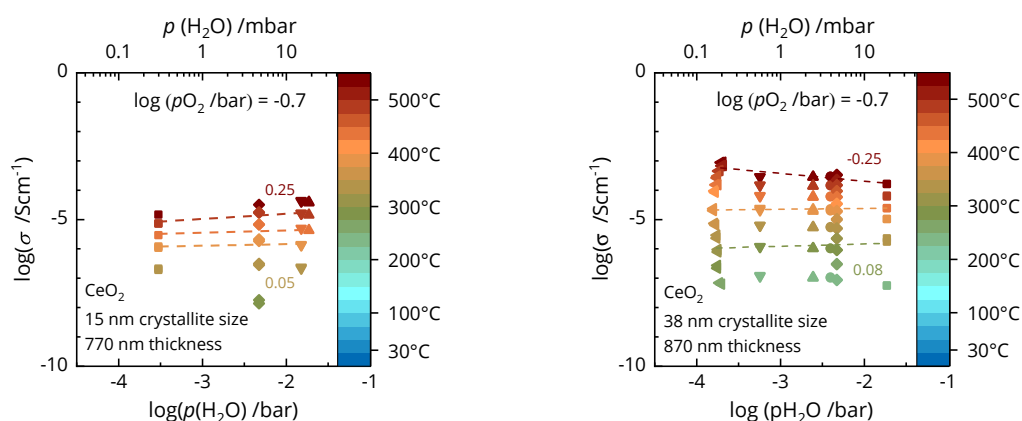


**Figure 4.29:** Comparison of the bulk conductivity of the ceria thin films (10CZO) with *left*) 15 nm grain size and 770 nm thickness and *right*) 38 nm grain size and 870 nm at different water partial pressures and different temperatures. Sample temperatures are given by the color scale. The dashed lines represent a linear fit of the data. For the highest and the lowest temperatures the value of the slopes are given in the respective color.

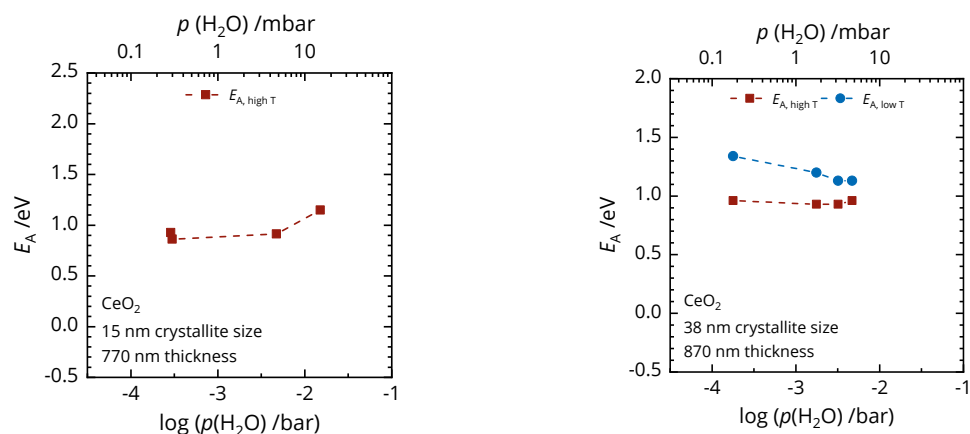


**Figure 4.30:** Comparison of the activation energies of  $\text{CeO}_2$  thin films (10CZO) with increasing grain size (15 – 38 nm) and thickness (770 nm – 880 nm) from left to right, at  $\log(p\text{O}_2 / \text{bar}) = -0.7$  and different water partial pressures, measured in the gas feed of the measurement setup at 25 °C. The dashed lines do not represent data points but are intended to give a guide to the eye.

The activation energies show a different behavior for each film (figure 4.30). For the film with the smaller average grain size, only a limited temperature range of the impedance data was evaluable, as it was also the case for the measurements under dry atmosphere. This results in the fact, that only one activation energy for the high temperature range could be determined. Compared to the activation energies determined without humidification of the gas atmosphere, the activation energies for the high temperature regime are in the same range for the 15 nm crystallites sample, whilst the thin film with larger grains shows slightly

larger activation energies, compared with the measurement under dry conditions (see figure 4.20 at  $\log(pO_2/\text{bar}) = -0.7$ )

The conductivities of the zirconium doped films as a function of water partial pressure and temperature are presented in figure 4.31 for the 8CZO thin films and in figure 4.32 for the 6CZO samples. It is observed that for these samples the water partial pressure has almost no influence on the samples conductivities. The slope for the conductivity as a function of intermediate humidities from 1 – 33% relative humidity ( $\approx 0.1 - 10$  mbar) is zero for all 8CZO and 6CZO samples under the given measurement conditions. The same result was also obtained for measurements conducted at a lower oxygen partial pressure (not shown here).

In addition to the conductivities the activation energies as a function of water partial pressures for the low (450 – 350 °C) and the high (550 – 450 °C) temperature regions were determined. The results are plotted in figure 4.33 and 4.34. Looking at the progression of the activation energies with changing water partial pressure, one finds that the differences between  $E_{A,\text{high T}}$  and  $E_{A,\text{low T}}$  are different for humidified conditions, compared to the differences in the activation energies determined for  $\log(pO_2/\text{bar}) = -0.7$  under dry conditions, which are shown in figures 4.25 and 4.26 on page 81. For example the 8CZO sample with 27 nm mean crystallite size (right plot in figure 4.25 and 4.33) exhibits activation energies that are similar for both temperature ranges ( $E_{A,\text{low T}}$  and  $E_{A,\text{high T}}$ ) under dry conditions at  $pO_2 = 202$  mbar, only deviating about 0.06 eV on an absolute scale. At the same oxygen partial pressure with only 1.2% relative humidity ( $\log(p(H_2O)/\text{bar}) = -3.5$ ) the difference in  $E_{A,\text{high T}}$  and  $E_{A,\text{low T}}$  is increased to 0.2 eV, continuously increasing with increasing water partial pressure. For the sample with slightly smaller crystallites of only 23 nm the difference of the activation energy in the low and high temperature region is in a similar regime, but exactly opposite regarding the two activation energies found, with  $E_{A,\text{low T}} > E_{A,\text{high T}}$ . The same trend for the activation energy differences between high and low temperature regime was also obtained for this sample in the  $E_A$  vs.  $\log pO_2$  plot (plot in the center of figure 4.25 on page 81). For the 8CZO thin film with the smallest crystallites (figure 4.25 on the left) the low and high temperature activation energies are almost equal. Comparing these results with the activation energies determined for the 6CZO thin films in figure 4.34 one finds that the absolute activation energy values are in a similar range. The activation energies of the 6CZO sample (figure 4.34, left plot) having the same crystallite size than the 8CZO film with the largest crystallites (figure 4.33, right plot) are in the same order of magnitude and show the same trend of  $E_{A,\text{high T}}$  increasing with water partial pressure. In case of the 6CZO sample this difference does not get as huge as for the 8CZO thin film. With increasing crystallite sizes for the 6CZO samples the difference between  $E_{A,\text{high T}}$  and  $E_{A,\text{low T}}$  increases

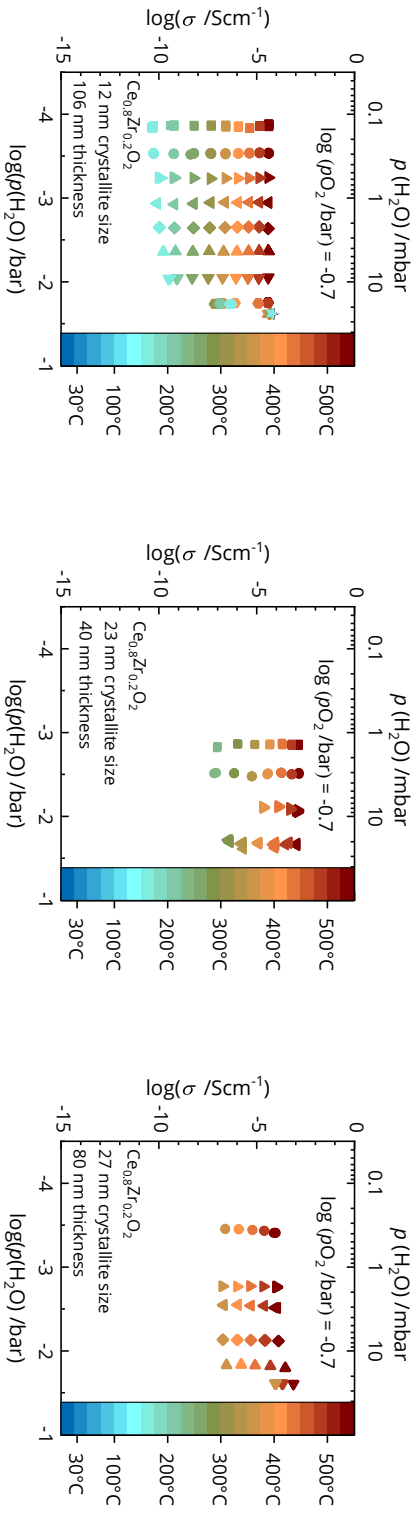


**Figure 4.31:** Comparison of the bulk conductivity of  $\text{Ce}_{0.8}\text{Zr}_{0.2}\text{O}_2$  thin films (8CZO) with increasing grain size from 10 – 27 nm and 40 – 106 nm thickness at  $\log(p\text{O}_2/\text{bar}) = -0.7$  and different water partial pressures measured in the gas feed of the measurement setup at 25 °C. Sample temperatures are given by the color scale.

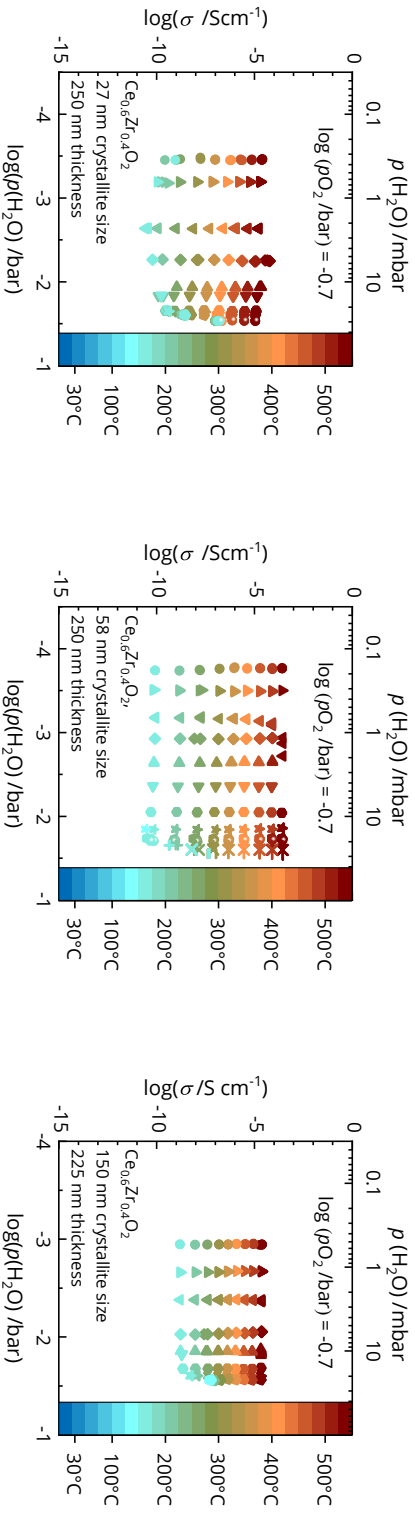


**Figure 4.32:** Comparison of the bulk conductivity of  $\text{Ce}_{0.6}\text{Zr}_{0.4}\text{O}_2$  thin films (6CZO) with increasing grain size from 27 – 150 nm and 225 – 250 nm thickness at  $\log(p\text{O}_2/\text{bar}) = -0.7$  and different water partial pressures measured in the gas feed of the measurement setup at 25 °C. Sample temperatures are given by the color scale.

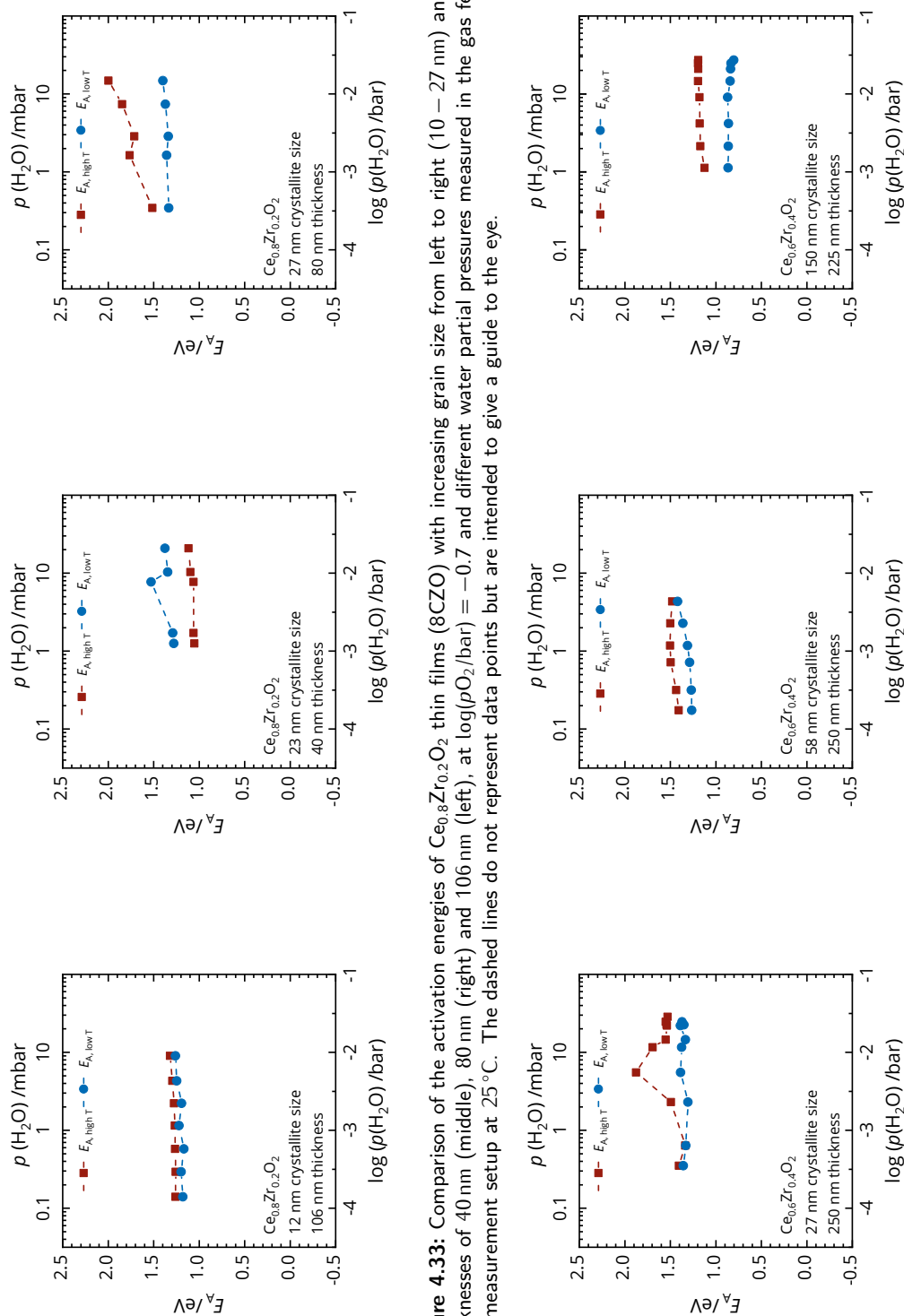


**Figure 4.33:** Comparison of the activation energies of  $\text{Ce}_{0.8}\text{Zr}_{0.2}\text{O}_2$  thin films (8CZO) with increasing grain size from left to right (10 – 27 nm) and film thicknesses of 40 nm (middle), 80 nm (right) and 106 nm (left), at  $\log(p_{\text{O}_2}/\text{bar}) = -0.7$  and different water partial pressures measured in the gas feed of the measurement setup at 25 °C. The dashed lines do not represent data points but are intended to give a guide to the eye.

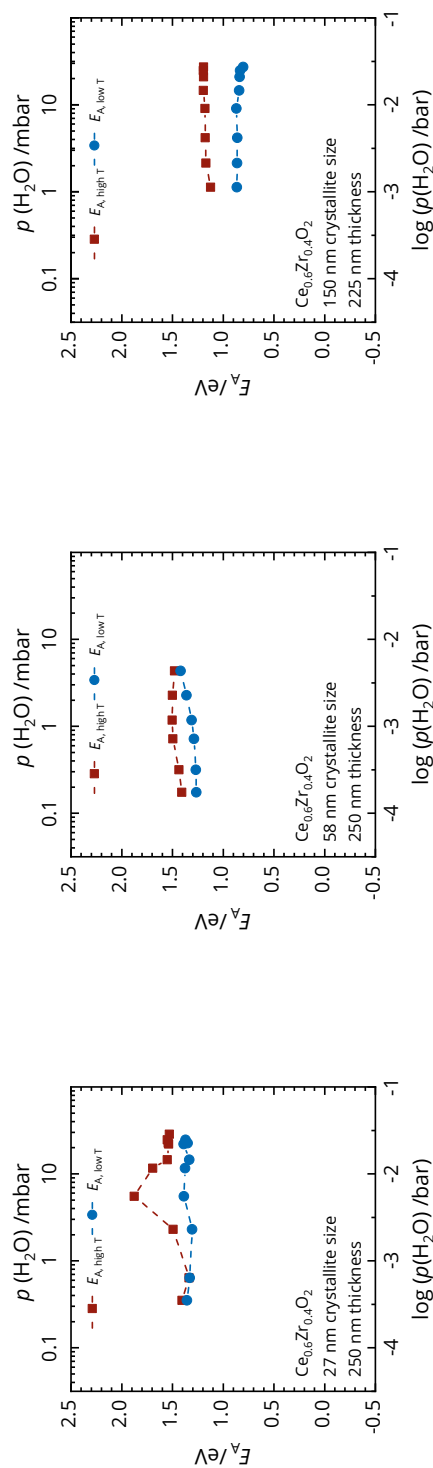


**Figure 4.34:** Comparison of the activation energies of  $\text{Ce}_{0.6}\text{Zr}_{0.4}\text{O}_2$  ceria thin films (6CZO) with increasing grain size from left to right (27 – 150 nm) and 225 nm (right) to 250 nm (left, middle) thickness at  $\log(p_{\text{O}_2}/\text{bar}) = -0.7$ , and different water partial pressures measured in the gas feed of the measurement setup at 25 °C. The dashed line does not represent data points but is intended to give a guide to the eye.

as well with increasing humidity.

For the pure ceria thin films in the temperature range from 250 – 550 °C the conductivity changes with the water partial pressure. This results in a slope in the double-logarithmic plots of the conductivity against the water partial pressure, of about  $+1/4$  for the 15 nm average grain size sample and  $-1/4$  for the 38 nm grain size sample, at the highest temperature of 550 °C measured (see figure figure 2.6). With decreasing temperature the slope tends towards zero, showing that the conductivity does not change with the water partial pressure anymore. This observation is quiet remarkable and in contrast to the behavior of the 8CZO and 6CZO samples shown in figure 4.31 and 4.32. Here the conductivity does not change with  $p_{H_2O}$  at all, except for very high water partial pressures, close to the saturation pressure of water. In order to interpret these results, it shall first be summarized what the expected result could be. Assuming that ceria incorporates protons in the bulk and take oxygen vacancies as the predominant positive defects into account, the dependence of proton concentration on water vapor pressure, which can be predicted from the proton incorporation reaction (equation (36)) given by several researchers in literature, is expected to show a power-law dependence of  $-\frac{1}{2}$ .<sup>38,57</sup> As already mentioned in the theoretical part of this work (see subsection 2.3.2) several results were published on ceria based materials under humidification. Oh et al. found an exponent of  $-\frac{3}{4}$  for undoped columnar porous ceria thin films for the  $\log \sigma$  vs.  $\log p_{H_2O}$ , while the same group (S. Haile) reports a decrease in conduction for acceptor doped microcrystalline ceria upon humidification.<sup>38,49</sup> Jimenez et al. did not systematically alter the water partial pressure, nor determined it precisely, but they report an increase of the conductivity in both humidified  $O_2$  and Ar, with a larger increase under lower oxygen partial pressure.<sup>57</sup> Based on two water partial pressure points only, their result roughly corresponds to a slope of  $-\frac{2}{5}$ , which is close to  $-\frac{1}{2}$ .

The water partial pressure was measured in the exhaust gases behind the oven in this work. Methodically it was not possible to measure it in the direct vicinity of the sample itself. Thus, it is possible that the water partial pressure is locally different at the sample, than at the point where the water partial pressure sensor was placed. Principally it is a reasonable assumption, that an incorrectly determined water partial pressure is the reason for this phenomenon. However, from the observations made for the 8CZO and 6CZO samples it is likely that the humidity does not have an influence on the conductivity at high temperatures. The opposite signs of the slopes in the 10CZO measurements is also pointing towards some kind of artifact being the reason for this observation rather than a physical meaningful effect. An additional hint is the fact that the experiments for the 10CZO samples shown here were conducted in an oven with a larger oven tube, than the experiments for the 8CZO and 6CZO samples. Taking the data points for the lowest water partial pressures out of the measure-

ment series in figure 4.29 one finds that the slope for the remaining data points becomes almost zero for all temperatures. This is an additional hint experimental problems for the lowest water partial pressure series led to this data. However, the reason of this different slopes for the 10CZO samples could not be revealed in the course of this project.

In order to pursue this phenomenon, more statistics would be needed on the conductivity of different 10CZO thin films as a function of the water partial pressure at  $\log(pO_2/\text{bar}) = -0.7$ . Unfortunately, these or different 10CZO samples were never measured in the new oven setup during this project, due to time constraints. Albeit that, the most likely reason is that this phenomenon is related to the measurement setup used for these two experiments. As the oxygen partial pressure was only actively monitored and controlled for the updated setup with the smaller sample oven, it could be a valid explanation, that the oxygen partial pressure during the measurements on the 10CZO sample under humidified conditions was not stable, causing a change in the conductivity.

In contrast to the 10CZO samples the results on the 8CZO and 6CZO samples measured in this project show a slope of 0 for the conductivity plotted against the water partial pressure. How can this behavior be understood?

As already mentioned in the theoretical section,  $[V_{\text{O}}^{\bullet\bullet}]$  is expected not to be fixed in the thin films, as they are not intentionally acceptor doped. Thus, the film conductivity is supposed to be a function of the equilibrium of these vacancies with the surrounding gas atmosphere (see Brouwer diagram in figure 2.3). However, the results obtained under dry conditions revealed that the thin films are unintentionally acceptor doped and thus the oxygen vacancy concentration is fixed in the intrinsic region, causing the conductivity to be constant for a  $pO_2$  of 200 mbar, as it was set during the water partial pressure dependent measurements shown here.

Water chemisorption (hydroxyl defect formation at the surface) consumes oxygen vacancies lowering their contribution to the overall conductivity.<sup>49</sup> In addition, water incorporation at the surface can also break associates of oxygen vacancies and electrons, according to Jimenez et al., making these electrons available to contribute to the conductivity of the material.<sup>57</sup> Thus, in humid atmosphere protons and electrons are expected to be the major charge carriers. Judging from the results in our case the electrons are higher in concentration and mobility, preventing the observation of proton conductivity at elevated temperatures. The fact that the conductivity for a given temperature (above 250 °C) is fixed for all 6CZO and 8CZO samples can be explained as follows. Only a limited number of vacancies is accessible for water molecules to adsorb, by the chemisorption type 2 mechanism schematically shown in figure 2.18, at a given  $pO_2$ . Thus, the conductivity related to the high frequency arc

of the impedance spectra is not altered significantly by the amount of water available in the surrounding atmosphere for elevated temperatures. This is a strong evidence that the bulk, assuming that its properties dominate the high frequency response of the electrochemical impedance spectroscopy experiments, is not influenced by water partial pressure. This behavior has also been reported for other similar systems. For example Pérez-Coll et al. reported that a dense gadolinium doped ceria ceramic did not change its high frequency arc conductivity under dry and wet oxygen, assigning this behavior to the dominant oxide ion conductivity.<sup>173</sup> A similar behavior is also reported by Shirpour et al. for pure and gadolinium doped microcrystalline ceria. They were actually able to analyze the grain boundary and bulk response separately, and did not find any influence of the water partial pressure under oxidizing conditions. For nanocrystalline samples an increase of the conductivity upon hydration already at temperatures as high as 400 °C is reported in the same publication. It is assigned to proton conduction along grain boundaries, which have an ideal geometry for the condensation of water in nanocrystalline ceria, leading to the formation of a conductive network even at relatively high temperatures already. In contrast to the presented results in this manuscript the results obtained by Shirpour were measured on compacted nano- powders that show more significant capillary effects, allowing the formation of a water network around the nano- powder granulates.<sup>58</sup> Judging from the obtained results this was not possible for the thin film samples in this work as they were dense, with grain boundaries in between the columnar crystals that were perpendicular to the field applied during the EIS measurements. At more moderate temperatures an interesting trend can be deduced from the data in figure 4.29, 4.31 and 4.32 showing the logarithmic conductivities plotted against the water partial pressures. An influence of adsorbing water at temperatures around 200 – 250 °C and high water partial pressures can be seen for the 8CZO and 6CZO samples, increasing their conductivity significantly. The same effect is not visible for the 10CZO samples. A possible explanation for this is, that 8CZO and 6CZO are easier reduced, due to their composition. Therefore, they exhibit more vacancies at the surface interacting with water molecules from the gas atmosphere. 8CZO and 6CZO samples already adsorb water on the surface at more elevated temperatures (or lower water partial pressures) than pure ceria thin films. Looking at the activation energies some differences in the slopes of the Arrhenius plots are found. For most of the samples the slope in the high temperature region, corresponding to  $E_{A,highT}$  in figure 4.33 and 4.34, is steeper as a function of the water partial pressure, than  $E_{A,lowT}$  in the low temperature regime, except for the 8CZO thin film with 23 nm average grain size. The absolute values correspond to what is reported in literature for the electronic transport processes related to ceria-zirconia samples under dry conditions.<sup>25,46,48,61</sup> Nevertheless, the values determined in this work cover a rather large range changing with water

partial pressure for a few samples, whilst staying almost constant for others. A clear trend, that would allow to deduce a certain influence of water (humidity in the atmosphere) on the charge transport process, is not given by the data measured. In this regard it would be interesting to study whether the thin film morphology or composition has an impact on how significantly the transport process is influenced by water adsorbing on the surface at elevated temperatures.

In conclusion, it can be stated that the impedance data at elevated temperatures are barely showing trends in between the samples that can be assigned to certain sample features like grain size or film thickness. It cannot be excluded that the high frequency response is purely that of the bulk material, although the capacity values are in the expected range and do not change with water partial pressure (not shown in this work). It could also be a mixture of bulk and grain boundary response. There is certain evidence of a second semicircle in the impedance spectra, that was unfortunately not separated well enough to be reliably fitted by the equivalent circuits tested in the course of this work. Further data evaluation approaches like the distribution of relaxation times analysis capable of working out additional features within the data are promising approaches, thinking of further research in this area.<sup>174,175</sup> It is very well possible that the huge amount of data evaluated during this research project holds more information than that what is represented by the relatively simple equivalent circuit model used here. More generally it can be concluded that the interaction with water in the gas atmosphere is influenced by the composition of the ceria-zirconia thin films. This is an interesting aspect thinking of possible sensor applications of mixed electronic ionic conductors in applications that combine high temperatures with the need to determine the humidity or the oxygen partial pressure.<sup>176</sup>

### 4.3.3 Measurements under humid atmosphere at low temperatures (30 °C > T > 200 °C)

In this work also the low temperature regime down to room temperature was investigated. For samples under dry atmosphere the results were scattering strongly as the impedance of the samples under test was almost too high to be measured (not shown). This observation changed completely, once the measurements were conducted under humidified conditions. Starting at a temperature of about 200 °C the impedance decreased to a measurable value even for rather dry conditions. Thus, as shown in figure 4.35 it was possible to measure the thin film conductivity over the whole temperature range between 30 – 550 °C starting at slightly increased humidities of the oven atmosphere. For all 8CZO and 6CZO samples the conductivities at temperatures between 30 °C and 200 °C were increased by several orders

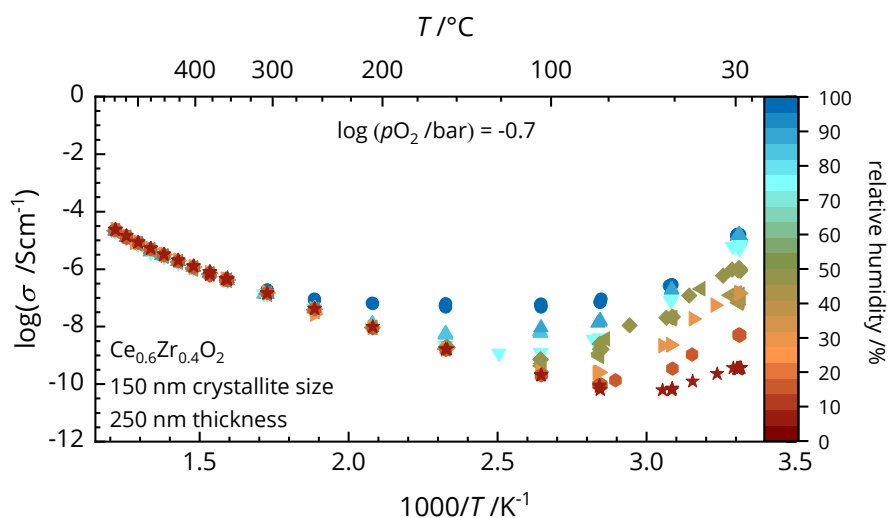


**Figure 4.35:** Bulk conductivity of a  $\text{Ce}_{0.6}\text{Zr}_{0.4}\text{O}_2$  thin film with 150 nm average grain size and 250 nm thickness as a function of inverse temperature at different atmosphere humidities between 4% and 98% shown by the color scale.

of magnitude with decreasing temperature and increasing water partial pressure. The higher the water partial pressure is set, the higher the temperature at which the conductivity begins to increase in each temperature series. Figure 4.36 exemplarily shows a Nyquist plot of a  $\text{Ce}_{0.8}\text{Zr}_{0.2}\text{O}_2$  thin film under humidified conditions and an oxygen partial pressure of about 200 mbar. The high and medium frequency semicircles are nicely resolved. Rather strong differences between the plots are found in the low frequency arc. This is nicely resolved for the measurement at 493 °C, whilst the impedance in the low temperature regime for the 31 °C measurement is so high, that only the first data points of this circle (not all of them are shown in figure 4.36) could be measured with the lowest excitation frequencies used in the impedance experiments. Figure 4.37 and 4.38 show a plot of the logarithmic conductivities as a function of the logarithmic water partial pressure for the temperature range between 30 – 200 °C for the 8CZO and 6CZO thin films. It is observed that the trends and absolute values for the conductivities are similar for all samples, independent of the thin film composition. The data is shown for different temperatures coded by the color of the symbols. For the lowest temperatures (30 °C) the conductivity increases step wise with increasing water partial pressure until it reaches the maximum value slightly above  $10^{-4} \text{ Scm}^{-1}$  for the 8CZO thin films. For the 6CZO films this value is one order of magnitude lower with only  $10^{-5} \text{ Scm}^{-1}$ . It can nicely be seen for each thin film that the onset of the conductivity increase happens at higher water partial pressure for higher temperatures.

Similar measurements as those for the 8CZO and 6CZO samples at low temperatures, were

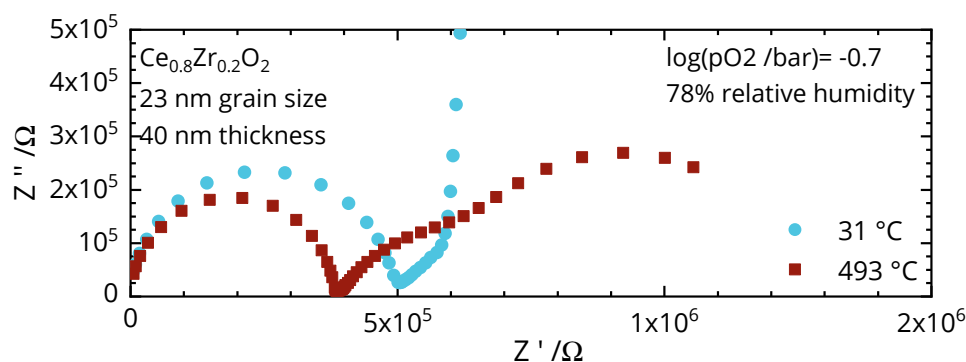


**Figure 4.36:** Nyquist plot of impedance measurements on a  $\text{Ce}_{0.8}\text{Zr}_{0.2}\text{O}_2$  thin film sample with 21 nm average grain size and 40 nm thickness at 493 °C and 31 °C under humidified conditions with 78% relative humidity in the gas atmosphere at 203 mbar oxygen partial pressure.

also done with 10CZO thin films in the early stages of experiments conducted in the course of this dissertation. These were done in an experimental setup with a significantly larger oven tube. This resulted in experimental data sets that were difficult to interpret, as the humidity sensor was placed behind the oven. Due to the large volume of the oven tube, the response of the humidity sensor to a change in humidity of the gas mixture at the sample was significantly delayed. The supplemental figure 6.2 in the appendix shows this effect. Plotting the thin film conductivity against the water partial pressure, calculated from the relative humidity, resulted in pairs of values that did not represent the actual conditions at the sample, although each data point on the relative humidity axis was measured several times. Thus, this data is not shown here. In order to correlate humidity and impedance data, significantly longer equilibration times would have been needed for each measurement point. This would have resulted in too long overall measurement times needed, in order to get data on the various thin films in a reasonable amount of time. Thus, it was decided to conduct further measurements in a different experimental setup with a significantly smaller tube, equipped with optimized gas circulation, resulting in less gas volume to be exchanged more efficiently when the desired atmosphere changes were applied with the gas flow controllers. Once the temperature is below a certain threshold temperature, physisorption of additional water layers occurs on the thin film surface, leading to a significant increase of the conductivity at high water partial pressures (see figure 4.31 and figure 4.32). The results for this region, where the temperatures are lowered down to almost room temperature are discussed in the following. The significant impedance decrease with increasing humidity for the high frequency arc at temperatures of 150 – 250 °C is most likely related to the formation of a physisorbed water

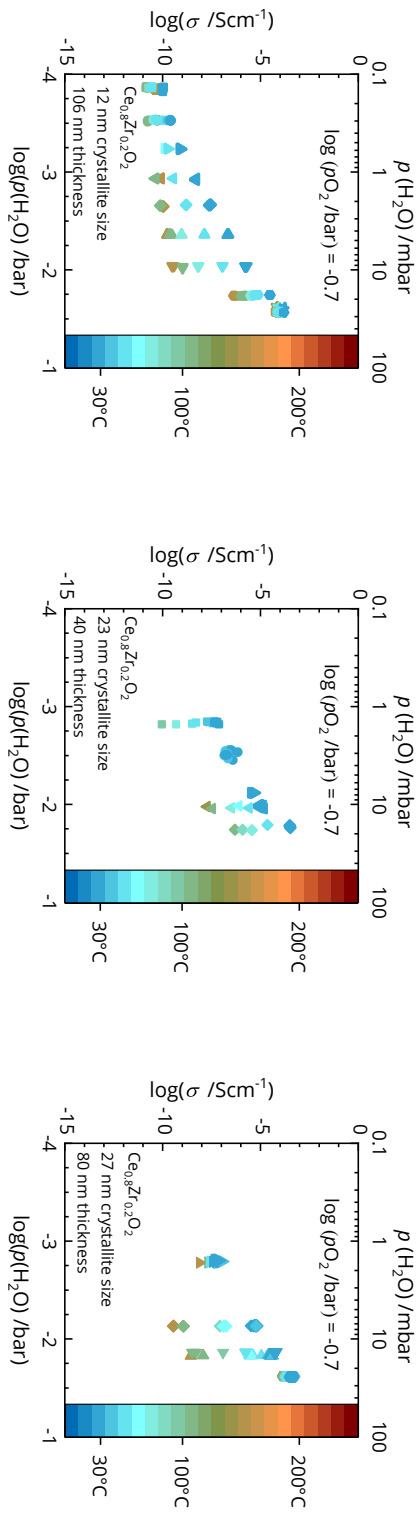


**Figure 4.37:** Comparison of the bulk conductivity of  $\text{Ce}_{0.8}\text{Zr}_{0.2}\text{O}_2$  thin films (8CZO) with increasing grain size from 10 – 27 nm and 40 – 106 nm thickness at  $\log(p\text{O}_2/\text{bar}) = -0.7$  and different water partial pressures measured in the gas feed of the measurement setup at 25°C.

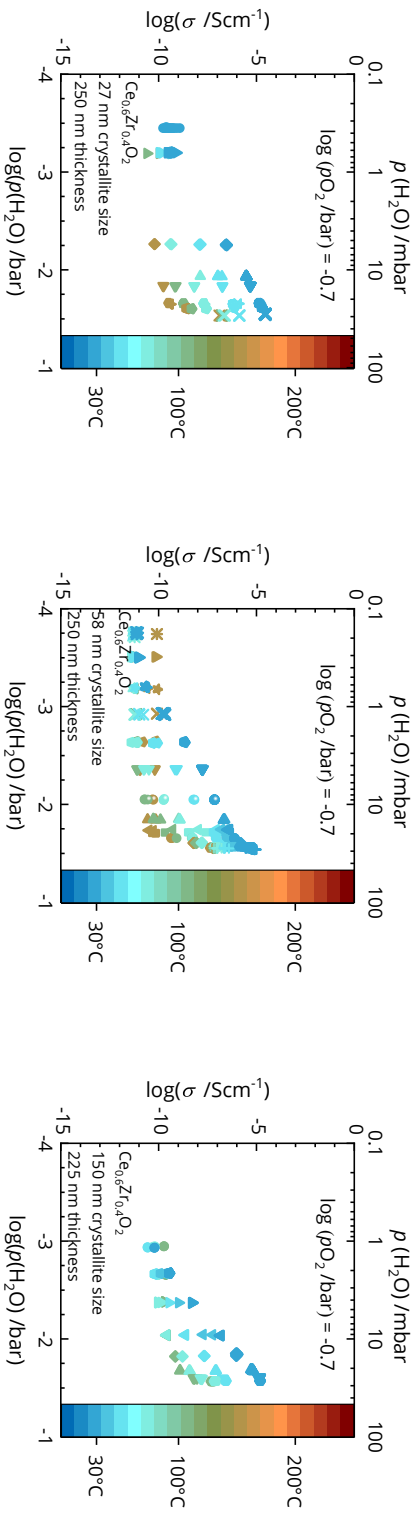


**Figure 4.38:** Comparison of the bulk conductivity of  $\text{Ce}_{0.6}\text{Zr}_{0.4}\text{O}_2$  thin films (6CZO) with increasing grain size from 27 – 150 nm and 225 – 250 nm thickness at  $\log(p\text{O}_2/\text{bar}) = -0.7$  and different water partial pressures measured in the gas feed of the measurement setup at 25°C.

layer, as described in subsection 2.3.1. A chemisorbed layer is formed at higher temperatures already, but at these temperatures charge carriers, namely hydronium ions in the water layer, are either not mobile enough or too low in concentration to contribute significantly to the measured conductivities. At intermediate temperatures (150 – 250 °C) it is likely that proton conduction occurs along the water molecules that are chemisorbed on the ceria surface under these conditions. This is indicated by the fact that the slope in the Arrhenius plot flattens, showing that the activation energies for the migration process is significantly lower than that reported for oxygen transport in nanocrystalline ceria, which is in the range of 0.8 – 1.5 eV.<sup>25,46,48</sup> As the temperature difference between the data points for the conducted experiments is relatively huge compared to the change in conductivity, the activation energies in this regime could not be precisely been determined by linear fitting of the Arrhenius plot, very likely undergoing a permanent change even within small temperature intervals. As soon as the temperature is lowered further a second water adsorption layer forms (type 2 mechanism, schematically shown in figure 2.18), in which hydronium ions can act as mobile charge carriers.<sup>42,43</sup> Below 100 °C, a physisorbed water layer forms on the ceria surface, resulting in the formation of a thicker water layer, allowing for an increased proton conduction. In this regime an apparent negative activation energy is observed in the Arrhenius plot against the water partial pressure of the gas feed into the oven. This is a result of the strong dependence of the amount of adsorbed water (and charge carriers) on temperature. This behaviour has also been reported for nano- metric zirconia thin films by Chiodelli et al..<sup>54</sup> In order to understand the achieved results better, it was intended to simulate the conductivities measured for the different samples on the basis of thermodynamic and kinetic assumptions. Therefore, a suitable model for the calculation needed to be established, taking into account thermodynamic values for the adsorption process, as well as the fact that water adsorption leads to the formation of a percolating network of water molecules on the surface as described in the theory section of this work (see subsection 2.4).

Equation (44) describes the conductivity of a thin film subsequently being covered with a water layer. Once a percolating conductive path for the protons is formed a significant increase in conduction occurs.<sup>125–129</sup> Thus, one can assume that the conductivity of the system reveals a power-law behavior, with an exponential proportionality to the water partial pressure in the surrounding atmosphere.

The coverage  $\theta$  is related to the water partial pressure. The easiest assumption here is that coverage and water partial pressure are linearly correlated with exponential factor  $s$  being close to unity.<sup>128</sup>

$$\theta \propto p(\text{H}_2\text{O})^s \quad (50)$$

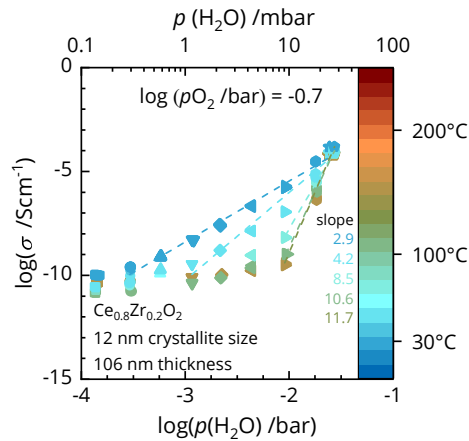


**Figure 4.39:** Doubly logarithmic plot of the conductivity against the water partial pressure of a 8CZO thin film with 12 nm crystallites at atmospheric oxygen partial pressure, showing the slopes of a linear fit of the data. The slope corresponds to the exponent  $m_s$  in equation (51).

Combining equation (44) and (50) results in the following proportionality:

$$\sigma \propto p(\text{H}_2\text{O})^{m_s} \quad (51)$$

Thus the exponent  $m_s$  can be found by determining the slope of the doubly logarithmic plot of the conductivity vs. the water partial pressure from figure 4.31 and 4.32. Looking at these figures it is obvious that the slope which can be determined strongly depends on the temperature, as exemplarily shown for the 8CZO thin film with the smallest crystallites in figure 4.39. The slopes that can be determined this way are given in table 4.2 for all 8CZO and 6CZO thin films. As it can be seen the exponents determined range from  $m_s = 2.9 - 22.6$ . The lowest values for  $m_s$  correspond to those determined for the measurements at 30 °C. The main reason for this large spread in the values is simply the fact, that the starting point for a linear fit for the different temperature series within the plots is difficult to be determined precisely. As the resolution on the  $p\text{H}_2\text{O}$  axis is not very high, it is difficult to determine exactly at which water partial pressure the conductivity increases for the different temperatures they were measured at. Thus a physical interpretation of these power law dependencies would probably be a little bit vague. Nevertheless, the values found for the exponent  $m_s$  from the conductivities determined at 30 °C are in the same range as those determined by Ahmad et al. for  $\text{Al}_2\text{O}_3/\text{NiO}$  nano composites under humid atmosphere.<sup>128</sup> In their work exponent values between 2.29 and 6.68 are reported. In order to introduce additional physicochemical parameters into the analysis of the measured data, a model combining a well established adsorption model, namely the BET isotherm (see section

**Table 4.2:** Slopes of the doubly logarithmic plot of the conductivity against the water partial pressure (see figure 4.37 and 4.38 of the thin films under investigation).

composition	crystallite size /nm	exponent <i>ms</i>	composition	crystallite size /nm	exponent <i>ms</i>
8CZO	12	2.9 - 11.7	6CZO	27	2.9 - 20.8
	23	3.2 - 5.8		58	3.2 - 19.4
	27	3.2 - 22.6		150	4.2 - 15.0

2.3.1 on page 21), with the concept of a percolating conductive network is proposed. Doing so the adsorption behaviour of water is considered in modeling the electric response of the sample under investigation.

The BET isotherm describes the adsorption behavior of a species from the gas phase to a solid surface. It can be used to describe the relative coverage  $\Theta_{\text{BET}}$  and thus be linked to percolation theory through the following relation, resulting from equation (33) and (44):

$$\sigma \propto (\Theta_{\text{BET}} - \Theta_{\text{C}})^m = \left( \frac{c \frac{p}{p_{\text{sat}}}}{\left(1 - \frac{p}{p_{\text{sat}}}\right) \cdot \left(1 - (1 - c) \frac{p}{p_{\text{sat}}}\right)} - \Theta_{\text{C}} \right)^m \quad (52)$$

As already described in section 2.4,  $\Theta_{\text{C}}$  is the critical coverage for percolation. The water partial pressure is  $p$ . The coefficient  $c$  represents the thermodynamic parameters and can be expressed by:

$$c = c_0 \exp \left( \frac{\Delta_{\text{ad}} H_1 - \Delta_{\text{cond}} H}{RT} \right) \quad (53)$$

The saturation partial pressure  $p_{\text{sat}}$  of the absorbent at the respective temperature  $T$  is derived using the IAPWS<sup>i)</sup> formulation converted to ITS-90<sup>ii)</sup> temperatures by Wagner and Pruß.<sup>178</sup> It is given by several coefficients, linking the saturation pressure to the given temperature as well as the critical temperature. It can thus be calculated for any given temperature in order to be used in the model. For further details on this the reader is referred to the publication by Wagner and Pruß.<sup>178</sup> Combining equation (52) and (53) a proportionality constant representing the conductivity of a full water layer has to be introduced along with a constant offset  $\sigma_{\text{min}}$  accounting for the conductivity (conductance  $G_{\text{min}}$ ) of the thin film without a water layer, preventing that the conductivity at zero coverage becomes zero as well. This offset is not necessarily the conductivity of the thin film without water coverage. It can also be the minimal conductivity that can be measured with the equipment used.

<sup>i)</sup>IAPWS: International Association for the Properties of Water and Steam

<sup>ii)</sup>ITS-90: International temperature scale of 1990<sup>177</sup>

Including this results in the terms:

$$\sigma_{\text{BET}} = \sigma_{\text{min}} + \sigma_0(\Theta_{\text{BET}} - \Theta_{\text{C}})^m \quad (54)$$

$$G_{\text{BET}} = G_{\text{min}} + G_0(\Theta_{\text{BET}} - \Theta_{\text{C}})^m \quad (55)$$

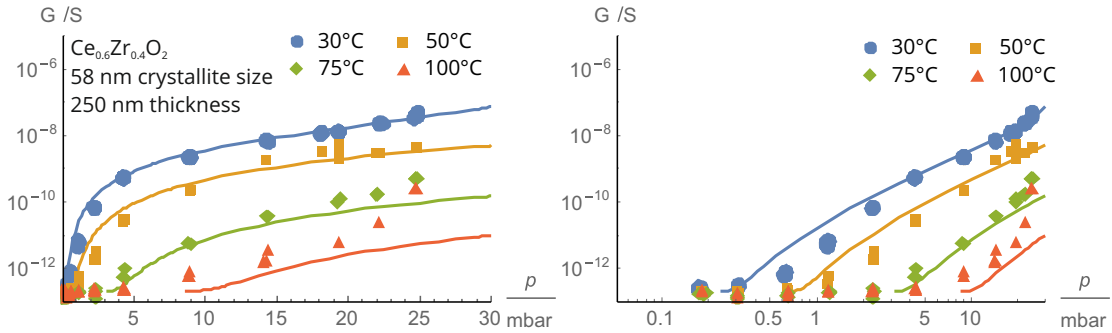
Thus,  $\sigma_{\text{BET}}$  or the conductance  $G_{\text{BET}}$  is a function of the difference between the first layer adsorption  $\Delta_{\text{ad}}H_1$  and condensation enthalpy  $\Delta_{\text{cond}}H$  of water on the thin films, which is influenced by the surface properties of the samples. Further  $\sigma_{\text{BET}}$  depends on the given temperature, the water partial pressure as well as the percolation coefficient  $m$ . The adsorption and condensation enthalpies depend on the surface the water molecules interact with.

In the present experiments an increase of the conductivity at intermediate temperatures between 100 – 250 °C (see results in section 4.3.3) due to the formation of a chemisorbed water layer, in which conduction takes place by a Grotthuss mechanism, is found.<sup>116</sup> If the temperatures are decreased further, a physisorption layer forms at the surface on top of the chemisorbed layer in which conduction takes place by a vehicle based mechanism.<sup>179</sup>

Although this effect is described in literature for several systems, a quantitative model for the description for the conductivity increase is not given to the best of the authors knowledge. Thus, the model described above is applied to the results in this work. For this purpose a Mathematica based fitting tool was programmed, in order to be able to manipulate the different parameters of equation (52) - (55) interactively.<sup>180</sup> Together with the thermodynamic values for the difference between the adsorption enthalpies for the first physisorbed layer  $\Delta_{\text{ad}}H_1$  and the condensation enthalpy  $\Delta_{\text{cond}}H$ , the computer model allows to simulate the measured conductance as a function of water partial pressure. For the simulated conductivity shown in figure 4.40 the fitting parameters in table 4.3 were used. The Mathematica software package was used due to the sophisticated dynamic calculation capabilities.<sup>180</sup> With reasonable coding effort the interactive manipulation of the single fitting parameters by simple sliders using the `Manipulate` function is made possible. This allows to conveniently get a good impression how the resulting graphs, derived from the rather complex mathematical relation in (52) - (55), change for all temperatures at once when a certain value is varied. A similar tool as the `Manipulate` function allowing to program a graphical user interface is certainly also implemented in other programs for such fitting tasks. However, the performance and usability, even with limited programming effort and skills, of Mathematica in this regard is remarkable. Using the features in Mathematica described above, it was possible to find reasonable fitting parameters, given in table 4.3 for the results obtained for a 6CZO sample with 58 nm crystallite size. This demonstrates that the relatively large parameter space in the model was significantly reduced by linking the results for several temperatures. Taking

**Table 4.3:** Simulation parameters for 6CZO sample with 58 nm crystallite size.

$T_1/K$	$\Delta T_2/K$	$\Delta T_3/K$	$\Delta T_4/K$	$c_0$	$m$	$\Theta_C$
305	17	50	75	1	2.3	0.02
$\Delta_{ad}H_1 / \text{kJ mol}^{-1}$	$\Delta_{cond}H / \text{kJ mol}^{-1}$	$G_{min} / S$	$G_0 / S$			
47.5	44.0	$2.3 \cdot 10^{-13}$	$1 \cdot 10^{-8}$			

**Figure 4.40:** Simulation of the low temperature conductance of a 6CZO thin film with 58 nm grain size with the water partial pressure axis scaled linear (left) and logarithmic (right). The solid lines represent the simulated data from equation (54). The data points are the same as those shown in figure 4.38.

this into account the simulation results obtained show a good qualitative and quantitative agreement with the experimental measurements. It can be seen that the match between the model and the experimental results, becomes less accurate for higher temperatures. Here the conductivity values measured for high water partial pressures show a further increase that is not described by the model. In order to check whether this differences result from the relatively harsh restriction of one set of parameters for the four different temperatures, the fit model was transferred from Mathematica to Origin, in order to allow for fitting each series of measurements with individual temperatures, using the starting conditions obtained with the Mathematica routine.<sup>144</sup> The results of individual fitting steps of the data by a classical least mean squares method (Levenberg-Marquardt algorithm) is shown in figure 4.41. The respective results of the fitting process are given in table 4.4. Using this more automated fit routines, the results for the fitted curves are quiet accurate showing reasonable coefficients of determination ( $R^2$ ). The data is described more precisely than by the semiautomatic method used in Mathematica. Nevertheless, the second increase of the conductivity at high water partial pressures for the 75 °C or 100 °C series could not be simulated with an individual set of parameters, nor with the more simplified fit in Mathematica. The fitting routine itself turned out not to be very stable regarding variations of single parameters. This manifested in the fact that even for the dataset with the most experimental data points available, the

**Table 4.4:** Simulation parameters for 6CZO sample with 58 nm crystallite size. Parameters that show an uncertainty of  $\pm 0$  were fixed in order to reduce the degree of freedom of the fitting model.

$T / ^\circ\text{C}$	$28 \pm 0$	$51 \pm 0$	$78 \pm 0$	$105 \pm 0$
$\Delta_{\text{ad}}H_1 / \text{J mol}^{-1}$	$48490 \pm 1650$	$47800 \pm 2087$	$47243 \pm 4283$	$49837 \pm 3621$
$\Delta_{\text{cond}}H / \text{J mol}^{-1}$	$44000 \pm 0$	$44000 \pm 0$	$44000 \pm 0$	$44000 \pm 0$
$G_0 / \text{S}$	$3.4 \times 10^{-9} \pm 2.4 \times 10^{-9}$	$1.9 \times 10^{-8} \pm 2.6 \times 10^{-8}$	$1.5 \times 10^{-7} \pm 5.9 \times 10^{-7}$	$2.6 \times 10^{-8} \pm 8.3 \times 10^{-8}$
$G_{\text{min}} / \text{S}$	$2.2 \times 10^{-13} \pm 1.3 \times 10^{-13}$	$2.0 \times 10^{-13} \pm 1.3 \times 10^{-13}$	$2.5 \times 10^{-13} \pm 2.0 \times 10^{-13}$	$3.6 \times 10^{-13} \pm 1.7 \times 10^{-13}$
$m$	$2.9 \pm 0.5$	$3 \pm 0.001$	$3 \pm 0.001$	$3 \pm 0.003$
$\theta_C$	$0.027 \pm 3.3 \times 10^{-6}$	$0.016 \pm 0.03$	$0.011 \pm 0.015$	$0.022 \pm 0.023$
$R^2$	0.996	0.988	0.964	0.932

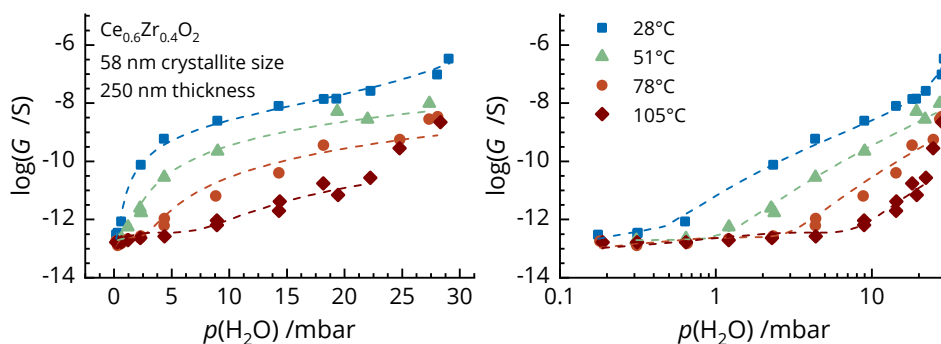


**Figure 4.41:** Individual simulation for each temperature series of the low temperature conductance of a 6CZO thin film with 58 nm grain size with the water partial pressure axis scaled linear (left) and logarithmic (right). The dashed lines represent the simulated data from equation (54). The data points are the same as those shown in figure 4.38.

fitting algorithm found several local minima with fitting parameters that were physically not meaningful. The main reason for this is that the mathematical parameter space given by the model is too huge for the limited amount of data available. This results in a elevated probability to find local minima in the parameter space, as observed during the fitting process with Origin. In order to reduce the degree of freedom for the model, it was decided to fix certain parameters based on the experiences made with the Mathematica “hands on approach” before. These can be identified in table 4.4, as they have a fitting uncertainty value equal to “0”.

Comparing the results of the Mathematica semiautomatic fitting approach and the automated routines used in Origin, it is found that several parameters are in the same range. The difference between the first layer adsorption  $\Delta_{\text{ad}}H_1$  and condensation enthalpy  $\Delta_{\text{cond}}H$  determines the shape of the simulated curves significantly. The absolute values are not important as long as the difference between them is the same. Using the Mathematica routine

the optimum difference to describe the experimental data is found to be  $3.5 \text{ kJ mol}^{-1}$ . Similar values are determined by the automated fitting routines in Origin. These differences are in the same order of magnitude than those reported for other water adsorption processes.<sup>44,111,181</sup> In theoretical works it is found by density-functional theory (DFT), as well as ab initio calculations, that the adsorption energy of water on a (111) ceria surface is only slightly influenced by the coverage.<sup>44,181</sup> Transferring this to the findings in this work, it can be concluded which the electrical response can be described by modeling the adsorption of a water multilayer on a ceria surface that is already terminated by chemisorbed hydroxyl groups.

According to literature the experimentally determined adsorption enthalpy of water on ceria is in the range of  $-\Delta_{\text{ad}}H = 48.6 \text{ kJ/mol} - 61.7 \text{ kJ/mol}$ , being in good agreement with the enthalpies determined here, taking the fact into account that it is strongly depending on several environmental factors (temperature, pressure, gas mixture) as well as the surface properties and morphologies of the adsorbent.<sup>59,113,182,183</sup>

The critical coverage value  $\Theta_c$  is found to be quite small for all fitted samples with relatively huge uncertainties, except for the lowest temperature series fitted for each sample. The higher the critical coverage is set using the manual Mathematica routine, the higher the  $p\text{H}_2\text{O}$  value for which a conductance parameter can still be calculated, as otherwise the discriminator in equation (52) becomes negative, resulting in physically not meaningful results for the conductance calculated. A possible explanation for this observation is that there are already chemisorbed hydroxyl groups present on the sample surface, lowering the temperatures below  $150^\circ\text{C}$ . Thus, only a small extra coverage by water molecules is necessary to form a conductive water layer path explaining the low critical coverage observed. This is in accordance with the findings of Ahmad et al.. They studied  $\text{NiO}/\text{Al}_2\text{O}_3$  nano-composites, and applied percolation theory to explain the measured conductivities at increasing humidity.<sup>128</sup> In their work they also found that conductive paths are formed at low relative humidities. Interestingly, the value  $G_0$  is showing a rather strong increase with temperature for all 6CZO samples investigated. This parameter phenomenologically describes the highest possible conductance of the water thin film at full coverage. The conductivity corresponding to this conductance should thus be similar to that of pure water, if the assumption is correct that it describes a water layer. The conductance of the water layer at  $28^\circ\text{C}$  in table 4.4 corresponds to a water film conductivity of  $0.10 \pm 0.07 \mu\text{S/cm}$  to  $1.56 \pm 0.057 \mu\text{S/cm}$  for the samples under investigation. This is in reasonable agreement with values for pure water conductivity at  $30^\circ\text{C}$  of  $0.05 \mu\text{S/cm}$  reported by the ASTM International, taking into account that even slight surface contaminations on the CZO films could change the conductivity of the water layer drastically.<sup>184</sup>

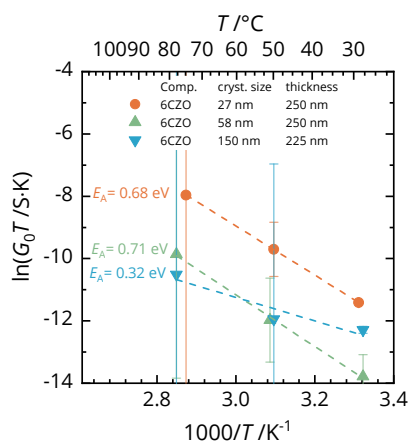


**Figure 4.42:** Arrhenius plot for the conductance of a water film at 100 % coverage  $G_0$  determined using the fitting routine described in the former paragraph.

The conductance  $G_0$  of the water layers is a function of the charge carrier concentration and their mobility, which is a function of temperature. The charge transport mechanism of a proton carrying a charge hopping from a hydronium ion to a neutrally charged water molecule (Grotthuss mechanism), can be described as an activated hopping process, similar to that of the charge carriers in the CZO films as well. The fact that the conductance of the water films increases with temperature is physically reasonable as the mobility of the charge carriers in the water thin films is supposed to increase with temperature. However, an increase over almost two orders of magnitude seems relatively huge. Figure 4.42 shows an Arrhenius plot for the conductance  $G_0$  of a water film at 100 % coverage in a temperature range from 30 – 80 °C, from which the activation energies for the charge carrier transport in the water layer can be deduced. The activation energies determined range from 0.32 eV to 0.71 eV. The fact that the activation energies are in a comparably high range compared to what is expected for bulk water (approx. 0.1 eV) indicates a rather strong binding of water molecules to the ceria surface, as it would be the case for water chemisorbed to oxygen vacancies in the ceria surface or ice-like water films. At the same time the error bars in graph 4.42 show that this analysis has huge uncertainties due to the huge fitting uncertainties in  $G_0$ . Nevertheless, more data points than those determined and presented in this work will be required to get more significant meaning and insight into this aspect. The trend given by this few data points taken strengthens the validity of the fitting model used to describe the measured conductivity data in the low temperature region. Ultimately, the exponential temperature behaviour could also be included in the fitting model routines in order to compensate for the over-determination of the model by introducing constraints for the parameters in the system.

One could assume that the protonic transport changes from a Grotthuss type mechanism at lower relative humidities to a vehicular transport mechanism at higher relative humidities. The activation energy becomes smaller with increasing humidity as the the water layer structure changes from a relatively strongly bound ice-like structure into a more loosely bound liquid structure. However, the amount of data points in figure 4.42 to proof or falsify this statement is not sufficient.

In order to address this, a different evaluation of the conductivity data is described in the following. Figure 4.35 shows the Arrhenius plot of a 6CZO thin film for different relative humidities of the gas feed into the oven in which the sample was measured. In order to determine the activation energies of the conduction mechanism in the water thin films from this particular data, one is interested in a  $\ln(\sigma T)$  vs.  $1/T$  plot for a constant water partial pressure at the sample. As the water partial pressure in the oven is unknown, but at the same time a function of the temperature, these data points of interest were not directly measured but can be determined mathematically.

For a certain relative humidity it can be calculated at which temperature the humidity value of another measurement series at higher relative humidities is the same as for the series with lower humidities. This is possible as the absolute humidity in the oven can be assumed to be constant. Using the following equation the relative humidity as a function of temperature  $RH_T$  can be determined.

$$RH_T = \frac{AH_{\text{feed}} \cdot R \cdot T}{p_{s,T} \cdot M_{H_2O}} \quad (56)$$

$AH_{\text{feed}}$  is the absolute humidity of the gas feed into the oven,  $R$  is the gas constant,  $M_{H_2O}$  is the molar mass of water and  $p_{s,T}$  is the saturation partial pressure of water at a given temperature  $T$ . The latter can be determined using the IAPWS formulation described above already.<sup>178</sup> If the relative humidity  $RH_T$  at a certain temperature is equal to that at lower temperature one wants to determine, this particular temperature of equal relative humidity is used to determine the respective  $\ln(\sigma T)$  value from the Arrhenius plot. If this is done for all measurement series of different relative humidities the data points represented by the open symbols in figure 4.43 are the result. These values allow to determine the activation energy of the water charge transport process in the respective temperature regime.

The described data analysis was applied to all 8CZO and 6CZO thin films. All samples show an increase of the activation energy at elevated temperatures. For the 8CZO samples with 12 nm and 27 nm crystallite size this effect is most pronounced. The activation energies shown in the graphs in figure 4.44 and 4.45 were determined for the data points at temperatures below those where the activation energy increases. For all samples and relative

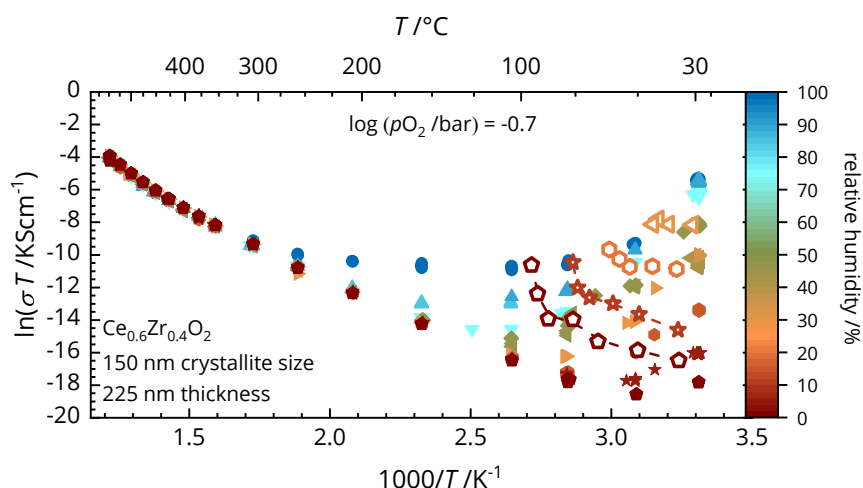


**Figure 4.43:** Bulk conductivity of a  $\text{Ce}_{0.6}\text{Zr}_{0.4}\text{O}_2$  thin film with 150 nm average grain size and 250 nm thickness as a function of inverse temperature at different atmosphere humidities. In addition the data points at those equivalent temperatures that correspond to the relative humidity of the respective relative humidity at 30°C (same symbol shape and color code with open symbols) for each measurement series are plotted.

humidities they are within the same range as those Stub et al. determined for the protonic transport processes in porous bulk YSZ samples.<sup>185</sup> It can be seen that these activation energies decrease with increasing relative humidity for the 6CZO samples. The same is reported by Stub et al. as well. This finding would confirm the assumption of a change in the charge transport mechanism within the water layer. Unfortunately, for the 8CZO samples no unambiguous trend is visible. However, the temperature dependency under fixed relative humidities cannot be ascribed to the enthalpies of defect formation and mobility of the protonic charge carriers in the water thin film only.<sup>185</sup> With increasing relative humidity above the 6CZO thin films the enthalpy for charge carrier formation decreases or the mobility increases (or both). Based on the experiments conducted in this work it is not possible to distinguish the influence of these two effects. In order to study this in more detail the measurements presented here could be repeated with deuterated water which should have an impact on the mobility in the Grotthuss type conduction mechanism regime.

#### **On the influence of grain sizes and thus grain boundaries on the conductivity in humid conditions**

In the following, the influence of the grain sizes and morphology of the underlying thin films on the measured conductivity shall be addressed as one of the main questions that motivated this research project. The BET and percolation model fitting routine presented above was applied to all 8CZO and 6CZO data sets available. Unfortunately, it turns out

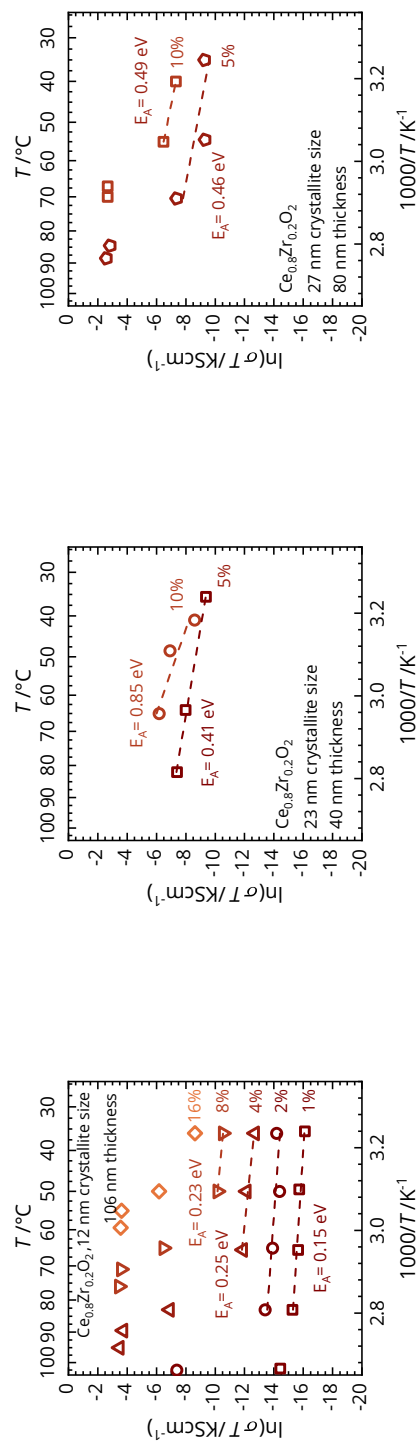


**Figure 4.44:** Comparison of the activation energies determined for the water layers forming on the  $\text{Ce}_{0.8}\text{Zr}_{0.2}\text{O}_2$  thin films (8CZO) with increasing grain size from 10 – 27 nm and 40 – 106 nm thickness at  $\log(p\text{O}_2/\text{bar}) = -0.7$ . The activation energies were determined by calculating the temperatures for equal relative humidities in the oven compared to those in the gas feed (given in percentage values in the graphs) as described in this paragraph.

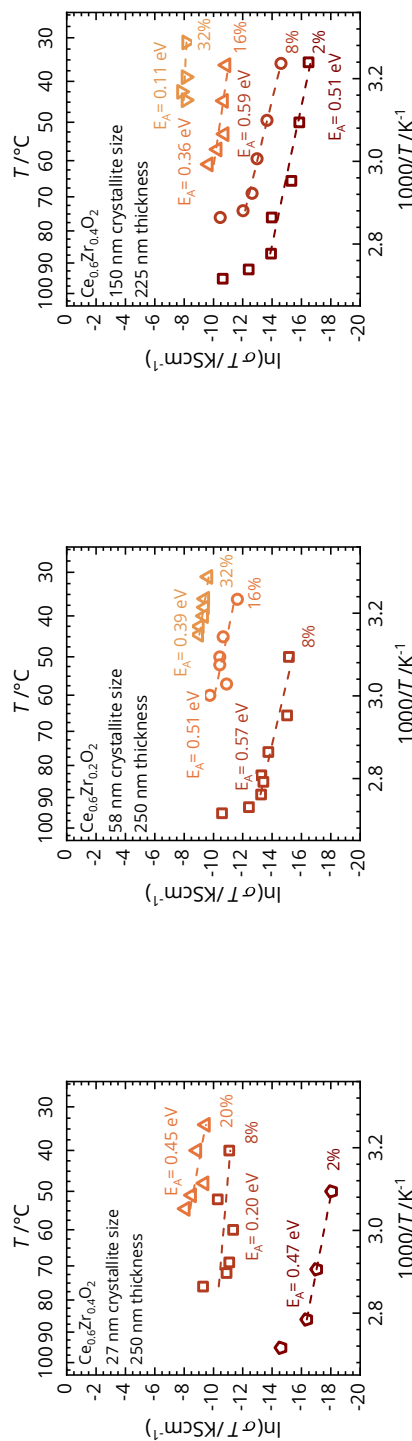


**Figure 4.45:** Comparison of the activation energies determined for the water layers forming on the  $\text{Ce}_{0.6}\text{Zr}_{0.4}\text{O}_2$  thin films (6CZO) with increasing grain size from 27 – 150 nm and 225 – 250 nm thickness at  $\log(p\text{O}_2/\text{bar}) = -0.7$ . The activation energies were determined by calculating the temperatures for equal relative humidities in the oven compared to those in the gas feed (given in percentage values in the graphs) as described in this paragraph.

that the data point density for two of the three 8CZO films (23 nm and 27 nm crystallite size) is not high enough to obtain reliable results. As already assumed by the visual comparison of the results in figures 4.37 and 4.38, the differences between the samples are small compared to the uncertainty of the method. No trends are deducible showing a dependence of the measured conductance of the thin film to any thermodynamic value, and thus allow a deduction of the adsorption behavior of water on the thin films as a function of their morphology or composition. In order to visualize this even better, the conductivities as a function of the water partial pressure are plotted in figure 4.46 and 4.47. It can be seen that irrespective of the grain size for the 8CZO and 6CZO thin films, the conductivity is the same for a certain grain size at each temperature between 50 – 100 °C. From this it can be deduced that the grain boundary density in the thin film under investigation does not have an influence on the conductivities measured at low temperatures.

The results confirm that on dense nanocrystalline  $\text{Ce}_{1-x}\text{Zr}_x\text{O}_2$  thin films in a humid environment the conductivity enhancement measured is caused by proton conduction in an adsorbed water layer at low temperatures, as described by Shirpour and Gregori for pure and Gadolinium doped ceria thin films.<sup>46,58,186</sup> In addition the results found in this work confirm what Shirpour and Gregori reported as well. Grain boundaries as pathways for proton conduction in CZO thin films can be excluded. As the thin films are dense, pore condensation cannot take place. The only possibility to incorporate additional water except for the surface would therefore be the grain boundaries. Obviously water, hydrogen or hydronium ions are not incorporated into these, as in this case an influence on the conductivities for thin films with different grain boundary densities would likely have been detected. Residual pores in the films are required as additional surfaces to increase the conductivity at higher temperatures already. This is in contrast to what Avila-Paredes et al. report for Gd-doped nanocrystalline ceria ceramics, which was described in section 2.3.2.<sup>52</sup>

Concluding this section it can be stated, that a theoretical model based on established approaches from thermodynamic and mathematic theorems, namely the BET isotherm model and the percolation theory was applied to describe the measured data. The model delivers qualitatively reasonable results, albeit the fact that the mathematical parameter space is over determined. Further development of the presented approach by either reducing the parameter space or by developing the model further, using suitable approximations, backed by a larger experimental dataset with higher data point density, is a promising approach for further research projects. The results obtained revealed interesting insights into the conductivity enhancing effect of humidity on dense mixed electronic and ionic conducting thin films. The obtained data, despite the elaborate analysis, does not show evidence for proton conduction through the thin films under investigation perpendicular to the grain boundaries.

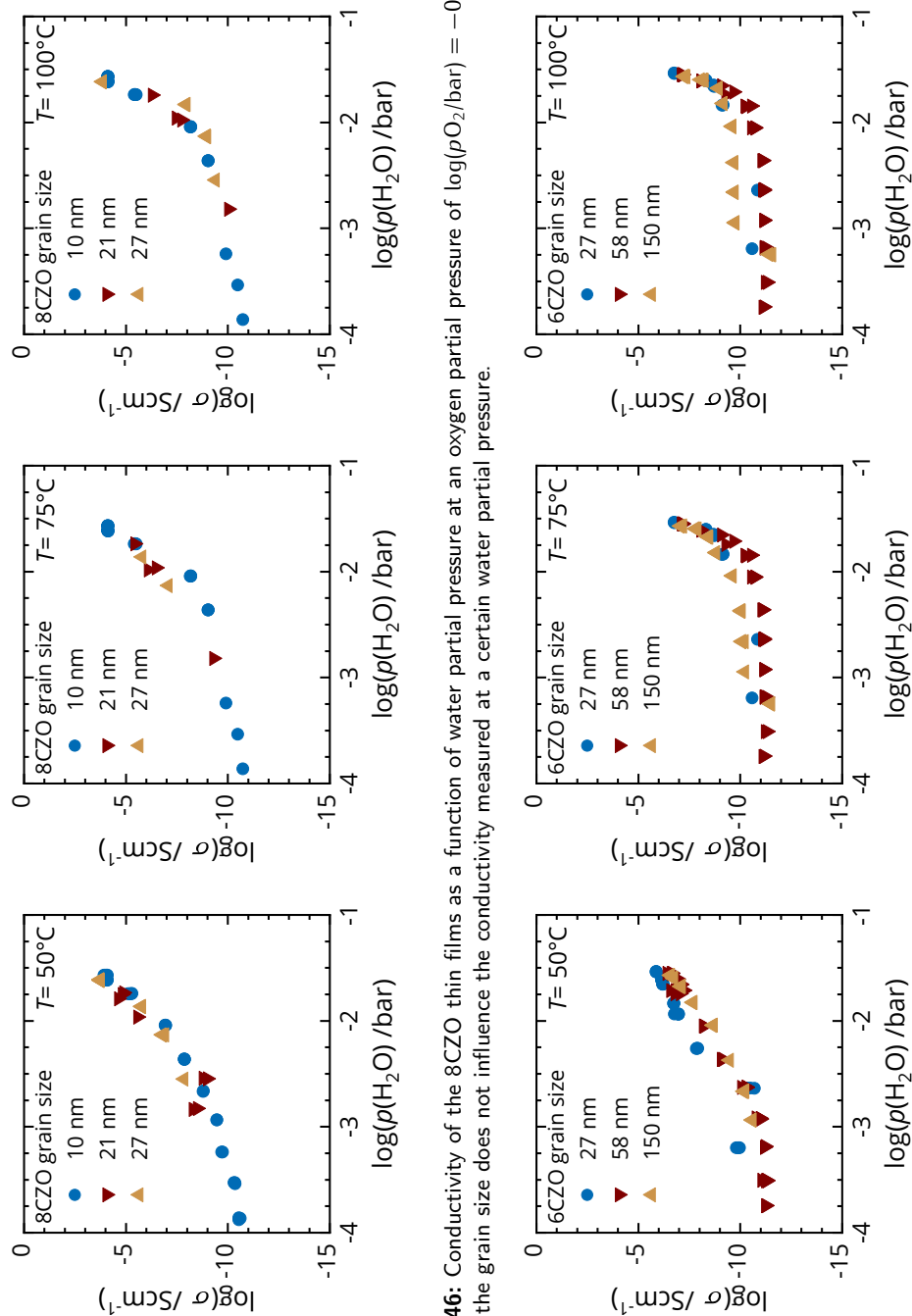


**Figure 4.46:** Conductivity of the 8CZO thin films as a function of water partial pressure at an oxygen partial pressure of  $\log(p_{\text{O}_2}/\text{bar}) = -0.7$ . It can be seen that the grain size does not influence the conductivity measured at a certain water partial pressure.

**Figure 4.47:** Conductivity of the 6CZO thin films as a function of water partial pressure at an oxygen partial pressure of  $\log(p_{\text{O}_2}/\text{bar}) = -0.7$ . It can be seen that the grain size does not influence the conductivity measured at a certain water partial pressure.



## 5 Conclusion and outlook

Concluding the experiments and results presented in this work the approach of combining the ability of PLD thin film preparation to vary the thin film morphology with the possibilities of state of the art impedance spectroscopy equipment to study the influence of the nanostructure properties on the defect chemistry and thus the different charge carrier contributions is very promising. Combining this with the ability of modern state of the art surface analytical techniques like TOF-SIMS, SEM, XPS, and XRD (probably also other techniques like TEM) to fully characterize the samples composition and morphology is necessary. The results obtained in this study nicely prove the potential of this approach, although the scattering of the impedance data prevented to deduce more generally applicable trends that would allow to predict the behavior of other samples with differences in morphology or composition for example.

The morphology of the thin films was varied by tuning parameters during the preparation process. The resulting morphology had a significant impact on the parameters to be applied during the structuring of the interdigital electrodes by photolithography on top of the thin films. It turned out that this step was one of the “bottle necks” in this research project. It took several iterations and thus samples to find a suitable experimental route for preparing a stable electrode on top of the CZO thin films. In case the liftoff of the photo resist did not work, the CZO film was often contaminated as the residuals of the resist were not fully removable. Samples that were prepared elaborately by PLD and characterized by several techniques had to be excluded from the sample stream before EIS experiments could be conducted. There is certainly room for further improvement in upcoming projects on the basis of this work.. A research project solely dedicated to determine the ideal routines for the preparation of interdigital platinum electrodes on CZO thin films of various morphologies would deliver valuable results, improving the sample preparation efficiency. In addition this would also be a great opportunity to include more variation in the PLD preparation parameters than in the present work. Preliminary results, as well as reports in literature, have shown that a larger variety of morphologies is accessible by variation of the temperature and base pressure, rather than by long annealing steps after the deposition.<sup>131</sup>

As the evaluation of EIS data is rather time consuming, the approach in this work was ba-

sically to conduct the EIS measurements in parallel to data evaluation on one sample by another. This was also restricted by the measurement setup, which is only equipped to take up one sample at a time. The most time consuming step in EIS experiments is the time needed for the atmosphere exchange in the oven, until a steady state is reached. Thus, mounting more than one sample in the oven setup and equilibrate multiple samples at once would result in a significant reduction of time needed for the experiments. For realizing this it would be necessary to have an impedance analyzer combined with an automatic switching unit, in order to measure one sample after another. Such a switch would have to be designed properly in order not to introduce any interference, by stray capacities for example, during the impedance measurements. This is not trivial from an electronic point of view, however such technology is available nowadays. An respective electrochemical workstation was actually purchased during the work on this project.<sup>i)</sup> In order to utilize the system and make the aforementioned possible an oven setup was developed as well, which allows to bring up to six samples into one gas tight oven. This oven is characterized by a minimized volume to assure efficient exchange of the oven atmosphere in a reasonable amount of time. In the supplement of this thesis the respective oven design is presented (S. 6.3). As shown in the drawing the samples are mounted on a heatable plate facing upwards, which also has the benefit of being able to wire the samples more easily. Its design also allows to use a ball bonding tool for connecting the sample with the wiring of the setup in order to assure high reproducibility and quality of the electric contact between the interdigital electrode and the impedance analyzer.<sup>ii)</sup>

An additional improvement to get better control of the atmospheric conditions during the impedance measurement in the oven could be the use of a more sophisticated water partial pressure sensor. The device used in this project was a rather simple polymer based capacitive sensor. More sophisticated sensors based on surface treated alumina ceramics are commercially available, allowing the detection of water even at very low partial pressures below 1% relative humidity. The drawback of this sensor technology is, that they are not stable against reducing gas atmospheres, which was revealed in the beginning of this work. Such a sensor was integrated into the EIS setup, but turned out not to deliver any reasonable measurement results. A revision of the device by the manufacturer showed that it had been damaged by applying reducing gases in a previous project.

---

<sup>i)</sup>ZENIUM impedanze analyser from ZAHNER-elektrik GmbH & Co. KG, Germany with RMux addon card allowing to connect up to 16 different electrochemical cells to the impedance analyzer, being switched automatically.

<sup>ii)</sup>The design of the oven was developed by the author of this manuscript and realized during this research project in close collaboration with Harald Weigand from the electronic workshop at the Physical Chemistry Institute at the University of Giessen. It is available to interested researchers at the institute at which this project was undertaken.

The availability of such a setup as described above for multiple impedance measurements under reducing conditions would not only enhance the comparability between different samples, as the exact same conditions would be assured for each sample in the oven. It would also lead to significantly more impedance data obtained that needs to be analyzed. In the recent years a lot of progress was made regarding commercially available software, that allows to apply efficient batch fitting routines and other sophisticated analysis methods, like the distribution of relaxation time (DRT) analysis.<sup>174</sup> Preliminary work on some data obtained during this work showed very promising results. Especially regarding batch fitting of impedance data the commercially available RelaxIS software package by rhd-instruments shall be mentioned here as a very powerful tool for impedance data analysis. In its most recent version, which was not available when the data analysis of this work was carried out, the DRT analysis is also implemented.<sup>143</sup>

Despite the faced and mentioned above, it is shown in this work that nanocrystalline 10CZO, 8CZO and 6CZO thin films exhibit a conduction mechanism influenced by electrons as well as oxygen vacancies for the oxygen partial pressure regime investigated. Increasing the temperature, increases the electron concentration in the material, causing these charge carriers to become the dominating species at higher temperatures.

Water does not influence this behaviour at intermediate temperatures above 250 °C significantly. This is a strong evidence that the changes of conductivity for nanocrystalline powders of the same material, reported by other groups is due to the large internal surface area and capillary forces, causing water to condense in the pores at relatively high temperatures already.

Lowering the temperatures below 200 °C a chemisorbed water layer forms on the CZO thin films, causing an increase in the determined conductivities by a Grotthuss mechanism. The conductivity data in this temperature regime revealed that vacancies in the vicinity of the surface are crucial for the formation of the chemisorbed layer when increasing the humidity, as the conductivity increase for the 8CZO and 6CZO thin films, exhibiting a higher vacancy concentration, was more significant than for the 10CZO thin films.

Lowering the temperatures even further (below approx. 150 °C) water started to form a physisorbed layer on the thin films. A model combining BET isotherm adsorption and percolation theory to describe the measured conductivity of the water films forming on the CZO thin films was introduced. The model was capable of describing the conductivity from physically meaningful thermodynamic parameters. However, it turned out to be over-determined regarding the amount of parameters included. Further model development reducing the amount of fitting parameters is promising in order to determine whether this observation was made solely due to the huge number of parameters or is based on the physics behind

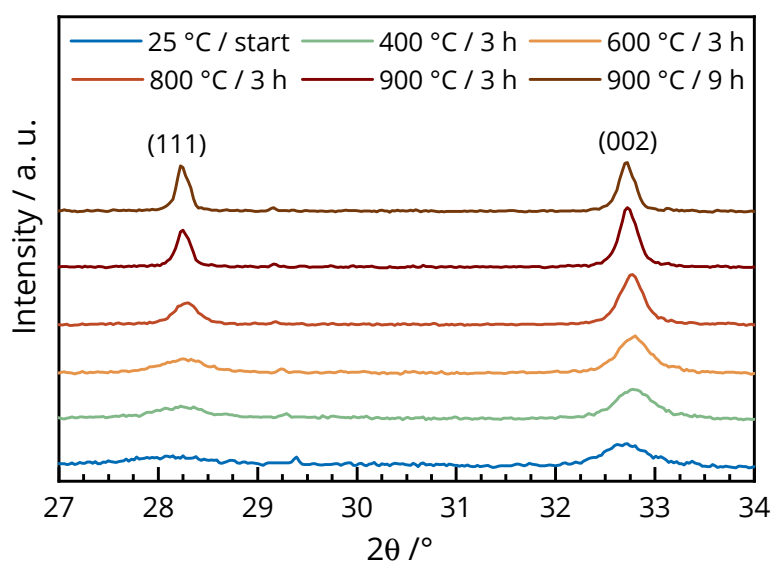
the data.

The evaluation of conductivity values at temperatures corresponding to the same relative humidity allowed to determine the activation energies of the conduction mechanism in the water layer on top of the ceria-zirconia thin films. They are in the same range as those reported for YZS, SiO<sub>2</sub> and TiO<sub>2</sub> porous bulk materials.<sup>116,185,187</sup> Due to their porosity these are supposed to be dominated by their surface properties as well. As the experimental setup in this work is utilizing an interdigital electrode on a dense thin film, it is certain that the conductivities determined are those parallel to the surface. The results are thus confirming the assumptions made in those previous works on porous materials.

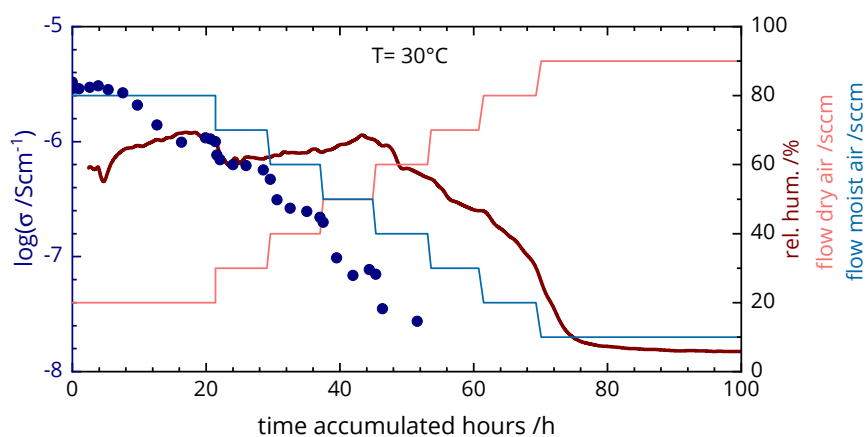
Despite the results achieved in this study it is also shown that the parameter space for the CZO thin film systems under investigation is huge. Further investigations to correlate the morphology of CZO thin films to their transport properties by impedance spectroscopy under humidified conditions are interesting, as so far no influence on the thin films at elevated temperatures was detected for the samples tested in this work. This allows the conclusion that pores in such kind of materials are mandatory for an enhancement of the electrical conductivity by proton conduction.

The techniques and experimental approaches developed during this work are an excellent basis to take this research further, testing a wider range of sample systems, morphologies, as well as a wider oxygen partial pressure range. Using the implemented techniques, it could for example be possible to address the question whether and how the termination of the thin film surface has an influence on the adsorption behaviour of water, as predicted in theoretical works.<sup>188</sup> It will be crucial to assure better statistics by analyzing more thin films to be able to distinguish between scattering of the data caused by systematic errors, or differences caused by the thin film properties.

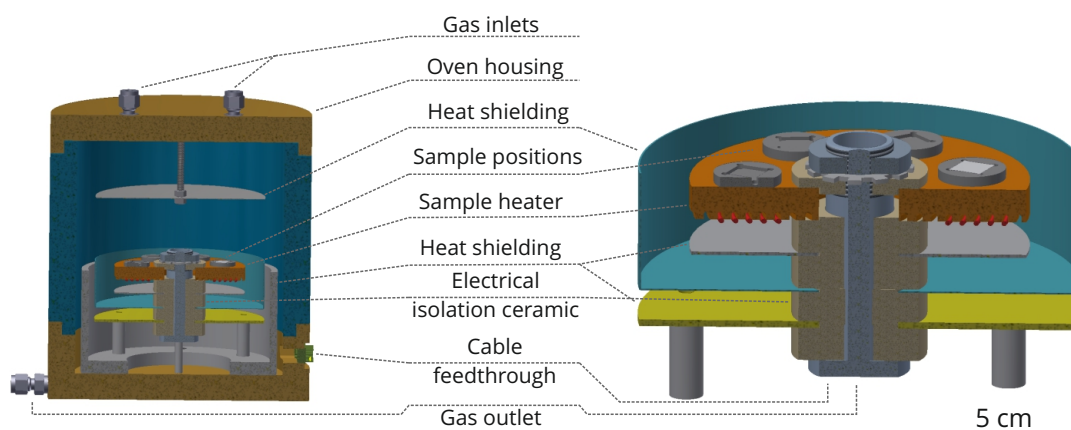
## 6 Supplement



**S. 6.1:** Result of an in-situ XRD heating experiment. It can be seen that no significant grain growth happens within the 3 h at each temperature step, unless the temperature is higher than 600 °C. The data shown here is only preliminary data, that was measured during the testing of the new XRD instrument, equipped with a heating chamber. The data is not corrected for height changes that might have occurred due to thermal dilatation of the ceramic sample holder during the XRD experiments.



**S. 6.2:** Graph demonstrating the problem of correlating the measured conductivity to the humidity in the oven tube. The graph shows the measured conductivity of a 10CZO thin film with 38 nm average grain size and 870 nm thickness. Whilst the conductivity ( $\bullet$ ) drops almost instantly with decreasing flow of moist air ( $\text{—}$ ) into the oven setup, the relative humidity ( $\text{—}$ ) stays almost constant at the humidity sensor behind the oven.



**S. 6.3:** Sketch of a cross section through the multi sample gas tide oven setup, developed during this research project. The oven is designed to mount up to 6 thin film samples on 1x1 cm substrates. The sample heating is able to reach temperatures of up to  $600^\circ\text{C}$  with fast heating rates. The small volume of the oven body allows for a quick and effective gas exchange. In addition the laboratory space needed for this bench-top design oven setup is significantly smaller than that of the tube ovens often used for impedance experiments. Due to the multiple heat shields no separate cooling is necessary.

## Bibliography

- [1] T. Montini, M. Melchionna, M. Monai, P. Fornasiero, *Chem. Rev.* **2016**, *116*, 5987–6041.
- [2] J.-P. Eufinger, *Master Thesis*, University of Gießen, **2010**.
- [3] J.-P. Eufinger, *Conference Talk, SSI 2013- Transport Properties of single-crystalline CeO<sub>2</sub>-ZrO<sub>2</sub>-Y<sub>2</sub>O<sub>3</sub> solid solutions*, **2013**.
- [4] P. Hartmann, T. Brezesinski, J. Sann, A. Lotnyk, J.-P. Eufinger, L. Kienle, J. Janek, *ACS Nano* **2013**, *7*, 2999–3013.
- [5] J.-P. Eufinger, M. Daniels, K. Schmale, S. Berendts, G. Ulbrich, M. Lerch, H.-D. Wiemhöfer, J. Janek, *Phys. Chem. Chem. Phys.* **2014**, *16*, 25583–25600.
- [6] M. Yashima, *Catal. Today* **2015**, *253*, 3–19.
- [7] A. Kirubakaran, S. Jain, R. Nema, *Renew. Sustain. Energy Rev.* **2009**, *13*, 2430–2440.
- [8] E. D. Wachsman, K. T. Lee, *Science (80-. )*. **2011**, *334*, 935–939.
- [9] R. N. Blumenthal, P. W. Lee, R. J. Panlener, *J. Electrochem. Soc.* **1971**, *118*, 123.
- [10] R. N. Blumenthal, R. K. Sharma, *J. Solid State Chem.* **1975**, *13*, 360–364.
- [11] H. L. Tuller, *J. Electrochem. Soc.* **1975**, *122*, 255.
- [12] H. L. Tuller, A. Nowick, *J. Phys. Chem. Solids* **1977**, *38*, 859–867.
- [13] H. L. Tuller, *J. Electrochem. Soc.* **1979**, *126*, 209.
- [14] I. Naik, T. Tien, *J. Phys. Chem. Solids* **1978**, *39*, 311–315.
- [15] B. Cales, J. Baumard, *J. Electrochem. Soc.* **1984**, *131*, 2407–2413.
- [16] R. G. Schwab, R. A. Steiner, *Thin Solid Films* **1992**, *207*, 288–293.
- [17] M. Panhans, R. Blumenthal, *Solid State Ion.* **1993**, *60*, 279–298.
- [18] J. Maier, *Prog. Solid State Chem.* **1995**, *23*, 171–263.
- [19] G. Balducci, J. Kas, P. Fornasiero, M. Graziani, M. S. Islam, J. D. Gale, J. Kašpar, P. Fornasiero, M. Graziani, M. S. Islam, J. D. Gale, *J. Phys. Chem. B* **1997**, *101*, 1750–1753.
- [20] H. L. Tuller, O. Porat, *J. Electroceramics* **1997**, *1*, 41.

- [21] I. Kosacki, *Solid State Ion.* **2000**, 136-137, 1225–1233.
- [22] I. Kosacki, V. Petrovsky, H. U. Anderson, *J. Electroceramics* **2000**, 4, 243–249.
- [23] H. L. Tuller, *Solid State Ion.* **2000**, 131, 143–157.
- [24] M. Boaro, A. Trovarelli, J. H. Hwang, T. O. Mason, *Solid State Ion.* **2002**, 147, 85–95.
- [25] J.-H. Lee, S. M. Yoon, B.-K. Kim, H.-W. Lee, H. S. Song, *J. Mater. Sci.* **2002**, 37, 1165–1171.
- [26] T. Suzuki, I. Kosacki, H. U. Anderson, *Solid State Ion.* **2002**, 151, 111–121.
- [27] V. Rührup, PhD thesis, Westfälische Wilhelms-Universität Münster, **2005**.
- [28] G. a. Umeda, W. C. Chueh, L. Noailles, S. M. Haile, B. S. Dunn, *Energy Environ. Sci.* **2008**, 1, 484.
- [29] Y.-P. Xiong, H. Kishimoto, K. Yamaji, M. Yoshinaga, T. Horita, M. E. Brito, H. Yokokawa, *Electrochem. Solid-State Lett.* **2010**, 13, B21.
- [30] S. J. Litzelman, R. a. Souza, B. Butz, H. L. Tuller, M. Martin, D. Gerthsen, *J. Electroceramics* **2008**, 22, 405–415.
- [31] G. Balakrishnan, P. Kuppusami, T. N. Sairam, R. Thirumurugesan, E. Mohandas, D. Sastikumar, *J. Nanosci. Nanotechnol.* **2009**, 9, 5421–5424.
- [32] S. J. Litzelman, H. L. Tuller, *Solid State Ion.* **2009**, 180, 1190–1197.
- [33] M. C. Göbel, G. Gregori, X. Guo, J. Maier, *Phys. Chem. Chem. Phys.* **2010**, 12, 14351.
- [34] S. Aškračić, Z. Dohčević-Mitrović, A. Kremenović, N. Lazarević, V. Kahlenberg, Z. V. Popović, *J. Raman Spectrosc.* **2012**, 43, 76–81.
- [35] T.-S. Oh, Y. S. Tokpanov, Y. Hao, W. Jung, S. M. Haile, *J. Appl. Phys.* **2012**, 112, 103535.
- [36] B. W. Sheldon, S. Mandowara, J. Rankin, *Solid State Ion.* **2013**, 233, 38–46.
- [37] M. C. Göbel, G. Gregori, J. Maier, *J. Phys. Chem. C* **2013**, 117, 22560–22568.
- [38] T.-S. Oh, D. a. Boyd, D. G. Goodwin, S. M. Haile, *Phys. Chem. Chem. Phys.* **2013**, 15, 2466–72.
- [39] N. Yang, A. Belianinov, E. Strelcov, A. Tebano, V. Foglietti, D. Di Castro, C. Schlueter, T.-I. Lee, A. P. Baddorf, N. Balke, S. Jesse, S. V. Kalinin, G. Balestrino, C. Aruta, *ACS Nano* **2014**, 8, 12494–12501.
- [40] M. T. Elm, J. D. Hofmann, C. Suchomski, J. Janek, T. Brezesinski, *ACS Appl. Mater. Interfaces* **2015**, 7, 11792–11801.
- [41] S. M. Yang, S. Lee, J. Jian, W. Zhang, P. Lu, Q. Jia, H. Wang, T. Won Noh, S. V. Kalinin, J. L. MacManus-Discoll, *Nat. Commun.* **2015**, 6, 8588.

- [42] J. Ding, E. Strelcov, S. V. Kalinin, N. Bassiri-Gharb, *Nanotechnology* **2016**, *27*, 345401.
- [43] J. Ding, E. Strelcov, S. V. Kalinin, N. Bassiri-Gharb, *Nano Lett.* **2015**, *15*, 3669–3676.
- [44] J. Zhang, H. Kumagai, K. Yamamura, S. Ohara, S. Takami, A. Morikawa, H. Shinjoh, K. Kaneko, T. Adschiri, A. Suda, *Nano Lett.* **2011**, *11*, 361–364.
- [45] S. Kim, U. Anselmi-Tamburini, H. J. Park, M. Martin, Z. A. Munir, *Adv. Mater.* **2008**, *20*, 556–559.
- [46] G. Gregori, M. Shirpour, J. Maier, *Adv. Funct. Mater.* **2013**, *23*, 5861–5867.
- [47] X. Q. Fu, C. Wang, H. C. Yu, Y. G. Wang, T. H. Wang, *Nanotechnology* **2007**, *18*, 145503.
- [48] E. Ruiz-Trejo, J. a. Kilner, *J. Appl. Electrochem.* **2009**, *39*, 523–528.
- [49] W. C. Chueh, C.-K. Yang, C. M. Garland, W. Lai, S. M. Haile, *Phys. Chem. Chem. Phys.* **2011**, *13*, 6442.
- [50] L. Almar, A. Tarancón, T. Andreu, M. Torrell, Y. Hu, G. Dezanneau, A. Morata, *Sensors Actuators B Chem.* **2015**, *216*, 41–48.
- [51] S. Kim, J. Maier, *J. Electrochem. Soc.* **2002**, *149*, J73.
- [52] H. J. Avila-Paredes, C.-T. Chen, S. Wang, R. a. De Souza, M. Martin, Z. Munir, S. Kim, *J. Mater. Chem.* **2010**, *20*, 10110.
- [53] H. J. Avila-Paredes, J. Zhao, S. Wang, M. Pietrowski, R. A. De Souza, A. Reinholdt, Z. A. Munir, M. Martin, S. Kim, *J. Mater. Chem.* **2010**, *20*, 990–994.
- [54] G. Chiodelli, F. Maglia, U. Anselmi-Tamburini, Z. a. Munir, *Solid State Ion.* **2009**, *180*, 297–301.
- [55] W. C. Chueh, C. Falter, M. Abbott, D. Scipio, P. Furler, S. M. Haile, A. Steinfeld, *Science* **2010**, *330*, 1797–801.
- [56] R. A. De Souza, Z. A. Munir, S. Kim, M. Martin, *Solid State Ion.* **2011**, *196*, 1–8.
- [57] R. Jimenez, W. Bucheli, A. Varez, J. Sanz, *Fuel Cells* **2011**, *11*, 642–653.
- [58] M. Shirpour, G. Gregori, R. Merkle, J. Maier, *Phys. Chem. Chem. Phys.* **2011**, *13*, 937–940.
- [59] S. Hayun, T. Y. Shvareva, A. Navrotsky, *J. Am. Ceram. Soc.* **2011**, *94*, 3992–3999.
- [60] D. R. Mullins, *Surf. Sci. Rep.* **2015**, *70*, 42–85.
- [61] G. Chiodelli, *Solid State Ion.* **1996**, *91*, 109–121.
- [62] J. L. Hertz, H. L. Tuller, *Solid State Ion.* **2007**, *178*, 915–923.

- [63] C. O. Bounds, *J. Miner. Met. Mater. Soc.* **1998**, *50*, 38–42.
- [64] A. Trovarelli, *Catalysis by Ceria and Related Materials Materials*, World Scientific Publishing, London, 2nd ed., **2005**, p. 527.
- [65] D. S. Aidhy, W. J. Weber, *J. Mater. Res.* **2016**, *31*, 2–16.
- [66] R. T. Downs, M. Hall-Wallace, *Am. Mineral.* **2003**, *88*, 247–250.
- [67] S. Gražulis, D. Chateigner, R. T. Downs, A. F. T. Yokochi, M. Quirós, L. Lutterotti, E. Manakova, J. Butkus, P. Moeck, A. Le Bail, *J. Appl. Crystallogr.* **2009**, *42*, 726–729.
- [68] S. Gražulis, A. Daškevič, A. Merkys, D. Chateigner, L. Lutterotti, M. Quirós, N. R. Serebryanaya, P. Moeck, R. T. Downs, A. Le Bail, *Nucleic Acids Res.* **2012**, *40*, D420–D427.
- [69] S. Gražulis, A. Merkys, A. Vaitkus, M. Okulič-Kazarinas, *J. Appl. Crystallogr.* **2015**, *48*, 85–91.
- [70] A. Merkys, A. Vaitkus, J. Butkus, M. Okulič-Kazarinas, V. Kairys, S. Gražulis, *J. Appl. Crystallogr.* **2016**, *49*, 292–301.
- [71] F. Kröger, H. Vink in *Solid State Phys., Vol. 3* (Eds.: F. Seitz, D. Turnbull), Academic Press, New York, **1956**, Chapter 5, pp. 307–435.
- [72] T. Norby, *J. Mater. Chem.* **2001**, *11*, 11–18.
- [73] F.-C. Chiu, C.-M. Lai, *J. Phys. D. Appl. Phys.* **2010**, *43*, 075104.
- [74] S. Vangelista, R. Piagge, S. Ek, T. Sarnet, G. Ghidini, C. Martella, A. Lamperti, *Thin Solid Films* **2017**, *636*, 78–84.
- [75] N. Knoblauch, L. Dörrer, P. Fielitz, M. Schmücker, G. Borchardt, *Phys. Chem. Chem. Phys.* **2015**, *17*, 5849–5860.
- [76] E. Mamontov, T. Egami, R. Brezny, M. Koranne, S. Tyagi, *J. Phys. Chem. B* **2000**, *104*, 11110–11116.
- [77] E. Tani, M. Yoshimura, S. Somiya, *J. Am. Ceram. Soc.* **1983**, *66*, 506–510.
- [78] R. Di Monte, J. Kašpar, *Catal. Today* **2005**, *100*, 27–35.
- [79] P. Duwez, F. Odell, *J. Am. Ceram. Soc.* **2006**, *33*, 274–283.
- [80] A. S. Ivanova, *Kinet. Catal.* **2009**, *50*, 797–815.
- [81] M. Yashima, H. Takashina, M. Kakihana, M. Yoshimura, *J. Am. Ceram. Soc.* **1994**, *77*, 1869–1874.
- [82] M. Yashima, H. Arashi, M. Kakihana, M. Yoshimura, *J. Am. Ceram. Soc.* **1994**, *77*, 1067–1071.

- [83] F. Zhang, C.-H. Chen, J. C. Hanson, R. D. Robinson, I. P. Herman, S.-W. Chan, *J. Am. Ceram. Soc.* **2006**, *89*, 1028–1036.
- [84] A. Varez, E. Garcia-Gonzalez, J. Sanz, *J. Mater. Chem.* **2006**, *16*, 4249–4256.
- [85] A. Cabañas, J. A. Darr, E. Lester, M. Poliakoff, *J. Mater. Chem.* **2001**, *11*, 561–568.
- [86] B. Chen, Y. Ma, L. Ding, L. Xu, Z. Wu, Q. Yuan, W. Huang, *J. Phys. Chem. C* **2013**, *2*, 5800–5810.
- [87] D. Chen, Y. Cao, D. Weng, H. L. Tuller, *Chem. Mater.* **2014**, *26*, 5143–5150.
- [88] S. R. Bishop, D. Marrocchelli, W. Fang, K. Amezawa, K. Yashiro, G. W. Watson, *Energy Environ. Sci.* **2013**, *6*, 1142.
- [89] N. Sammes, *Solid State Ion.* **1999**, *121*, 121–125.
- [90] P. Hartmann, *Mesoporöse Dünnschichten der festen Lösung CeO<sub>2</sub>-ZrO<sub>2</sub> : Elektrische Leitfähigkeit nanostrukturierter gemischter Leiter*, Justus-Liebig-Universität Gießen Masterthesis, **2010**.
- [91] D. Xu, Q. Wang, Y. Tang, Z. Lu, Z. Liu, S. Liu, G. Zhang, W. Su, *J. Phys. Condens. Matter* **2002**, *14*, 11265–11268.
- [92] E. Mamontov, R. Brezny, M. Koranne, T. Egami, *J. Phys. Chem. B* **2003**, *107*, 13007–13014.
- [93] R. A. De Souza, *Phys. Chem. Chem. Phys.* **2009**, *11*, 9939.
- [94] J. Maier, *J. Phys. Chem. Solids* **1985**, *46*, 309–320.
- [95] A. Tschöpe, *Solid State Ion.* **2001**, *139*, 255–265.
- [96] A. Tschöpe, *Solid State Ion.* **2001**, *139*, 267–280.
- [97] A. Tschöpe, R. Birringer, *J. Electroceramics* **2001**, *7*, 169–177.
- [98] M. Gouy, *J. Phys. Théorique Appliquée* **1910**, *9*, 457–468.
- [99] D. L. Chapman, *Philos. Mag. Ser. 6* **1913**, *25*, 475–481.
- [100] M. Dornhege, PhD thesis, Technische Universität Berlin, **2007**.
- [101] C. H. Hamann, W. Vielstich in *Elektrochemie*, WILEY-VCH, Weinheim, 4th ed., **2005**, Chapter 3, p. 662.
- [102] A. Tschöpe, C. Bäuerle, R. Birringer, *J. Appl. Phys.* **2004**, *95*, 1203–1210.
- [103] J. M. Polfus, K. Toyoura, F. Oba, I. Tanaka, R. Haugrud, *Phys. Chem. Chem. Phys.* **2012**, *14*, 12339.
- [104] D. Van Laethem, J. Deconinck, D. Depla, A. Hubin, *J. Eur. Ceram. Soc.* **2016**, *36*, 1983–1994.

- [105] N. Kochetova, I. Animitsa, D. Medvedev, A. Demin, P. Tsiakaras, *RSC Adv.* **2016**, *6*, 73222–73268.
- [106] D. H. Everett, *Pure Appl. Chem.* **1972**, *31*, 78.
- [107] P. Atkins, *Physikalische Chemie*, Oxford University Press, 3rd ed., **2002**.
- [108] I. Langmuir, *J. Am. Chem. Soc.* **1918**, *40*, 1361–1403.
- [109] I. Langmuir, *J. Am. Chem. Soc.* **1915**, *37*, 1139–1167.
- [110] W. H. Bragg, W. L. Bragg, *Proc. R. Soc. A Math. Phys. Eng. Sci.* **1913**, *88*, 428–438.
- [111] S. Brunauer, P. H. Emmett, E. Teller, *J. Am. Chem. Soc.* **1938**, *60*, 309–319.
- [112] K. S. Sing, F. Rouquerol, J. Rouquerol in *Adsorpt. by Powders Porous Solids*, Elsevier, **2014**, Chapter 5, pp. 159–189.
- [113] M. Prin, M. Pijolat, M. Soustelle, O. Touret, *Thermochim. Acta* **1991**, *186*, 273–283.
- [114] S. Kim, R. Merkle, J. Maier, *Solid State Ion.* **2003**, *161*, 113–119.
- [115] H. Takamura, N. Takahashi, *Solid State Ion.* **2010**, *181*, 100–103.
- [116] S. Raz, K. Sasaki, J. Maier, I. Riess, *Solid State Ion.* **2001**, *143*, 181–204.
- [117] M. A. Blesa, A. J. Maroto, A. E. Regazzoni, *J. Colloid Interface Sci.* **1990**, *140*, 287–290.
- [118] J. Ding, E. Strelcov, S. V. Kalinin, N. Bassiri-Gharb, *Nanotechnology* **2016**, *27*, 345401.
- [119] E. Strelcov, A. V. Ievlev, S. Jesse, I. I. Kravchenko, V. Y. Shur, S. V. Kalinin, *Adv. Mater.* **2014**, *26*, 958–963.
- [120] D. Stauffer, A. Aharony, *Introduction to percolation theory*, Taylor & Francis Group, London, 2nd ed., **1992**, p. 181.
- [121] P. J. Flory, *J. Am. Chem. Soc.* **1941**, *63*, 3083–3090.
- [122] W. H. Stockmayer, *J. Chem. Phys.* **1943**, *11*, 45–55.
- [123] A. Bunde, J. W. Kantelhardt in *Diffus. Condens. Matter* (Ed.: P. Heitjans), Springer-Verlag, Berlin/Heidelberg, **2005**, Chapter 22, pp. 895–914.
- [124] S. Wolfram, *Percolation on a square grid*, **2011**, <http://demonstrations.wolfram.com/PercolationOnASquareGrid/>, accessed 2020-08-16.
- [125] C.-W. Nan, Y. Shen, J. Ma, *Annu. Rev. Mater. Res.* **2010**, *40*, 131–151.
- [126] C. D. Lorenz, R. M. Ziff, *J. Chem. Phys.* **2001**, *114*, 3659–3661.
- [127] M. B. Bryning, M. F. Islam, J. M. Kikkawa, A. G. Yodh, *Adv. Mater.* **2005**, *17*, 1186–1191.

- [128] M. M. Ahmad, S. A. Makhlof, K. M. S. Khalil, *J. Appl. Phys.* **2006**, *100*, 094323.
- [129] Q. Li, S. Xu, Q. Zeng, *Cem. Concr. Compos.* **2016**, *70*, 35–47.
- [130] D. Almond, G. Duncan, A. West, *Solid State Ion.* **1983**, *8*, 159–164.
- [131] A. Infortuna, A. S. Harvey, L. J. Gauckler, *Adv. Funct. Mater.* **2008**, *18*, 127–135.
- [132] J. A. Thornton, *Annu. Rev. Mater. Sci.* **1977**, *7*, 239–260.
- [133] R. Anderhalt in *Scanning Microsc. Nanotechnol.*, Springer New York, New York, NY, **2006**, pp. 76–100.
- [134] L. Thompson in *Introd. to Microlithogr. Theory, Mater. Process. (Acs Symp. Ser., American Chemical Society, 1983, Chapter Chapter 1, pp. 1–13.*
- [135] P. Hartmann, *Promotionsvorhaben*, **2010**.
- [136] S. Strobel, C. Kirkendall, J.-B. Chang, K. K. Berggren, *Nanotechnology* **2010**, *21*, 505301.
- [137] T. Ryll, H. Galinski, L. Schlagenhaut, P. Elser, J. L. M. Rupp, A. Bieberle-Hutter, L. J. Gauckler, *Adv. Funct. Mater.* **2011**, *21*, 565–572.
- [138] C. V. Thompson, *Annu. Rev. Mater. Res.* **2012**, *42*, 399–434.
- [139] Hygrosens Instruments GmbH, *Technisches Datenblatt - LabKit mit USB-Schnittstelle HYGROCHIP*, Hygrosens instruments gmbh technical report, Hygrosens Instruments GmbH, Löffringen, **2010**.
- [140] Innovative Sensor Technology IST AG, *HYT 939 - technical datasheet*, Innovative sensor technology ist ag technical report, **2017**.
- [141] ZIROX Sensoren und Elektronik GmbH, *ZIROX Electrolysis Device SGM5EL Technical Note*, Zirox sensoren und elektronik gmbh technical report, ZIROX Sensoren und Elektronik GmbH, Greifswald, Germany, **2017**.
- [142] T-E-Klebertechnik, *Technisches Datenblatt A2 - Keramische Hochtemperatureklebstoffe und Pasten*, T-e-klebertechnik technical report, **2014**.
- [143] Rhd instruments, *RelaxIS*, **2018**, <https://www.rhd-instruments.de/en/products/software/relaxis>, accessed 2020-08-24.
- [144] OriginLab, *Origin 2018*, **2018**.
- [145] D. G. Lamas, R. O. Fuentes, I. O. Fábregas, M. E. Fernández de Rapp, G. E. Lascalea, J. R. Casanova, N. E. Walsøe de Reca, A. F. Craievich, *J. Appl. Crystallogr.* **2005**, *38*, 867–873.
- [146] M. Yashima, S. Kobayashi, T. Yasui, *Solid State Ion.* **2006**, *177*, 211–215.

- [147] A. Varez, E. Garcia-Gonzalez, J. Jolly, J. Sanz, *J. Eur. Ceram. Soc.* **2007**, *27*, 3677–3682.
- [148] R. D. Shannon, *Acta Crystallogr. Sect. A* **1976**, *32*, 751–767.
- [149] M. Mogensen, N. M. Sammes, G. A. Tompsett, *Solid State Ion.* **2000**, *129*, 63–94.
- [150] P. Scherrer, *Nachrichten von der Gesellschaft der Wissenschaften zu Göttingen Math. Klasse* **1918**, 98–100.
- [151] A. L. Patterson, *Phys. Rev.* **1939**, *56*, 978–982.
- [152] C. Artini, G. A. Costa, M. Pani, A. Lausi, J. Plaisier, *J. Solid State Chem.* **2012**, *190*, 24–28.
- [153] CrysTec GmbH, *Sapphire datasheet*, Crystec gmbh technical report, CrysTec GmbH, Berlin, **2017**.
- [154] T. Salkus, V. Venckute, E. Kazakevicius, V. Kazlauskiene, J. Miskinis, A. Kezionis, V. Kunigelis, A. Orliukas, *Lith. J. Phys.* **2009**, *49*, 311–316.
- [155] J. Zahnow, *Mikrokontaktierung und elektrochemische Charakterisierung einzelner CeO<sub>2</sub>-Kristallite*, **2016**.
- [156] T. Skála, N. Tsud, K. C. Prince, V. Matolín, *Appl. Surf. Sci.* **2011**, *257*, 3682–3687.
- [157] J. Burke, D. Turnbull, *Prog. Met. Phys.* **1952**, *3*, 220–292.
- [158] J. L. Rupp, A. Infortuna, L. J. Gauckler, *Acta Mater.* **2006**, *54*, 1721–1730.
- [159] H. Natter, M. Schmelzer, M.-S. Löffler, C. E. Krill, A. Fitch, R. Hempelmann, *J. Phys. Chem. B* **2000**, *104*, 2467–2476.
- [160] H. Natter, M.-S. Löffler, C. Krill, R. Hempelmann, *Scr. Mater.* **2001**, *44*, 2321–2325.
- [161] C. Moelle, H. Fecht, *Nanostructured Mater.* **1995**, *6*, 421–424.
- [162] J. W. Cahn in *Sel. Work. John W. Cahn, Vol. 10* (Eds.: W. C. Carter, W. C. Johnson), John Wiley & Sons, Inc., Hoboken, NJ, USA, **2013**, Chapter 15, pp. 115–116.
- [163] J. W. Cahn in *Sel. Work. John W. Cahn, Vol. 10*, John Wiley & Sons, Inc., Hoboken, NJ, USA, **2013**, Chapter 16, pp. 117–126.
- [164] C. Belouet, *Appl. Surf. Sci.* **1996**, *96-98*, 630–642.
- [165] B. E. McNealy, J. Jiang, J. L. Hertz, *J. Electrochem. Soc.* **2015**, *162*, F537–F546.
- [166] J. Macdonald, *J. Electroanal. Chem. Interfacial Electrochem.* **1987**, *223*, 25–50.
- [167] M. Shoar Abouzari, F. Berkemeier, G. Schmitz, D. Wilmer, *Solid State Ion.* **2009**, *180*, 922–927.
- [168] M. Gerstl, E. Navickas, G. Friedbacher, F. Kubel, M. Ahrens, J. Fleig, *Solid State Ion.* **2011**, *185*, 32–41.

- [169] P. Jasinski, V. Petrovsky, T. Suzuki, H. U. Anderson, *J. Electrochem. Soc.* **2005**, *152*, J27.
- [170] R. W. Oppermann, *Master thesis*, Universität Gießen, **2016**.
- [171] Y. P. Xiong, H. Kishimoto, K. Yamaji, M. Yoshinaga, T. Horita, M. E. Brito, H. Yokokawa, *Solid State Ion.* **2011**, *192*, 476–479.
- [172] S. Kim, J. Maier, *J. Electrochem. Soc.* **2002**, *149*, J73.
- [173] D. Pérez-Coll, G. C. Mather, *Solid State Ion.* **2010**, *181*, 20–26.
- [174] F. Ciucci, C. Chen, *Electrochim. Acta* **2015**, *167*, 439–454.
- [175] Bio-Logic Science Instruments, *Distribution of Relaxation Times (RT): an introduction*, Bio-logic science instruments technical report, **2017**.
- [176] T. Blank, L. Eksperiandova, K. Belikov, *Sensors Actuators B Chem.* **2016**, *228*, 416–442.
- [177] Bureau International des Poids et Mesures, *Guide to the Realization of the ITS-90*, **2018**, <https://www.bipm.org/en/committees/cc/cct/guide-its90.html>, accessed 2020-08-24.
- [178] W. Wagner, *J. Phys. Chem. Ref. Data* **1999**, *31*, 387.
- [179] S. Miyoshi, Y. Akao, N. Kuwata, J. Kawamura, Y. Oyama, T. Yagi, S. Yamaguchi, *Chem. Mater.* **2014**, *26*, 5194–5200.
- [180] I. Wolfram Research, *Mathematica*, **2017**.
- [181] S. Kumar, P. K. Schelling, *J. Chem. Phys.* **2006**, *125*, 204704.
- [182] M. A. Henderson, C. L. Perkins, M. H. Engelhard, S. Thevuthasan, C. H. F. Peden, *Surf. Sci.* **2003**, *526*, 1–18.
- [183] C. T. Campbell, J. R. V. Sellers, *Chem. Rev.* **2013**, *113*, 4106–4135.
- [184] ASTM International in *B. Stand.*, ASTM International, West Conshohocken, 11th ed., **2014**, Chapter ASTM D1125, p. 8.
- [185] S. Ø. Stub, E. Vøllestad, T. Norby, *J. Phys. Chem. C* **2017**, *121*, 12817–12825.
- [186] M. Shirpour, G. Gregori, R. Merkle, J. Maier, *Phys. Chem. Chem. Phys.* **2011**, *13*, 937–940.
- [187] J. H. Anderson, G. A. Parks, *J. Phys. Chem.* **1968**, *72*, 3662–3668.
- [188] M. Molinari, S. C. Parker, D. C. Sayle, M. S. Islam, *J. Phys. Chem. C* **2012**, *116*, 7073–7082.